

THESIS

A STATISTICAL PREDICTION MODEL FOR EAST PACIFIC AND ATLANTIC
TROPICAL CYCLONE GENESIS

Submitted by

Stephanie A. Slade

Department of Atmospheric Science

In partial fulfillment of the requirements

For the Degree of Master of Science

Colorado State University

Fort Collins, Colorado

Spring 2012

Master's Committee:

Advisor: Eric D. Maloney

David Thompson
Edwin Chong

Copyright by Stephanie A. Slade 2012

All Rights Reserved

ABSTRACT

A STATISTICAL PREDICTION MODEL FOR EAST PACIFIC AND ATLANTIC TROPICAL CYCLONE GENESIS

A statistical model is developed via multiple logistic regression for the prediction of weekly tropical cyclone activity over the East Pacific and Atlantic Ocean regions using data from 1975 to 2009. The predictors used in the model include a climatology of tropical cyclone genesis for each ocean basin, an El Niño-Southern Oscillation (ENSO) index derived from the first principal component of sea surface temperature over the Equatorial East Pacific region, and two indices representing the propagating Madden-Julian Oscillation (MJO). These predictors are suggested as useful for the prediction of East Pacific and Atlantic cyclogenesis based on previous work in the literature and are further confirmed in this study using basic statistics. Univariate logistic regression models are generated for each predictor in each region to ensure the choice of prediction scheme. Using all predictors, cross-validated hindcasts are developed out to a seven week forecast lead. A formal stepwise predictor selection procedure is implemented to select the predictors used in each region at each forecast lead.

Brier skill scores and reliability diagrams are used to assess the skill and dependability of the models. Results show a significant increase in model skill at predicting tropical cyclogenesis by the inclusion of the MJO out to a three week forecast lead for the East Pacific and a two week forecast lead for the Atlantic. The importance of ENSO for Atlantic genesis prediction is highlighted, and the uncertain effects of ENSO

on East Pacific tropical cyclogenesis are re-visited using the prediction scheme. Future work to extend the prediction model with other predictors is discussed.

ACKNOWLEDGEMENTS

This study was made possible due to the support of various individuals and organizations. I would like to deeply thank my advisor, Dr. Eric D. Maloney, for his excellent guidance and support throughout this study. I also would like to extend my gratitude to Dr. David Thompson and Dr. Edwin Chong for serving in my committee and providing highly useful feedback. Furthermore, I am very grateful for the advice of Dr. Phillip Chapman, who provided invaluable instruction on the regression methods used in this study. I am greatly appreciative of the faculty and my colleagues at the Colorado State University Department of Atmospheric Science for aiding in my education and understanding of the atmosphere. I would specially like to thank the Maloney research group for always helping me when needed, particularly in the early stages of my Master's degree when I was learning how to program. I am also very grateful for my family and friends for their strong support throughout my education journey. In addition, this study would not have been possible without the financial support of the Center for Multiscale Modeling of Atmospheric Processes (CMMAP) and the Alliance for Graduate Education and the Professoriate (AGEP). These organizations provided my funding during my first year as a Master's candidate. This study was further supported by the National Science Foundation Climate and Large-Scale Dynamics Program grant ATM-0832868 and ATM-0946911.

TABLE OF CONTENTS

Abstract.....	ii
Acknowledgements.....	iv
Table of Contents.....	v
1. Introduction.....	1
1.1 Motivation.....	1
1.2 Tropical Cyclogenesis.....	2
1.2.1 An Initial disturbance.....	2
1.2.2 A Favorable Environment.....	4
1.3 The Madden-Julian Oscillation.....	6
1.3.1 Description.....	6
1.3.2 The MJO and East Pacific Tropical Cyclogenesis.....	9
1.3.3 The MJO and Atlantic Tropical Cyclogenesis.....	12
1.4 El Niño-Southern Oscillation.....	15
1.4.1 Description.....	15
1.4.2 ENSO and East Pacific Tropical Cyclogenesis.....	17
1.4.3 ENSO and Atlantic Tropical Cyclogenesis.....	18
1.5 Medium-Long Lead Cyclogenesis Prediction.....	20
1.5.1 Seasonal Prediction.....	20
1.5.2 Intraseasonal Prediction.....	22
1.6 Overview of Study.....	27
2. Data and Methodology.....	28
2.1 Data.....	28
2.1.1 HURDAT.....	28
2.1.2 HADISST.....	29
2.1.3 NOAA Interpolated OLR.....	30
2.1.4 NCEP/NCAR 40-Year Reanalysis.....	31
2.2 Predictor Development.....	32
2.2.1 Climatology.....	32
2.2.2 Leading Modes of SST.....	33
2.2.3 RMM Indices.....	36
2.3 Logistic Regression.....	37

2.4 Sequential Forward Selection.....	40
2.5 Forecast Verification.....	41
3. Predictors	43
3.1 Predictor Justification.....	43
3.1.1 Climatology	43
3.1.2 The MJO.....	45
3.1.3 ENSO and PC2 of Equatorial East Pacific SST	50
3.1.4 Goodness of Fit.....	54
3.2 Predictor Selection	56
4. Hindcasts.....	58
4.1 Probability Hindcasts	58
4.1.1 East Pacific Hindcasts	59
4.1.2 Atlantic Hindcasts.....	62
5. Model Skill and Reliability.....	67
5.1 Brier Skill Scores	67
5.2 Reliability Diagrams	69
5.2.1 East Pacific	70
5.2.2 Atlantic	71
5.3 Hurricane Strength Skill.....	72
6. Summary and Conclusions	75
References.....	78
Appendix I	88
Appendix II.....	106

1. Introduction

1.1 Motivation

A hurricane is a rotating low pressure oceanic weather system in the Atlantic or East Pacific with 1-minute sustained winds of at least 64 knots (~ 74 mph). Hurricanes have alternate names in other regions such as typhoons, Severe Tropical Cyclones, and Severe Cyclonic Storms. Worldwide, they are among the most destructive natural phenomena in recorded history. Typhoons stopped the Mongolian attempt to invade the Japanese twice; once in 1274, killing almost 13,000 men and destroying many of their ships, and again in 1281, with further devastating losses (Emanuel, 2005). Even though the Mongols lacked the knowledge and technology of today that could have foreseen these losses, more recent hurricanes have still caused staggering destruction. In 2005, Hurricane Katrina directly caused about 1000 deaths (Brunkard et al., 2008) and cost approximately 81 billion dollars worth of damage, normalized to today's inflation, wealth, and population (Pielke et al., 2008). In 2008, Cyclone Nargis made landfall over Myanmar resulting in over 138,000 deaths and over \$10 billion in damages, making it the eight most lethal cyclone on record (Fritz et al., 2009). All hurricanes evolve from tropical storms (sustained winds of at least 35 knots but less than 64 knots), but not all tropical storms become hurricanes (Emanuel, 2005). In 2001, Tropical Storm Allison hit southeast Texas, resulting in the deaths of 43 people and causing 5.1 billion dollars in damages (Ross and Lott, 2003). For this reason, not only hurricanes but also tropical

storm prediction improvements are vital to ensure adequate evacuations and safety procedures.

This study develops an intraseasonal statistical model for tropical cyclone formation over the East Pacific and North Atlantic Ocean basins similar to the Southern Hemisphere model of Leroy and Wheeler (2008). The following sections provide relevant background information on the development of the model.

1.2 Tropical Cyclogenesis

1.2.1 An Initial disturbance

The prominent lower and upper level tropospheric flow signature observed prior to tropical disturbance intensification into a tropical cyclone was first noted by Herbert Riehl. Riehl (1948a, 1948b, 1950) describes the process which brings about the development of a tropical storm, or tropical cyclogenesis, as the evolution of a moving wave or disturbance within the trade winds occurring under a favorable environment of upper-level divergence. Since the early work of Riehl, the mechanisms which bring about tropical cyclogenesis have been studied but are still poorly understood.

Tropical cyclones in the Atlantic and East Pacific can form via tropical easterly waves. Tropical cyclones tend to form along low surface pressure associated with a tropical wave-trough. While a large amount of wave-troughs occur during a given hurricane season, only 20% of those which form in the east and central regions of the Atlantic via African easterly waves actually lead to cyclogenesis (Frank, 1970). Studies have theorized that this may be due to the initial lack of surface cyclonic circulation in a mesoscale convective vortex (MCV; Bister and Emanuel, 1997; Ritchie and Holland,

1997). An MCV in the Atlantic or East Pacific basins can be generated via mesoscale convective systems (MCSs) that develop in a wave-trough within easterly waves (Bister and Emanuel, 1997; Molinari et al., 1997; Dunkerton et al., 2009).

Using RAMS, a non-hydrostatic cloud model, Montgomery et al. (2006) looked at the case of an MCV with a weak ocean surface cyclonic circulation developing into a warm-core tropical depression vortex. The study found a possible upscale organization mechanism leading to the evolution of a self-sustaining vortex. Given a high-vorticity MCV, the primary coherent structure in the model simulations consists of vortical hot towers (VHTs). VHTs are cumulonimbus convection cores with a small horizontal scale and extend to at least the tropopause. The VHTs were found to give rise to powerful vertical cyclonic vorticity via stretching and tilting of the preexisting vorticity found in the MCV. This mechanism led to a surface concentrated rotary system within realistic time scales and was shown to precede the axisymmetric wind-induced surface heat exchange (WISHE; Rotunno and Emanuel, 1987) believed to be the principal mechanism of the intensification of a surface-concentrated vortex (Montgomery et al., 2006).

The mechanism behind cyclone genesis occurring within an easterly wave trough is hypothesized by the marsupial paradigm in Dunkerton et al. (2009). The marsupial paradigm describes the ideal region for vortex development as a “pouch” that is provided by the wave. The center of the pouch, defined as the intersection between the critical layer (the region where the wave phase speed equals the mean flow) and the trough axis of the easterly wave, is the most favorable region for tropical cyclogenesis. The pouch acts as a protective layer against cyclone development inhibitors such as dry air from the Sahara Air Layer. The vortex can exist outside of this pouch once it has gathered

sufficient spin to develop its own propagation; the strength of the vortex can be increased via convective intensification and the merging of vortices within the pouch.

Various other mechanisms leading to tropical cyclogenesis have been theorized. Given a large-scale vortex, smaller-scale regions of vorticity have been observed to fuse with and energize the larger-scale vortex flow (Montgomery and Enagonia, 1998; Moller and Montgomery, 1999, 2000). Other routes exist such as cyclogenesis via baroclinic development (Bosart and Bartlo, 1991), wave energy accumulation (Shapiro, 1977; Sobel and Bretherton, 1999), and low-level disturbance interaction with upper-level disturbances (Sadler, 1976; Montgomery and Farrell, 1993).

1.2.2 A Favorable Environment

Tropical cyclones are composed of a tropospheric warm core which obtains its energy primarily from ocean evaporation and condensation in convection (Emanuel, 1988). This warm core is what allows for intense winds to form near the surface (Holland, 1993). Favorable environmental conditions are essential to allow for sufficient accumulation of condensational heat at the core to be used for sensible warming.

Gray (1979) statistically related cyclogenesis to six climatological environmental conditions which he uses to define a seasonal genesis parameter:

- i. Adequate surface to 400-mb vorticity and convergence.
- ii. A large enough coriolis parameter for large scale rotation. The latitudinal distance from the equator is generally a minimum of 5° to allow for a sufficient coriolis force to generate cyclonic rotation (Gray, 1979; Lighthill et al., 1994).
- iii. Low vertical shear of the horizontal winds. High vertical wind shear inhibits tropical cyclone formation due to the detrainment of heat from the disturbance.

Interference of formation due to wind shear would make it difficult for the storm's required thermal energy to become concentrated at its core (Gray, 1968; Gray, 1979). Vertical shear has also been shown to negatively impact cyclone genesis and growth through vertical stability (DeMaria, 1996) and secondary circulation effects (Bender, 1997).

- iv. Surface to 60 meter ocean temperatures above 26°C. This ocean thermal energy component with a deep thermocline is essential to compensate for turbulent mixing within the mixed layer that entrains cold water from below.
- v. Deep atmospheric conditional instability. A sufficient decrease in temperature with height must be present so saturated parcels can continue to rise along moist adiabats (Lighthill et al., 1994). This component deals with the vertical gradient of the equivalent potential temperature, or the moist buoyancy potential, between the surface and 500-mb. Gray (1979) observed that cyclogenesis cannot occur if there is a lack of upper-lower tropospheric vertical coupling brought on by cumulonimbus convection.
- vi. High values of low-mid level tropospheric relative humidity. As dry air is entrained into convecting parcels, evaporative cooling occurs that can cause buoyancy loss. Sufficiently high levels of relative humidity would prevent such effects (Lighthill et al., 1994). Larger values of relative humidity make the tropospheric column more conducive to deep convection and enhance the surface to mid-level vertical coupling (Gray, 1979).

In addition to the favorable conditions listed, an initial pre-existing disturbance is also necessary (Emanuel, 1989; Rotunno and Emanuel, 1987). Given an initial tropical

disturbance with high values of concentrated vorticity, a low-level wind surge must penetrate for tropical cyclogenesis to be favorable (Gray, 1998; Zehr, 1992). The presence of all these components greatly depends on the large-scale flow. Various components of tropical cyclogenesis have been found to be affected by large-scale variability such as the Madden-Julian Oscillation and the El Niño-Southern Oscillation. A description of these oscillations and how they affect tropical cyclogenesis is discussed in the following sections.

1.3 The Madden-Julian Oscillation

1.3.1 Description

The Madden-Julian Oscillation (MJO) is the dominant mode of tropical intraseasonal variability in the atmosphere. The MJO was initially observed as a significant 40-50 day spectral peak in the zonal wind, temperature, and surface pressure fields with wave-like characteristics (Madden and Julian, 1971, 1972). It is characterized as a large-scale eastward propagating convectively-coupled phenomenon which travels at a phase speed of approximately 5 m/s east of the dateline and propagates uncoupled to convection west of dateline at approximately 10-15 m/s. The MJO has a 30-90 day period and maximum variance at roughly 50 days (Zhang, 2005). Figure 1 captures this MJO life cycle via the propagation of outgoing longwave radiation (OLR) and 850-mb level winds (MJO Working Group).

An MJO event is characterized by eastward propagating anomalous deep convection (represented by negative OLR values in figure 1) typically initiated over the equatorial Indian Ocean. The MJO is composed of out of phase upper and lower level

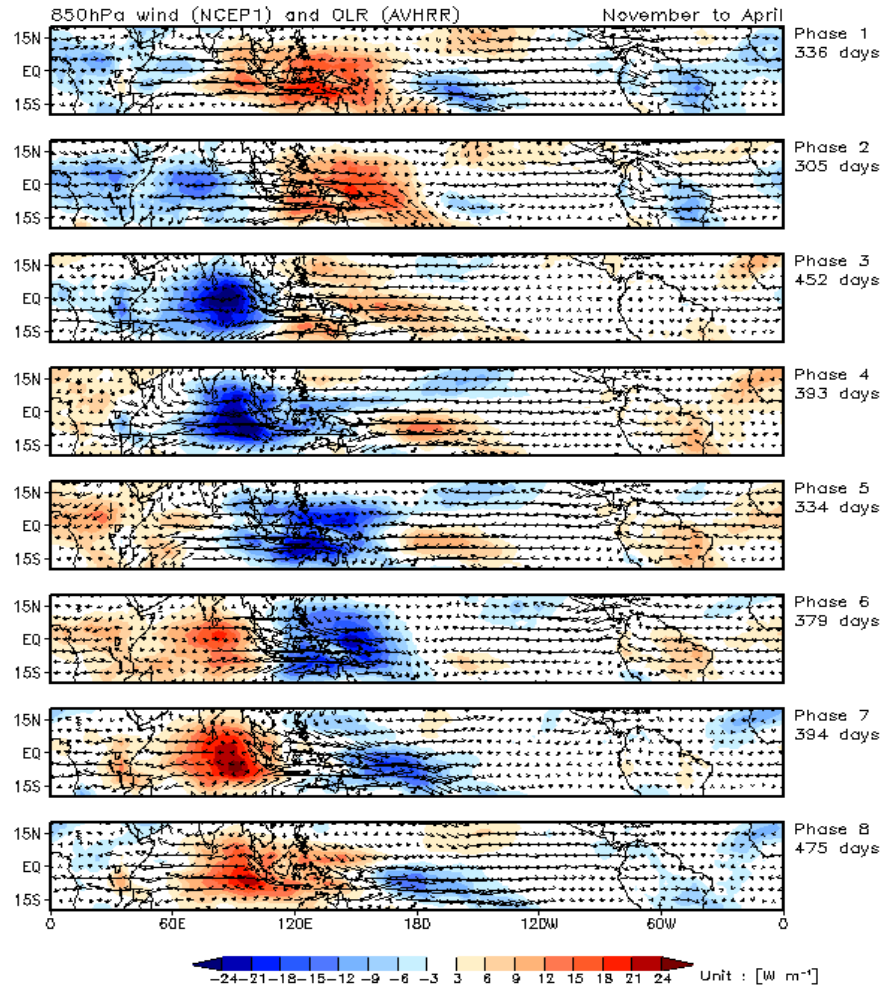


Fig 1: November-April life cycle composite of the MJO. Shown are OLR and 850-mb wind vectors. From the MJO Working Group.

winds and enhanced convection which is preceded and followed by suppressed convection. Over the Indian Ocean, the convective region tends to coincide with upper (lower) level westerly (easterly) anomalies. As the MJO progresses into the Pacific, the region of convection shifts so that it occurs OLR within upper (lower) level easterly (westerly) anomalies (Salby and Hendon, 1994). Within an event, the area of deep convection and related surface flow anomalies cool sea surface temperatures (SST) by more than 1°C through reductions in surface shortwave radiation and enhanced latent heat fluxes

(Shinoda et al., 1999). Cyclonic gyres form behind the areas of strong suppressed convection in the upper-troposphere due to the upper-level divergence created by the rising air of the convective cloud. Likewise, anti-cyclonic gyres follow the areas of enhanced convection. Opposing weaker gyres occur at the surface. These gyres characterize an equatorial Rossby wave response to the slowly-evolving MJO heating. East of the convective core region, the MJO flow resembles a Kelvin wave with upper-level westerlies and low-level easterlies (Salby and Hendon, 1994).

The associated circulation pattern to the MJO resembles that proposed in the Gill (1980) model detailing the atmospheric response to an equatorial heat anomaly on an equatorial β -plane. In this case, the heat source is the latent heat release due to enhanced convection in the MJO. The MJO resembles a slowly-propagating heat source coupled to a Rossby-Kelvin wave response. Low-level Rossby gyres form on both sides of the equator west of the convective core. East of the convection is an equatorially symmetric Kelvin wave response. The heating anomaly evolves more slowly than the time it takes the large-scale circulation response to establish itself (Gill, 1980; Heckley and Gill, 1984). After generation in the Indian Ocean, the MJO convective signal dissipates near the dateline while an uncoupled Kelvin wave continues to propagate east at phase speeds of 10-15 m/s (Rui and Wang 1990; Salby and Hendon, 1994).

The MJO convective extent is concentrated at zonal wave numbers 1-3, while circulation effects peak at zonal wave number 1. The MJO-induced anomalous surface pressure and wind anomalies extend past the dateline in the form of faster uncoupled equatorial waves. The tropospheric low-level MJO signal in the winds is mostly blocked by the Andes Mountains of South America, which inhibits eastward propagation,

therefore the MJO's equatorial circumferential signal is most prominent in upper-level fields (Hendon and Salby, 1994; Madden and Julian, 1994; Zhang, 2005). However, significant MJO signals are observed over the East Pacific and Atlantic basins (Maloney and Hartmann, 2000a, b), including some at low-levels which propagate to the Atlantic via the Isthmus of Panama (Yu et al., 2011).

The MJO has a seasonal cycle with two primary peak seasons. The primary peak corresponds with the Australian summer monsoon. This occurs when the strongest MJO signal is immediately south of the Equator during Australia's summer/fall seasons. The second peak is associated with the Asian summer monsoon when the strongest MJO signal is immediately north of the Equator during boreal summer (Zhang, 2005).

1.3.2 The MJO and East Pacific Tropical Cyclogenesis

Gray (1979) noted the tendency for tropical cyclones to be clustered in space and time. Studies have shown that this tendency may be partially due the MJO. Molinari et al. (1997) observed a reversal of the meridional potential vorticity (PV) gradient over the Caribbean, which met the Charney-Stern necessary conditions for instability (Charney and Stern, 1962). A strengthening of the PV reversal was hypothesized to produce stronger easterly waves and therefore enhance tropical cyclone activity over the East Pacific. This relationship varied on timescales of the MJO, suggesting that MJO activity over the Caribbean and corresponding shear variations are a likely cause for the observed clustering of cyclone activity in the East Pacific (Molinari et al., 1997, 2000).

Molinari and Vollaro (2000) suggested the role of the MJO on East Pacific tropical cyclogenesis as follows:

- 1) Convectively active MJO activity enters the East Pacific and Caribbean.

- 2) A strong PV gradient reversal develops over the western Caribbean and East Pacific regions.
- 3) Unstable waves propagate downstream from the Caribbean into the East Pacific and grow via modal instabilities (Molinari et al., 1997). Unstable waves have also been shown to grow over the East Pacific via nonmodal growth (Sobel and Bretherton, 1999).
- 4) Tropical depressions are generated in correspondence with stronger precursor waves.

To study the effects of the MJO on tropical cyclogenesis Maloney and Hartmann (2000a) use an MJO index based on the first two empirical orthogonal functions (EOFs) of the 20-80 day bandpass-filtered May-November 850-mb zonal wind over the averaged equatorial tropics (index detailed in Maloney and Hartmann, 1998). The EOFs demonstrate an eastward propagating signal; positive values of EOF 1 denote low-level westerlies over the Indian Ocean becoming easterly over the Pacific, while EOF 2 appears as strong low-level westerlies which are often observed to accompany MJO events over the western portion of the Pacific (Lau et al., 1989). MJO phase composites generated from this index indicate an East Pacific zonal wind anomaly maximum near 10°N that varies as a function of MJO phase.

Maloney and Hartmann (2000a) found that when the MJO produces strong low-level westerly anomalies over the East Pacific just north of the Equator, meridional shear of the zonal flow generates cyclonic relative vorticity anomalies to the north of the strongest wind anomalies, associated with increased precipitation. This increase in convection works to amplify the westerly anomalies (Maloney and Esbensen, 2005). The

increase in cyclonic relative vorticity and meridional shear creates favorable conditions for tropical cyclone formation (Gray, 1979). Frictional convergence in this region of horizontal low-level wind shear can produce rising motion; also favorable conditions for tropical cyclone formation. In addition, Maloney and Hartmann (2000a) found low vertical wind shear over the genesis region in association with MJO westerly wind anomalies. The findings in Maloney and Hartmann (2000a) were further confirmed by Frank and Roundy (2006), who found through wave filtering that given a genesis point, the MJO frequency band consists of negative OLR (indicating a region of enhanced convection) and westerly wind anomalies over the East Pacific, which act to increase low-level rotation and convergence.

Furthermore, MJO-induced westerly wind anomalies enhance eddy kinetic energy (EKE) generation from mean low-level flow via barotropic conversion. The resulting eddies form strong precursor disturbances for tropical cyclones over the North Pacific basin. When there are strong westerly anomalies present over the Northeast Pacific, barotropic EKE conversion allows eddies to grow, which supports favorable cyclogenesis conditions given climatologically favorable conditions (Maloney and Hartmann, 2001).

In contrast to periods of MJO westerly wind anomalies and enhanced convection, anomalous MJO easterly winds are associated with anticyclonic vorticity anomalies. The anticyclonic vorticity anomalies are accompanied by suppressed precipitation, low-level divergence, and high vertical wind shear, inhibiting cyclone development (Maloney and Hartmann, 2000a). Associated with strong easterly anomalies is negligible eddy generation through barotropic conversion over the Pacific, further suppressing cyclogenesis (Maloney and Hartmann, 2001).

1.3.3 The MJO and Atlantic Tropical Cyclogenesis

The majority of Atlantic tropical cyclones form off the coast of Africa in association with African easterly waves. Easterly waves and their effects on cyclogenesis have therefore been the focus of many studies (Frank and Clark, 1980; Landsea, 1993; Thorncroft and Hodges, 2001). While tropical disturbance (TD) type waves, such as African easterly waves, are primarily responsible for the formation of tropical cyclones over the Atlantic, the MJO has been shown to affect the environmental conditions, making genesis favorable or unfavorable. Frank and Roundy (2006) observed that when the MJO frequency band is isolated there is often a reduction of the July-September central Atlantic westerly shear near a given point of cyclone genesis.

Maloney and Shaman (2008) analyzed the relationship between the MJO and the 30-90 day precipitation variability over the West African monsoon region (West Africa and eastern Atlantic) and how this relationship affects tropical cyclones. The study found that positive regional precipitation events are associated with an enhancement of eddy kinetic energy in the Main Development Region (MDR; Goldenberg and Shapiro, 1996) and a weakening of the Atlantic trade winds. The strongest enhancement in eddy kinetic energy is observed 5 days after the precipitation event maximum. Approximately 5-10 days after a maximum in regional precipitation, tropical cyclone activity over the MDR is enhanced. In contrast, about 5-10 days before a maximum in precipitation tropical cyclone activity is suppressed over the MDR. About 5 times more tropical cyclones are associated with the enhanced cyclone phase than the suppressed.

Focusing on the MDR, Klotzbach (2010) looked at various field differences per phase of the MJO and found a 99% significance level difference in mean zonal wind, sea

level pressure, and relative humidity between phases 1 and 2 compared to phases 6 and 7 based on the RMM indices of Wheeler and Hendon (2004). Phases 1 and 2 represent convection over Eastern Africa and the Indian Ocean, while phases 6 and 7 are characterized by a convective signal over the western Pacific. Klotzbach (2010) found the largest differences between phases 1 and 2 and phases 6 and 7 to be in the 700-mb relative humidity and the 200-mb to 850-mb zonal wind shear. Wind shear differences are observed to be around 4 m/s, which is similar to the August-October averaged wind shear value difference between very active and inactive seasons. During phases 1 and 2 there is reduced vertical wind shear, lower surface pressure, and increased middle atmosphere humidity over the MDR region. These factors along with cyclonic vorticity anomalies off the coast of Africa make conditions more favorable for tropical cyclone formation and intensification.

In order to quantify the effects of the MJO on tropical cyclone activity, Klotzbach (2010) separated all North Atlantic basin tropical cyclones by values of named storms, named storm days, hurricanes (≥ 64 kt), hurricane days, major hurricanes (≥ 96 kt), major hurricane days, and accumulated cyclone energy by all cyclones. Each cyclone category was separated by phase of the MJO and was found to have statistically significant differences at the 95% level between phases 1-2 and phases 6-7 for all cyclone categories except for named storms. During phases 1 and 2, more than twice as many hurricane days and more than 3 times as many major hurricane days occur than during phases 6 and 7. Moreover, phases 6 and 7 see far less major hurricane strength storm days than phases 1 and 2, a difference significant at the 99% level. Not only are there less major hurricanes observed during phases 6 and 7, but they also tend to have shorter tracks.

Maloney and Hartmann (2000b) investigated the easterly and westerly wind anomalies over the East Pacific due to the MJO and their effects on tropical cyclones over the Gulf of Mexico and Caribbean regions of the Atlantic. During the westerly phase (low-level westerly wind anomalies), low-level cyclonic vorticity over the Gulf of Mexico creates favorable conditions for tropical cyclones. Mo (2000) analyzed a complementary signal in upper-level streamfunction; in association with positive MJO OLR anomalies (suppressed convection) from the western Pacific to the dateline, positive 200-mb streamfunction anomalies form over the eastern tropical Pacific. These anomalies travel over the Gulf of Mexico and western Caribbean regions of the Atlantic. Upper-level easterly wind anomalies are enhanced in these regions resulting in a reduction of vertical wind shear, making conditions more favorable for cyclogenesis. Furthermore, Maloney and Shaman (2008) noted that the MJO accounts for approximately 50% of the amplitude in vertical shear variations over the MDR region during the 30-90 day precipitation events over the West African monsoon region.

In contrast, during the MJO easterly phase there is low-level anticyclonic vorticity over the Gulf of Mexico and the western side of the Caribbean, suppressing tropical cyclone formation and intensification (Maloney and Hartmann, 2000b). Once MJO convection is enhanced over the Indian Ocean, negative streamfunction anomalies at upper levels are observed in the MDR. Upper-level westerlies and vertical wind shear is increased over the MDR, creating unfavorable conditions for storm genesis and intensification (Mo, 2000). Cyclone genesis during low-level westerly periods is shown to outnumber that during easterly periods by about 4 to 1 (Maloney and Hartmann, 2000b). Klotzbach (2010) further confirmed this relationship by performing statistical

analysis on the Gulf of Mexico and northwest Caribbean regions. He found that during the westerly phases, when the MJO amplitude is greater than 1, approximately 4-5 times more tropical storms form than in significant MJO easterly phases.

1.4 El Niño-Southern Oscillation

1.4.1 Description

El Niño-Southern Oscillation (ENSO) is an ocean-atmosphere coupled mode in the tropical Pacific. The Southern Oscillation (SO), the atmospheric component of ENSO, is characterized by a fluctuation in atmospheric pressure between the maritime continent and tropical eastern Pacific, often represented by the pressure difference between Tahiti and Darwin (Rasmusson and Wallace, 1983). These pressure variations are associated with fluctuations in SST, rainfall, and the trade winds. Under normal or neutral ENSO conditions, the tropical Pacific experiences northeasterly (southeasterly) trade winds in the northern hemisphere (southern hemisphere). These trade winds are enhanced in the tropical Pacific associated with the Walker circulation. The Walker circulation is associated with low pressure and deep cumulus convection over the West Pacific warm pool, upper-tropospheric westerly winds, and high pressure over the equatorial eastern Pacific. During neutral ENSO conditions, the trade winds produce upwelling in the equatorial Pacific and off the coast of South America and a deepening of the thermocline in the western Pacific relative to the east (Halpern, 2002). This is manifest in cool SSTs in the East Pacific equatorial waveguide known as the cold tongue, and warmer (by up to 3 to 6 K) SSTs in the West Pacific warm pool. During a La Niña

event, or the cold phase of ENSO, the conditions observed during a normal or neutral phase are amplified (Rasmusson and Wallace, 1983; Chu, 2004).

A warm ENSO event occurs approximately every 2-6 years. It is characterized by tropical Pacific changes relative to normal conditions in various atmospheric and oceanic components. During an El Niño, or warm phase of ENSO, the trade winds are weakened or reversed, becoming westerly. The eastern half of the Equatorial Pacific experiences an increase in SST while west of the dateline SSTs remain near or slightly below neutral conditions (Rasmusson and Wallace, 1983). The low pressure normally occurring over the Pacific warm pool shifts east so that regions in the warm pool such as Indonesia experience drought; meanwhile, islands in the central Equatorial Pacific experience large amounts of rainfall.

Preceding an El Niño event there is a buildup of ocean heat content associated with a deepening of the Pacific thermocline (Meinen and McPhaden, 2000). SST anomalies in the East Pacific induced by the changes in thermocline depth force wind stress anomalies from the west; in turn, the wind stress anomalies support a flattened thermocline across the Pacific and relaxation of the zonal temperature gradient along the Equatorial Pacific that exists under normal conditions. This results in anomalous convection in the East Pacific and associated relaxation of the Walker circulation. Kelvin waves, excited by periodic westerly wind bursts over the western and Central Pacific, may contribute to East Pacific thermocline deepening resulting in anomalously warm SSTs in the East and Central Pacific Equatorial regions (Battisti and Hirst, 1989; Chu, 2004; Rasmusson and Wallace, 1983). The MJO can often produce these Kelvin waves via such westerly wind episodes (McPhaden, 1999).

In conjunction with ENSO-induced SST changes, tropospheric temperature shifts and corresponding fluctuations in tropospheric flow are observed in various parts of the globe (Halpert and Ropelewski, 1992; Horel and Wallace, 1981; Rasmusson and Carpenter, 1981). Various studies have linked ENSO-induced changes in tropospheric flow to tropical cyclogenesis, especially in the Atlantic basin.

1.4.2 ENSO and East Pacific Tropical Cyclogenesis

No conclusive relationship has been found between ENSO and tropical storm frequency in the East Pacific basin. During El Niño and La Niña years, there is no clear distinction in cyclone numbers. However, a relationship was found between ENSO and intense hurricanes (Saffir-Simpson scale cat 3+; Simpson, 1974). Approximately twice as many intense hurricanes are observed during El Niño years compared to La Niña years (Gray and Sheaffer, 1991; Whitney and Hobgood, 1997). A change in tropical cyclone (TC) genesis average longitude is also evident. Tropical storms forming during El Niño events tend to form 5.7° west of the mean origin location when compared to La Niña storm genesis. Storms are more likely to form near the coast of Mexico during a La Niña event (Irwin and Davis, 1999).

Collins and Mason (2000) found that sub-dividing the East Pacific region into two sections clarifies some of the uncertainty in the ENSO-East Pacific relationship. Differences in TC activity environmental parameters between west and east of 116° suggest sub-regional differences due to ENSO. East of 116° environmental conditions tend to be climatologically favorable for cyclogenesis regardless of ENSO phase. West of 116° this is not always the case, hence a significant relationship was found between ENSO and hurricane strength storms in the western region (Collins, 2007; Collins and

Mason, 2000). Collins and Mason (2003) found via multiple regression analysis that this is largely due to variations in relative humidity over the western region. During La Niña events, mid-troposphere dry air associated with the trade-wind inversion (Kloesel and Albrecht, 1989) along with cooler SSTs in the western region of the East Pacific suppress tropical cyclone activity. During El Niño events, the trade-wind inversion is shifted further north. Warm SSTs and deep convection over the equatorial Pacific spreads further north into the western region, allowing for the increase in relative humidity and making conditions more favorable for tropical cyclone activity.

1.4.3 ENSO and Atlantic Tropical Cyclogenesis

The enhanced convection brought on by an El Niño event produces upper-tropospheric anomalous westerly winds over the equatorial Atlantic and the Caribbean regions. Since low-level tropospheric ENSO effects over the Atlantic are small, the upper-level westerly anomalies induce an increase in vertical wind shear, suppressing tropical cyclone activity (Goldenberg and Shapiro, 1996; Gray, 1984a; Gray and Sheaffer, 1991; Landsea et al., 1999; Shapiro, 1987). Furthermore, El Niño events engender subsidence over the western Atlantic, also unfavorable for cyclogenesis. In contrast, during La Niña events there is an enhancement of convection over the western Atlantic which aids in tropical cyclone development (Wyrski, 1982; Chu, 2004). Generally an overall increase in Atlantic TC activity is observed during La Niña events (Gray et al., 1993).

Atlantic cyclogenesis primarily arises from easterly waves that propagate off the west coast of northern Africa. The main development region of these easterly waves, and hence of Atlantic tropical cyclones, is near the entrance of the North African-Asian

(NAA) jet. In order to understand the mechanisms by which ENSO affects tropical cyclones in the Atlantic basin, it is important to understand how ENSO affects the NAA jet. An El Niño-induced increase in deep convection over the equatorial Pacific allows for westward-propagating long stationary barotropic Rossby waves that generate vorticity anomalies and upper-level anomalous westerly winds in the NAA jet region. The westerly wind anomalies increase zonal wind vertical shear, suppressing tropical cyclone formation over the MDR. During boreal autumn, El Niño upper-tropospheric changes induce eastward-propagating stationary barotropic Rossby waves. By October, these eastward-propagating waves generate vorticity anomalies over the Atlantic which disrupt the vorticity anomalies produced by the westward-propagating waves (Shaman et al., 2009).

The maximum ENSO-induced wind shear occurs in July. As the season progresses the vorticity effects due to the autumn eastward-propagating waves along with an observed southward shift of the NAA jet works to suppress westerly anomalies over the MDR region. This southward shift of the jet means the vorticity anomalies produced within the jet, and therefore westerly anomalies, occur south of the MDR. These effects are depicted by a large minimum in wind shear during October, suggesting ENSO effects on tropical cyclone formation are smallest in October.

Even though the largest ENSO-induced wind shear occurs in July, the largest suppression of tropical cyclones for the Atlantic occurs in September due to a large maximum in zonal wind over most of the Atlantic. This September increase in westerly anomalies results from the NAA jet sitting over the northern edge of the larger MDR. This location allows for positive vorticity anomalies due to the westward-propagating

barotropic stationary Rossby waves to form along the core of the NAA jet. The strengthening of the westerly wind greatly constrains tropical cyclone formation (Shaman et al., 2009).

1.5 Medium-Long Lead Cyclogenesis Prediction

1.5.1 Seasonal Prediction

Gray (1979) developed a genesis index using the six climatological genesis components described in section 1.2.2. This seasonal genesis parameter is obtained by multiplying the dynamic potential components by the thermal potential components:

$$sgp = f \times (\zeta_r + 5) \times \left(\frac{1}{(S_z+3)}\right) \times E \times \left(\frac{\partial\theta_e}{\partial p} + 5\right) \times (\overline{RH}) \quad (1.1)$$

where f is the coriolis parameter, $(\zeta_r + 5)$ describes the vorticity, $\left(\frac{1}{(S_z+3)}\right)$ is the inverse vertical shear where $S_z = \left|\frac{\partial V}{\partial p}\right|$ at 750-mb, $E = \int \rho_w c_w (T - 26) dz$ and represents the energy of the ocean with SSTs of at least 26°C down to an ocean depth of 60 m, $\left(\frac{\partial\theta_e}{\partial p} + 5\right)$ is the surface to 500-mb moist stability, and (\overline{RH}) is the 500-700 mb mean relative humidity component which is zero if $\overline{RH} \geq 70$ or $\overline{RH} \leq 40$ (Gray, 1979). This index is found to perform well in reproducing the approximate areas and frequency of tropical cyclones in all basins and seasons.

Gray's work motivated a study by Emanuel and Nolan (2004), where a new genesis potential index was developed. This genesis index is defined as:

$$GP = |10^5 \eta|^{\frac{3}{2}} \left(\frac{H}{50}\right)^3 \left(\frac{V_{pot}}{70}\right)^3 (1 + 0.1 V_{shear})^{-2} \quad (1.2)$$

where η is the absolute vorticity at 850-mb, H is the 600-mb relative humidity percentage, V_{pot} is the potential intensity, and V_{shear} represents the 850-200 mb vertical wind shear. The main difference between the two indices deals with the thermodynamic components. Unlike the Gray (1979) genesis parameter which limits the SST threshold for genesis at 26°C, the new index would allow variations in this threshold so that it may be used in a changing climate. The potential intensity component of the new index depends on the difference between the outflow temperature at the neutral buoyancy level and SST, along with the air-sea disequilibrium. This index is also shown to do a decent job of depicting the total number of cyclones per basin (Camargo et al., 2007).

Statistical research in hurricane prediction began as correlations were found between possible predictors and hurricane activity. These predictors are based on predictable changes in hurricane-favorable conditions, such as those used in the Gray (1979) seasonal genesis index and later the Emanuel and Nolan (2004) index. Gray (1984b) developed a seasonal forecasting method for the Atlantic basin based on ENSO, the Quasi-Biennial Oscillation (QBO; stratospheric equatorial zonal wind fluctuations between westerly and easterly phases), and spring/early summer Caribbean basin mean monthly sea-level pressure anomalies. His forecast scheme included the number of hurricanes per season, the number of tropical storms plus hurricanes per season, and the number of hurricane days per season. A hurricane destruction potential based on the square of a hurricane's maximum wind speed was later added. Hastenrath (1990) verified the performance of the early forecasts, and found them remarkable. The model was later expanded by adding two additional predictors: 200-mb zonal wind and the June-September western Sahel predicted rainfall (Gray et al., 1992; Landsea and Gray,

1992). The model forecasts were issued just prior to December 1st (Gray et al., 1992), June 1st (start of the Atlantic hurricane season; Gray et al., 1994) and August 1st (start of the most active part of the hurricane season; Gray et al., 1993). Forecasts are found using a least absolute deviation (LAD) multiple regression model and include number of named storms, hurricanes, and intense hurricanes (Saffir-Simpson category 3+), along with number of hurricane days, named storm days, and intense hurricane days.

Various advancements in statistical seasonal prediction have been made possible in other studies (Elsner and Schmertmann, 1993; Hess and Elsner, 1994). As noted by Lehmiller et al. (1997), a seasonal forecast informs of the overall amount of seasonal activity expected, knowing only that it will occur sometime during the hurricane season. Lehmiller et al. (1997) developed a seasonal statistical model specifying the presence of TC activity as a function of time within coastal subregions of the Atlantic basin, a useful tool for landfalling hurricane preparedness. Such a model helps solve some of the mystery of tropical cyclone activity within seasonal forecasts, however not in terms of genesis prediction.

1.5.2 Intraseasonal Prediction

Intraseasonal (from 10-60 days; Vitart et al., 2010) prediction is an ideal forecast range for temporal genesis prediction. Leroy and Wheeler (2008) generated an intraseasonal multiple logistic regression model to predict southern hemispheric weekly tropical cyclone activity. This model included 5 possible predictors: two real-time MJO indices (RMM1 and RMM2) developed by Wheeler and Hendon (2004), two leading VARIMAX rotated principal components of monthly standardized SST anomalies where the first EOF depicts ENSO, and lastly the climatological seasonal cycle of tropical

cyclones. All predictors are lagged to their real-time availability in order to ensure a real-time model. They divide the study region into four zones and use the model to predict the probability that at least one cyclone will form in each zone at any given week.

Hindcasts were generated as a form of cross-validating the model, and Brier skill scores and reliability diagrams were used to assess the skill and reliability of the model (Leroy and Wheeler, 2008). Since the development of the Leroy and Wheeler (2008) southern hemisphere model, the model has been expanded by including a gridded framework of overlapping regions in the Southern Hemisphere, allowing for spatial variability in the predictors. Furthermore, the Indian dipole mode index (Saji et al., 1999) and the Trans-Niño index (Trenberth and Stepaniak, 2001) have been included as predictors in the model (Vitart et al., 2010). This real-time prediction model is currently operational for southern hemisphere cyclones.

An empirical method of intraseasonal statistical prediction of TC probabilities was developed by Paul Roundy (see <http://www.atmos.albany.edu/facstaff/roundy/tcforecast/tcforecast.html>). The model predicts tropical cyclone activity in all major basins, including the East Pacific and Atlantic, and is based on the relationship between TCs and various wave modes as discussed in Frank and Roundy (2006). The predictors include Kelvin waves, mixed Rossby-gravity waves, convectively coupled equatorial Rossby waves, easterly waves, the MJO, and ENSO. These are generated via the filtering of the wavenumber-frequency spectrum of OLR and the implementation of EEOF (Extended EOF) analysis (Roundy and Schrek, 2009). A caveat in generating the predictors from OLR, as noted by Frank and Roundy (2006), is that there are instances in which waves will affect TC genesis without significantly altering the OLR pattern but

rather through fluctuations in low-level vorticity and/or vertical shear. An example of this is the MJO effects on the East Pacific and Atlantic basins, as discussed in section 1.3.

Dynamical forecasting models of TC activity in intraseasonal time scales have also been developed. An issue with dynamical general circulation models (GCMs) is that they often poorly simulate the MJO (Slingo et al., 1996; Lin et al., 2006). Furthermore, TC representation tends to vary between numerical models (Vitart, 2006). The European Centre for Medium-Range Weather Forecasts (ECMWF) Integrated Forecast System (IFS) has been shown to do a relatively adequate job simulating the MJO and its effects on TCs (Vitart, 2009), although it has a tendency to produce MJO events that propagate too slowly and are about 25% too strong after the day 10 forecast (Vitart and Molteni, 2009).

Vitart et al. (2010) provides a comparison between the ECMWF forecast system over the Southern Hemisphere and the statistical model developed by Leroy and Wheeler (2008), including the gridded framework and predictor improvements to the statistical model as previously discussed in this section. The models are compared for November-April hindcasts, concurring with the season and region of highest MJO activity.

Hindcasts are generated out to a 3 week lead. ECMWF 46-day hindcasts from 1989 to 2008 are generated consisting of 15 ensemble members (one being a control run) with 62 vertical levels and a T399 resolution (~50km grid). The ensembles are integrated for 10 days and are forced by persisted SST anomalies. The model is coupled to an ocean GCM (HOPE; Wolff et al., 1997) every 3 hours and the resolution is lowered to T255 (~80km) after 10 days. Initial conditions are taken from the ERA-40 reanalysis dataset (Uppala et al., 2005) until 2001 and from the ECMWF operational analysis thereafter. For more details see (Vitart et al., 2010).

Forecast reliability and skill over equal grid spaces are compared between the statistical and dynamical model. Reliability diagrams found that the ECMWF hindcasts had a tendency to overproduce high probabilities of TCs for all 3 week leads, a common issue among dynamical models. This is depicted by a flatter reliability curve, whereas a perfect forecasting model lies along the 45° diagonal line. Reliability curves are further discussed in section 5.2. Vitart et al. (2010) noted this overestimation is likely because the model had a tendency to produce approximately 30% more TCs than was observed in the time period of the study. In terms of skill, the statistical model was shown to have a higher Brier skill score than ECMWF for week leads 2 and 3; however, ECMWF had a higher Brier skill score at a week 1 forecast lead. Brier skill scores are discussed in more detail in sections 2.5 and 5.1.

The statistical model was found more reliable and showed higher skill past a week 1 forecast lead, however there are caveats. For example, the sharpness (the capability of the model to deviate from its mean climatology) of the dynamical model is better than that of the statistical model. Vitart et al. (2010) found that the ECMWF forecasted probabilities between 0% and 100%, even at the week 3 forecast lead. The statistical model, however, rarely predicts a 0% probability and probabilities only range up to 70% in the time frame of the study. It is common amongst statistical models to not predict very low or very high probabilities.

Vitart et al. (2010) did find improvements to the dynamical ECMWF model by calibrating it to reduce the overestimation of TC occurrences over the Southern Hemisphere. Furthermore, the study found that combining the statistical and calibrated dynamical forecasts by averaging the forecasted probabilities increased the skill of the

week 2 and 3 forecasts by an amount significant at the 95% level. ECMWF forecasts past week 3 are also shown to be less skillful likely because of the model's difficulty to properly propagate the MJO across the Maritime Continent (Vitart and Molteni, 2009). Improvements to the ECMWF since the version of the model in the Vitart et al. (2010) study include an improvement in the model's tendency to produce MJO events that are too strong, although the issue has not been fully resolved (Vitart and Molteni, 2009).

The Climate Prediction Center (CPC) provides the Global Tropics Hazards and Benefits Outlook for a week 1 and week 2 forecast lead to forecast the likelihood of rainfall and tropical cyclone formation globally. The model uses tropical atmospheric waves such as those described in Frank and Roundy (2006), extratropical interactions such as frontal systems in the lower mid-latitudes, and other climate variability modes such as ENSO and the MJO. The product utilizes both statistical and dynamical forecasts, including statistical MJO forecasts, the Global Forecast System (GFS), and the Climate Forecast System (CFS). Implications of the model include issues simulating a realistic MJO in the dynamical models. Furthermore, the model currently lacks a quantification of hazard probabilities (it currently forecasts qualitative likelihoods such as "high" and "moderate"), which they hope to implement via multi-model approaches (CPC, see <http://www.cpc.ncep.noaa.gov/products/precip/CWlink/ghazards/index.php>; US CLIVAR, see [www.usclivar.org/Organization/MJO WorkingGroup/MJO-Hazards.html](http://www.usclivar.org/Organization/MJO%20WorkingGroup/MJO-Hazards.html)).

1.6 Overview of Study

Using a similar multiple logistic regression method as Leroy and Wheeler (2008), a model for the prediction of weekly tropical cyclone genesis probabilities is created for both the East Pacific and Atlantic basins. Section 2 describes the data sets used and includes a methodology. The methodology explains the predictor selection and development, along with logistic regression and forecast verification methods. Section 3 focuses on predictor and model justification. Section 4 details the hindcasted results based on the full model. Section 5 discusses the skill and reliability of the model. Lastly, section 6 summarizes the model results, and future work is discussed.

2. Data and Methodology

2.1 Data

2.1.1 HURDAT

The National Hurricane Center (NHC) Hurricane best track (HURDAT) is an ideal tropical cyclone archive for this study as it contains 6 hourly latitude and longitude information for tropical cyclones in the East Pacific and Atlantic dating back to 1851, along with minimum central pressure and maximum sustained 1-minute surface winds (Neumann et al., 1999). This study uses data from 1975-2009, which is available as observations from the HURDAT archive at 0000, 0600, 1200, and 1800 GMT. The year 1978 is excluded from all analysis due to a lack of RMM data (discussed in section 2.1.3), and hereafter assumed in any mention of the period 1975-2009. For the time period of this study, the cyclone data is predominantly collected from organized aircraft reconnaissance and weather satellites containing infrared and visible sensors (Jarvinen et al., 1984).

This study primarily focuses on the probability of cyclogenesis occurrence within a given week. For the East Pacific Ocean basin, the official hurricane season of May 15-November 30 is used. For the North Atlantic Ocean basin, a more restrictive subset of the official hurricane season, July 1-October 31, is used. These subsets of the data were selected to remove possible anomalous outliers which could distort the results. In the

case of the Atlantic, better results were yielded using a more active subset. To exclude weaker systems, only storms that reach a minimum of 34 knots, or tropical storm strength, are considered. The model of choice, discussed further in section 2.3, allows input observations to be dichotomous; since the desired probabilities are weekly, a 0 is assigned for any week where no storm formed and a 1 if at least one storm formed.

Figure 2 illustrates all cyclogenesis points used in this study for both the East Pacific and North Atlantic basins. The East Pacific domain is bounded by 90°W-120°W, 5°N-25°N; the Atlantic is bounded by 15°W-100°W, 5°N-50°N. The East Pacific is bounded at 120°W in accordance with the Collins and Mason (2000) findings of separating the western and eastern regions of the East Pacific, as discussed in section 1.4.2.

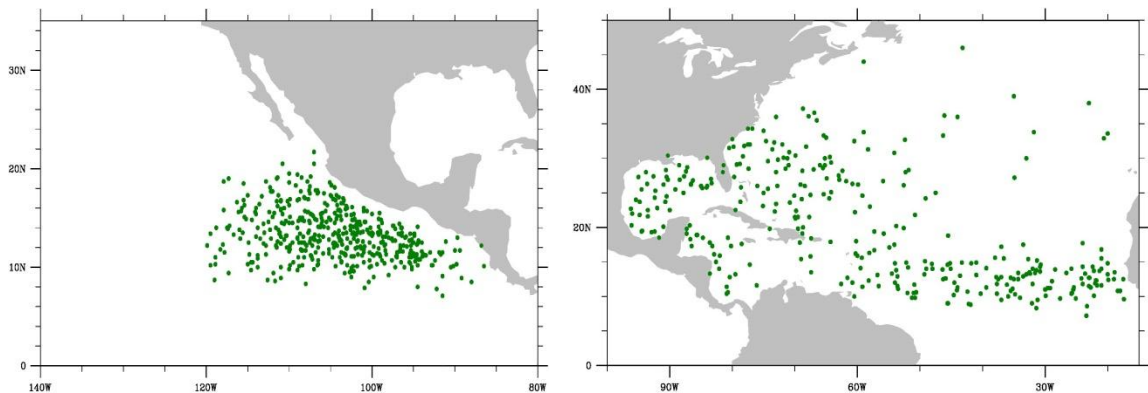


Fig 2: Tropical cyclogenesis locations for 1975-2009 for the East Pacific ocean basin (left) bounded by 90°W-120°W, 5°N-25°N, and the North Atlantic ocean basin (right) bounded by 15°W-100°W, 5°N-50°N.

2.1.2 HADISST

The Hadley Centre Sea Ice and Sea Surface Temperature (HadISST) re-analysis dataset is used to develop an ENSO index via use of East Pacific SSTs. HadISST is a globally-complete 1° gridded dataset including SSTs and sea ice concentration data

(Rayner et al., 2003). The dataset is available from 1871-present, where the data is obtained from a combination of satellite AVHRR (Advanced Very High Resolution Radiometer) and in-situ observations. SST data available up to 1981 is based on in-situ observations, and is therefore more inhomogeneous in terms of coverage. Oceanic data sparse regions are interpolated using a reduced space optimal interpolation (RSOI) forming a 4° grid from 1871-1948, and a 2° grid thereafter. The RSOI method, which utilizes EOF analysis, is applied to a combination of satellite and in-situ data from 1982 onward. This interpolated dataset using RSOI is then combined with the bias-adjusted, gridded, non-interpolated in-situ data to reestablish some of the smaller scale variance. The satellite data utilizing AVHRR SSTs use a regression of brightness temperatures from infrared channels onto buoy SST data and is then gridded to have a 1° resolution. Biases associated with aerosols and clouds are adjusted by calculating a smoothed biased field and subtracting it from the data. In this study, only a region of the Equatorial East Pacific SSTs is used (5.5°S - 4.5°N, 89.5°W - 149.5°W) from 1975-2009 to calculate an El Niño index.

2.1.3 NOAA Interpolated OLR

An OLR dataset constructed from the National Oceanic and Atmospheric Administration (NOAA) polar-orbiting satellites is used by Wheeler and Hendon (2004) in the construction of two indices, which are used in this study, representing the eastward propagation of the MJO. The dataset includes OLR data from daytime and nighttime orbits in 2.5° x 2.5° global grids (Liebmann and Smith, 1996). To ensure values do not unrealistically deviate too far from neighboring grids, a grid point is set to missing if there is a difference greater than 49 W/m² between the grids; this criterion is altered if the

grid point is surrounded by any missing values. Furthermore, any data likely to be in error is removed. These include values less than 50 W/m^2 ; between 90°N - 60°N and 45°S - 90°S : daytime values greater than 325 W/m^2 and nighttime values greater than 300 W/m^2 ; between 57.5°N - 42.5°S : daytime values greater than 400 W/m^2 and nighttime values greater than 300 W/m^2 .

Missing values are interpolated in space and time for daytime and nighttime values separately. First, temporal linear interpolation is used on 1-day gaps. Second, a spatial interpolation of missing values is computed by averaging the non-diagonal neighboring values if at least 3 are non-missing. This procedure follows another 1-day interpolation in time. Next, another spatial interpolation is calculated given 2 or more non-missing neighboring values. Spatial and temporal interpolations continue until all missing values are filled. Following the interpolation procedure, the data is once again checked to ensure values not unrealistically deviate too far from neighboring grids. Lastly, the daytime and nighttime values are averaged into daily averages. Values from March 17-December 31, 1978 are missing from the dataset.

2.1.4 NCEP/NCAR 40-Year Reanalysis

The National Centers for Environmental Prediction (NCEP) and the National Center for Atmospheric Research (NCAR) produced a global 40-year reanalysis dataset consisting of various atmospheric fields with data beginning in 1957 (Kalnay et al., 1996). The upper and lower level wind fields in the dataset are used in the calculation of the Wheeler and Hendon (2004) MJO indices used in this study. Data used in the reanalysis includes the Comprehensive Ocean-Atmosphere Data Set (COADS; includes data from fixed and drifting buoys, ships, and ocean station data), global rawinsonde,

aircraft, land surface, satellite, and pibal (pilot balloon) data. The satellite data includes Special Sensing Microwave/Imager (SSM/I) surface wind speed data and cloud drift winds from the Geostationary Meteorological Satellite (GMS). A consistent method of data assimilation utilizing a global NCEP spectral model and a complex quality control scheme is used throughout the dataset. Zonal and meridional winds are available for 17 vertical levels in 2.5° global grids and are classified as A in the reanalysis, meaning the fields are well defined by observations and statistical interpolation allows for a better estimate of the field than via observations alone; this is compared to classification B, which are fields well defined by the observations but have been greatly influenced by the model parameters used in data assimilation, and classification C, which are fields fully determined by the model during data assimilation. For more details see Kalnay et al. (1996).

2.2 Predictor Development

2.2.1 Climatology

The first predictor developed for the model is a climatology of tropical cyclone genesis. A raw climatology is made by taking the weekly stratified dichotomous genesis observations and averaging each week over all years. This results in a weekly probability that is then multiplied by 100 to depict a climatological percent probability of genesis. The raw climatology is smoothed by applying a weighted running average with a 1-2-1 filter four times for the Atlantic and twice for the East Pacific. The climatology of each basin is plotted in figure 3, where the dashed black curve represents the raw weekly

climatology and the smoothed version is in solid red. The smoothed climatology is used as the predictor in the finalized prediction model.

The East Pacific climatology is less filtered than the Atlantic in order to preserve the probability minimum in late July and early August. This minimum is likely due to the midsummer drought (Magaña et al., 1999). In late July and early August, a decrease

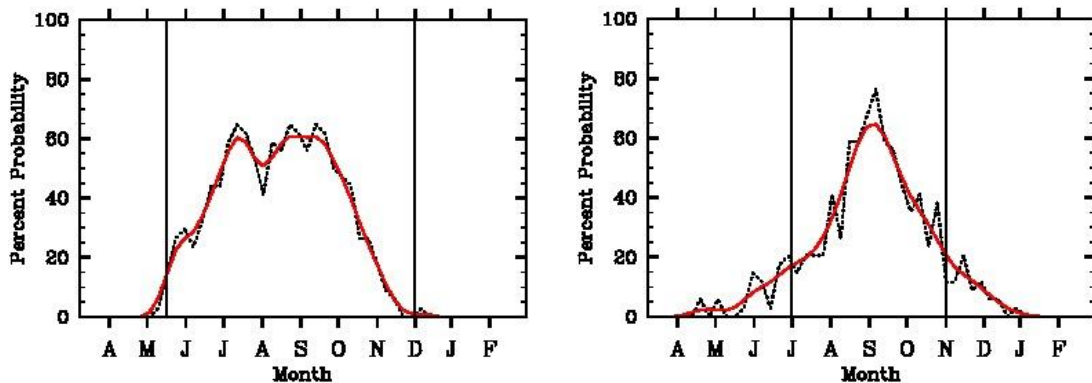


Fig 3: Climatology of tropical storm cyclogenesis probability (%) for 1975-2009 for the East Pacific Ocean (left), and the Atlantic Ocean (right). The black dashed curve is a raw weekly stratified climatology. The red solid curve is a smoothed climatology, smoothed with a 1-2-1 filter. The x-axis ranges from March-February. Vertical lines represent time range boundaries used in the data.

in tropical cyclone activity is observed due to a deep convective activity minimum in Mexico and adjacent regions of the East Pacific. This midsummer drought causes changes in low-level flow such that low-level winds become easterly, making environmental conditions less favorable for cyclogenesis (Magaña et al., 1999).

2.2.2 Leading Modes of SST

The next two predictors considered in this study are the first two principal components (PCs) of tropical East Pacific SST. To formulate the predictor indices, a 3-point running mean average is applied to the monthly SST data to reduce intraseasonal influence. The annual cycle and long term mean are removed and the data is detrended.

The monthly data is then linearly interpolated to daily resolution and cosine weighted according to latitude. The first two EOFs are calculated via the covariance matrix for 5.5°S- 4.5°N, 89.5°W - 149.5°W. Figure 4 illustrates the first 2 EOFs calculated but over a larger domain (30°S- 30°N, 70°W-110°E). This is done to show a more coherent picture of the leading modes of SST variability over the Equatorial East Pacific. Hatched over EOF1 in figure 4 is the El Niño 3 region used for the index calculation. Also discussed is the El Niño 4 region hatched over EOF2 (5.5°S-4.5°N, 150°E-160°W). The first EOF of SST shown in figure 4 represents the leading mode in SST variability over the Equatorial East Pacific. This mode is representative of ENSO, characterized by the Equatorial East Pacific warming of SSTs coinciding with SST cooling over the western Pacific. The second EOF is representative of the El Niño Modoki, or Central Pacific El Niño. This event is characterized by Central Pacific warming events and is a fairly recent topic of study. El Niño Modoki events are believed to be a result of recent global warming; this theory was hypothesized because El Niño Modoki events were first observed in the 1990s (Yeh et al., 2009). Kim et al. (2009) found that during these Central Pacific warming events (defined using an index derived from SSTs over the El Niño 4 region), there is an increase in Atlantic basin tropical cyclone activity. However, since 1950 only 5 years of the Kim et al. (2009) study were representative of Central Pacific warming events. Due to the rarity of the event, the Central Pacific warming event is not used in the final statistical model developed in this study.

In the development of an El Niño 3 index, the first PC is standardized and analyzed to be a possible predictor. PC1 represents the time series of EOF1, in this case the temporal variability of ENSO. To ensure that a proper El Niño 3 index has been

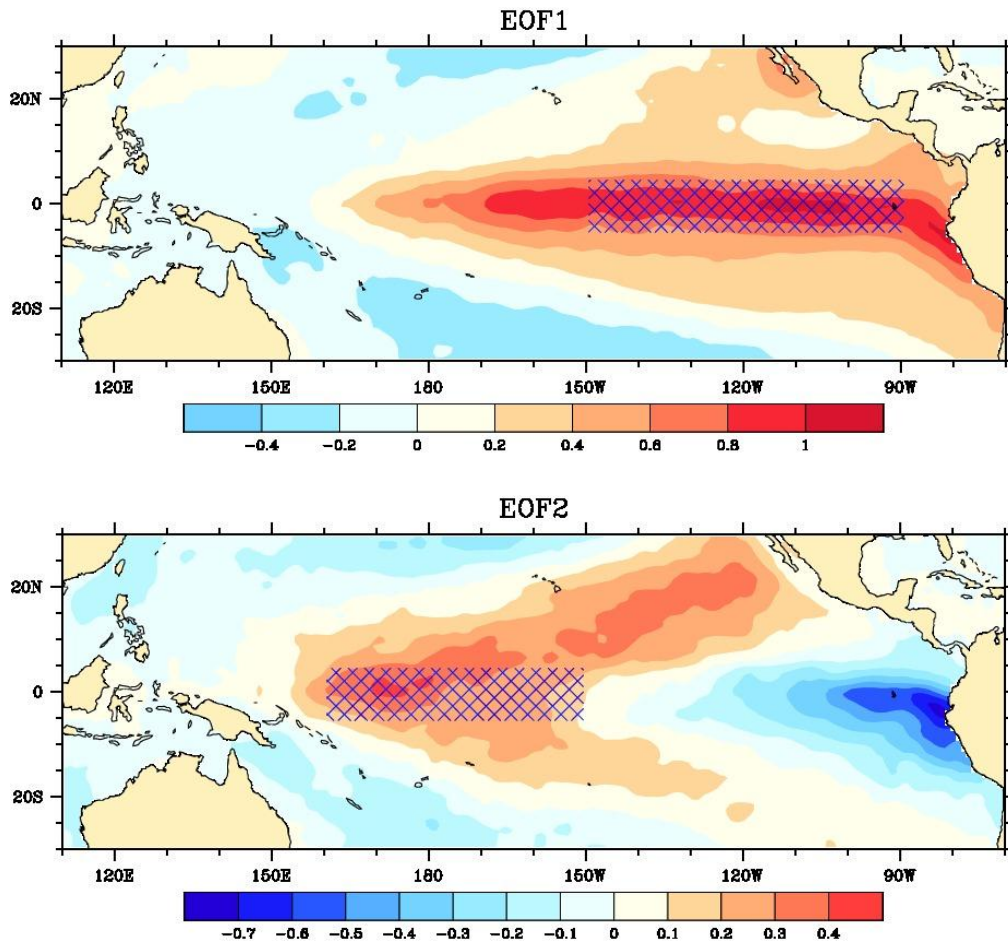


Fig 4: Leading modes of SST over the Equatorial East Pacific. Over the full domain, EOF1 (top) explains 51% of the total variance and EOF2 (bottom) explains 13% of the variance. An El Niño 3 region is used for the calculation of the predictor indices and is hatched in blue (5.5°S- 4.5°N, 89.5°W - 149.5°W) in the EOF1 plot. EOF analysis over the El Niño 3 region is calculated separately and used in the index calculations; in this smaller domain EOF1 explains 89% of the variance while EOF2 explains 6% of the variance. The hatched region over EOF2 represents an El Niño 4 region (5.5°S-4.5°N, 160°E-150°W).

developed, a correlation between PC1 and the Climate Prediction Center (CPC) Optimum Interpolation (OI) Niño 3 SST index is computed (for index documentation, see Reynolds et al., 2002). Since the CPC OISST is available beginning in 1982 and is provided as a monthly average, this correlation uses only data from 1982-2009 and the CPC OISST index is interpolated to daily values. We find that the correlation between the two daily indices for the given time period is 0.96. The second PC over the El Niño 3 region is also

tested for a possible relationship with East Pacific and Atlantic TC activity, although not used in the finalized model.

2.2.3 RMM Indices

Wheeler and Hendon (2004) developed two real-time multivariate MJO (RMM) indices used to represent the eastward propagation of the MJO. These indices are derived from the first two EOFs of the near-equatorially (15°S - 15°N) averaged and normalized 200-mb and 850-mb zonal wind fields and satellite OLR. Values are normalized by dividing by the field's global variance prior to EOF analysis. Preceding EOF analysis the fields are detrended, the seasonal cycle is removed, a daily measure of ENSO is subtracted from the fields, and to remove any other aspects of interannual variability, a 120-day average of the preceding 120 days is subtracted from the fields. The EOFs, shown in figure 5 (figure 1 in Wheeler and Hendon, 2004), represent the propagation of the MJO; EOF 1 depicts low-level easterly winds, upper-level westerly winds, and enhanced convection (negative OLR) over the Maritime Continent. EOF2 winds are in approximate quadrature to those in EOF1, with enhanced convection over the Pacific. The daily observed data is projected onto the computed EOFs to yield the two PCs, or time series, of the EOFs. These PCs, called RMM1 and RMM2, mostly vary on the timescale of the MJO.

The daily OLR data used to construct the multivariate EOFs are averaged values ranging from 1979-2001. These values, obtained from the NOAA interpolated OLR dataset, along with the NCEP/NCAR 40-year reanalysis of upper and lower wind field data for the same time period, are used to calculate the EOFs. Real-time OLR data is acquired directly from NCEP. The RMM indices are available from June 1974 to March

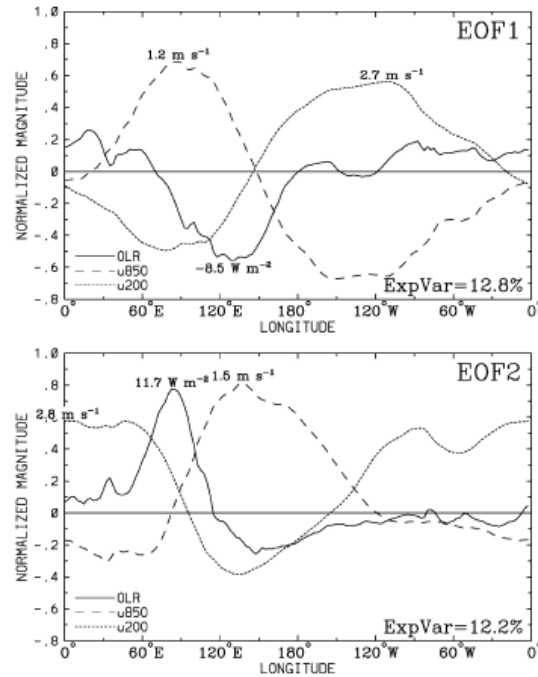


Fig 5: EOF 1 (top) and EOF 2 (bottom) spatial structures calculated from the combination of OLR, 850-mb wind (denoted u850 in legend), and 200-mb wind (denoted u200). Values are plotted as a normalized magnitude. From Wheeler and Hendon (2004).

16, 1978, and January 1979 to present, by projecting onto the calculated EOFs. The discontinuity in 1978 is due to the availability of the OLR satellite data. For this reason, 1978 is not used in this study and is excluded from all datasets. The RMM indices developed by Wheeler and Hendon (2004) are used in this study and are available at <http://cawcr.gov.au/staff/mwheeler/maproom/RMM/>.

2.3 Logistic Regression

The prediction model developed in this study employs multiple logistic regression. Regression methods are ideal for distinguishing the relationship between an independent variable (the predictor) and an outcome variable (the response). According to Hosmer and Lemeshow (2000), the idea is to find the best possible fit while reducing

the number of parameters. Multiple logistic regression allows for the use of various independent predictor variables to find the ideal fit. The model is formulated as follows:

$$\hat{P}(x) = P(Y|x) = \frac{e^{\beta_0 + \beta_1 x_1 + \beta_2 x_2 + \dots + \beta_m x_m}}{1 + e^{\beta_0 + \beta_1 x_1 + \beta_2 x_2 + \dots + \beta_m x_m}} \quad (2.1)$$

Equation (2.1) represents the conditional probability that the dichotomous variable Y occurs given the independent variables, x_m , where m is the number of independent variables. The regression coefficients are represented by β_m . This form of regression is unique in that its output yields a probability between 0 and 1. The first step to finding the outcome probabilities is calculating the regression coefficients. This is done using a least squares approach via a maximum likelihood function defined by:

$$l(\beta) = \prod_{i=1}^n \hat{P}(x_i)^{y_i} [1 - \hat{P}(x_i)]^{1-y_i} \quad (2.2)$$

where y_i and x_i indicate the dependent and independent variables, respectively, at time step i for n total time steps. In maximum likelihood the idea is to select the regression coefficients which maximize the value of $l(\beta)$. For simplicity, the log of this equation is calculated and given by:

$$L(\beta) = \ln[l(\beta)] = \sum_{i=1}^n \{y_i \ln[\hat{P}(x_i)] + (1 - y_i) \ln[1 - \hat{P}(x_i)]\} \quad (2.3)$$

To maximize the value of $L(\beta)$, the derivative of equation 2.3 with respect to β_m is calculated and set equal to zero. This results in the non-linear likelihood equations, expressed as:

$$\sum_{i=1}^n [y_i - \hat{P}(x_i)] = 0 \quad (2.4)$$

$$\sum_{i=1}^n x_i [y_i - \hat{P}(x_i)] = 0 \quad (2.5)$$

These equations are generally solved with an iterative weighted least squares scheme (McCullagh and Nelder, 1989). The results yield the maximum likelihood

estimates for the regression coefficients. The regression coefficients can then be used to find the probability that the dichotomous variable Y occurs given new values of the predictors (Hosmer and Lemeshow, 2000).

In this study, probability hindcasts using equation 2.1 are generated independently for each year from 1975-2009. Hindcasts are a form of cross-validation, utilizing regression coefficients calculated using the full time range while excluding the hindcasted years. The regression coefficients are then used to “forecast” the excluded year (Elsner and Schmertmann, 1994). Hindcasts are generated out to a seven week lead (i.e., a four week lead would use today’s predictor data to predict the probability of a storm developing four weeks from now). Probability hindcasts generated are further discussed in section 4.

In order to eliminate any possible bias in the model with a storm forming within a certain day of the week, a week is defined beginning on every day, resulting in overlapping weekly probabilities. No communication between weeks (i.e. stratified weeks) would allow the possibility of tropical cyclone probabilities less than one week long. For example, given overlapping weeks (as done in this model), if a cyclone was to form on a given Wednesday, this would be observed beginning 7 days before the actual event (the previous Thursday). This represents a cyclogenesis occurrence observed in the week beginning Thursday and ending the next Wednesday. However, if, say, Monday is defined as the beginning of each stratified week and a cyclone forms on Wednesday, a cyclone would not be observed until that Monday; this results in a 3 day week of an observed cyclogenesis event, beginning Monday and ending Wednesday. Given weekly

overlapping tropical cyclone genesis observations, relationships between the observations and the predictors are observed in full one week intervals.

2.4 Sequential Forward Selection

Stepwise selection schemes are commonly used in regression as a basis for determining the importance of a variable, including it only if significant given a specific criterion (Hosmer and Lemeshow, 2000). In this study a sequential forward selection scheme is used. Variables are sequentially included to an initially empty set until the addition of further variables no longer improves prediction, meaning it no longer decreases the criterion. Typically this test for significance, called the likelihood ratio test, is done by comparing the log likelihood (equation 2.3) of the model with and without a particular variable. It's represented by:

$$D = -2 \ln \left(\frac{L(\beta)}{L(\beta)_s} \right) \quad (2.6)$$

where $L(\beta)$ denotes the likelihood of the fitted model and $L(\beta)_s$ is the likelihood of the saturated model, or the model which includes all the predictors. Substituting equation 2.3 into 2.6 yields:

$$D = -2 \sum_{i=1}^n y_i \ln \left[\frac{\hat{P}(x_i)}{y_i} + (1 - y_i) \ln \left(\frac{1 - \hat{P}_i}{1 - y_i} \right) \right] \quad (2.7)$$

Equation 2.7 is known as the deviance, analogous to the residual sum of squares in linear regression, and follows a chi-square distribution (Hosmer and Lemeshow, 2000). In the model developed here, deviance is used as the criterion in the forward selection scheme. The forward selection scheme stops once deviance can no longer be reduced, so there is no advantage in including the other predictors. Using an inverse chi-square cumulative distribution function at 1 degree of freedom, the 95% significance critical

value is found, meaning there is a 5% chance that the deviance between the model with and without a variable came by chance. One degree of freedom is used because a single variable is being added at a time in stepwise regression. This critical value is the minimum deviance difference value allowed in the selection scheme; if the value becomes less than the critical level the iterations terminate (MATLAB, 2011b, The MathWorks).

2.5 Forecast Verification

The most common method for verification of dichotomous events is the Brier score (BS), defined by the equation:

$$BS = \frac{1}{n} \sum_{i=1}^n (y_i - o_i)^2 \quad (2.8)$$

where y_i represents the forecasted probability between 0 and 1 for event i out of a total of n events (Wilks, 2006). The observations, o_i , are dichotomous where $o_i = 1$ if the event occurred and $o_i = 0$ if it did not occur. The Brier score calculation in essence calculates the mean-squared error of the forecasted probability. Since both the forecasts and observations are bounded by 0 and 1, so is the Brier score. A Brier score of 0 denotes a perfect forecast, meaning o_i always equals y_i . In contrast, a Brier score of 1 indicates that the forecast is wrong for every event. Using the Brier score calculated, a Brier skill score is then computed:

$$BSS = \frac{BS - BS_{ref}}{0 - BS_{ref}} = 1 - \frac{BS}{BS_{ref}} \quad (2.9)$$

where BS is the Brier score calculated from the forecasts and BS_{ref} represents a reference forecast Brier score. This study utilizes a seasonal mean climatology to calculate the reference Brier score (discussed in section 5). The Brier skill scores are

multiplied by 100 to denote a percentage. This is ideal as it allows the Brier skill score to represent a percent decrease in mean squared error (by the forecasts) over a mean seasonal climatology. A Brier skill score of 100% is achieved when every forecasted probability is perfect. A BSS of 100% is not possible with this statistical model due to the low sharpness limitation associated with the use of statistical models as mentioned in the introduction.

3. Predictors

3.1 Predictor Justification

The predictors considered in this study includes a smoothed climatology of tropical cyclone genesis for each basin, two MJO indices (RMM1 and RMM2), and two indices based on the first two EOFs of SST in the El Niño 3 region. While physical reasoning between the possible predictors and tropical cyclone genesis are discussed in the introduction, it is possible that a predictor will either not show a strong enough relationship with TC genesis to be used for prediction or not be a good fit for logistic regression. In this section statistical analysis is used to determine if each predictor is a good fit for the finalized model.

3.1.1 Climatology

Climatology is based on the tropical cyclone genesis data, so there is a natural strong relationship between genesis and its climatology. To determine if logistic regression is a good fit for climatology, univariate logistic regression models are calculated for each basin and illustrated in figure 6. The smoothed, stratified climatology (red curve in figure 3) is interpolated from weekly probabilities to daily to allow the univariate models to begin each week on every day. Climatology is the only predictor not lagged out to a 7 week lead because it is based on all other years excluding the forecasted year, meaning it is always known and is therefore the same for all forecast leads. The x-axis in figure 6 represents the smoothed, stratified climatology values from

figure 3, while the y-axis is the probability of a tropical cyclone observation occurring within a certain climatological probability range. The East Pacific (Atlantic) tropical cyclone observations are binned into 20 (17) bins of approximately 340 (246) values each and averaged. For example, the probability of an East Pacific cyclogenesis event in June is between 25% and 45% according to figure 3, therefore that event would be binned according to its climatological probability (between 25 and 45 in the x-axis of figure 6). The logistic regression models (solid curves) are calculated independently of the averaged probabilities (dots).

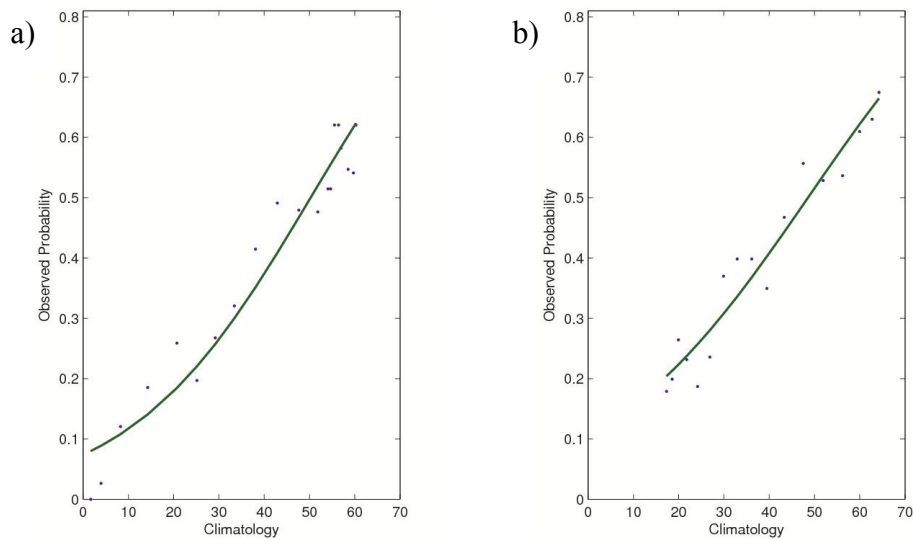


Fig 6: Univariate logistic regression curves fitted for tropical cyclogenesis climatology for the a) East Pacific Ocean and b) Atlantic Ocean. Genesis observations are binned according to their corresponding climatological value and averaged (dots). Logistic regression models (solid curves) are calculated independently.

Sensitivity tests found that the relationship between the averaged probabilities and the logistic curves is not a factor of the number of bins; increasing the number of values in each bin results in less averages (dots) about the fitted line while decreasing the number of values in each bin results in more averages about the fitted line, however the

deviation of the averages from the curve is unchanged. The fit appears to support the choice of model. The goodness of fit (the strength of the relationship) between the logistic curves and the binned averages is discussed in section 3.1.4.

3.1.2 The MJO

In order to illustrate the relationship between the MJO and cyclogenesis, genesis locations are binned according to MJO phase as defined by Wheeler and Hendon (2004) and plotted in figure 7. Weak MJO events, denoted when $\sqrt{(RMM1^2 + RMM2^2)} < 1$, are excluded. North Pacific results are shown from May 15 to Nov 30 data (fig 7a), while the Atlantic basin results are displayed for July 1 to Oct 31 data (fig 7b).

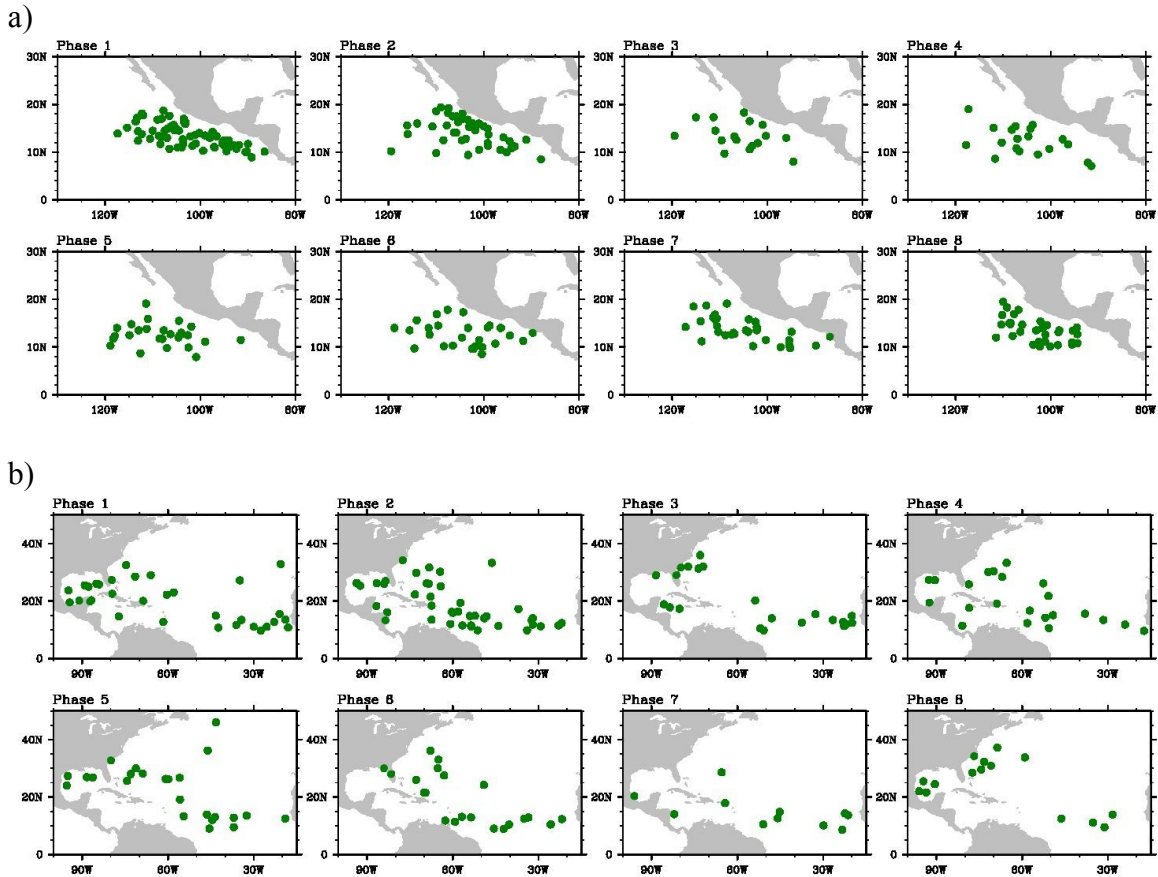


Fig 7: Tropical cyclone genesis locations per phase of the MJO for 1975-2009 for a) East Pacific, using May 15-Nov 30 data, and b) North Atlantic, using July 1-Oct 31 data. Only storms reaching a minimum of 34 kt (tropical storm strength) are considered. Genesis points are plotted only if the amplitude of the corresponding MJO is greater than 1.

Table 1 quantifies the findings in figure 7. Shown are the phase, the number of days in each phase from May 15-Nov 30 for the East Pacific (column 2) and July-Oct 31 for the Atlantic (column 5), the number of cyclones formed in each phase out of a total of 463 (388) for the East Pacific (Atlantic) basin, and the fraction of TC genesis to total cyclones per RMM phase per basin.

Table 1: Shown are phase of the MJO of amplitude > 1, number of days in each phase for May 15 - Nov 30, East Pacific number of storms (≥ 34 kt) formed per phase (463 total storms), East Pacific ratio of storms per phase to total storms, number of days in each phase for July 1 - Oct 31, Atlantic number of storms per phase (388 total storms), and Atlantic ratio of storms per phase to total storms

Phase	Days	East Pacific (463 TCs)	East Pacific Fraction	Days	Atlantic (388 TCs)	Atlantic Fraction
1	662	66	1/7	427	32	1/11
2	590	42	1/11	375	42	1/8
3	374	17	1/27	201	22	1/16
4	440	19	1/25	247	22	1/16
5	612	27	1/17	424	24	1/14
6	519	28	1/17	293	22	1/16
7	392	31	1/15	195	11	1/28
8	453	33	1/14	222	15	1/22

In agreement with Pegion et al. (2008), most cyclones over the East Pacific tend to form during RMM phases one, two, and eight, while cyclone genesis is less likely during phases three, four, five, and six. For the East Pacific, cyclogenesis is more likely when convection is suppressed over the East Indian Ocean and Maritime continent (Maloney and Hartmann, 2000a). This occurs approximately around phases 8 and 1 of the RMM MJO index. In contrast, cyclones are less likely to occur when convection is enhanced over the East Indian Ocean and Maritime continent. This is observed during RMM MJO index phase 4. Approximately 4 times more cyclones were observed in

phase 1 than phases 3 and 4. Normalized to the number of days in each phase (done by taking storms formed per phase and dividing by total number of days in each phase), approximately twice as many storms form during phases 8 and 1 than during phases 3 and 4.

Over the Atlantic basin, most tropical cyclones initiate genesis during phases 1 and 2 of the MJO, as noted by Klotzbach (2010). Cyclogenesis is least frequent during phase 7. Normalized to the number of days in each phase, approximately 1/3 more cyclones form during phases 1 and 2 than phases 6 and 7. In the Gulf and Northwest Caribbean regions alone, we find that approximately 4 times more cyclones are observed during phases 1 and 2 than phases 6 and 7. While this relationship in the Gulf and Caribbean has been previously studied (Maloney and Hartmann, 2000b; Klotzbach, 2010), the Atlantic model developed in this study focuses on the full Atlantic basin. This is because in logistic regression (and various other statistical techniques), the probability of rare events are highly underestimated (King and Zeng, 2001). In terms of a weekly occurrence, it is relative rare to observe a cyclogenesis event in the Gulf and Western Caribbean.

Univariate logistic regression models are fitted individually for each RMM index to confirm the choice of model, shown in figures 8-11. The same binning process as climatology is applied to both indices for each basin. Both indices are lagged out to a 7 week lead and models are fitted for each lead. Although week 0 has no predictability, it is shown for comparison.

Figure 8 indicates a strong relationship between RMM1 and East Pacific TC genesis out to a week 3 lead based on the steepness of the curve and the goodness of fit

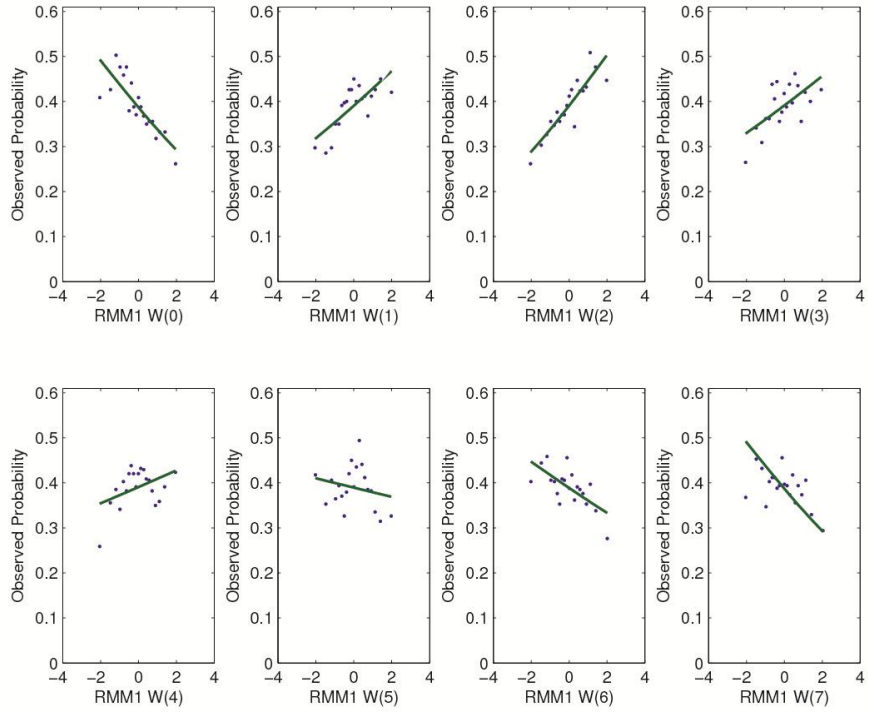


Fig 8: East Pacific genesis observations binned according to RMM1 value and averaged (dots) out to a week 7 lead. W(0) denotes a week 0 lag. Logistic regression models (solid curve) are calculated independently.

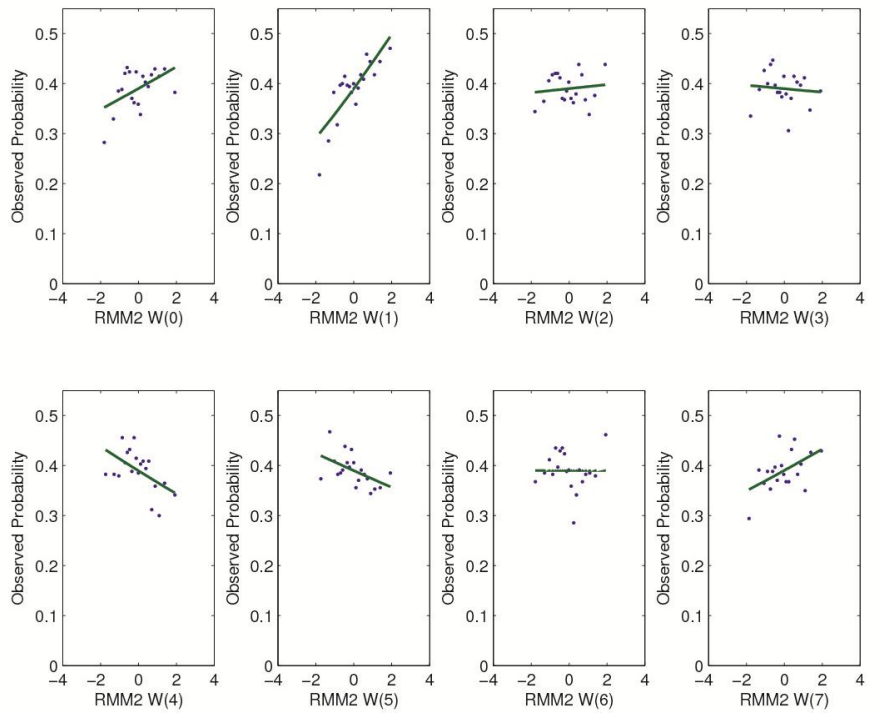


Fig 9: Same as fig. 8 but for RMM2.

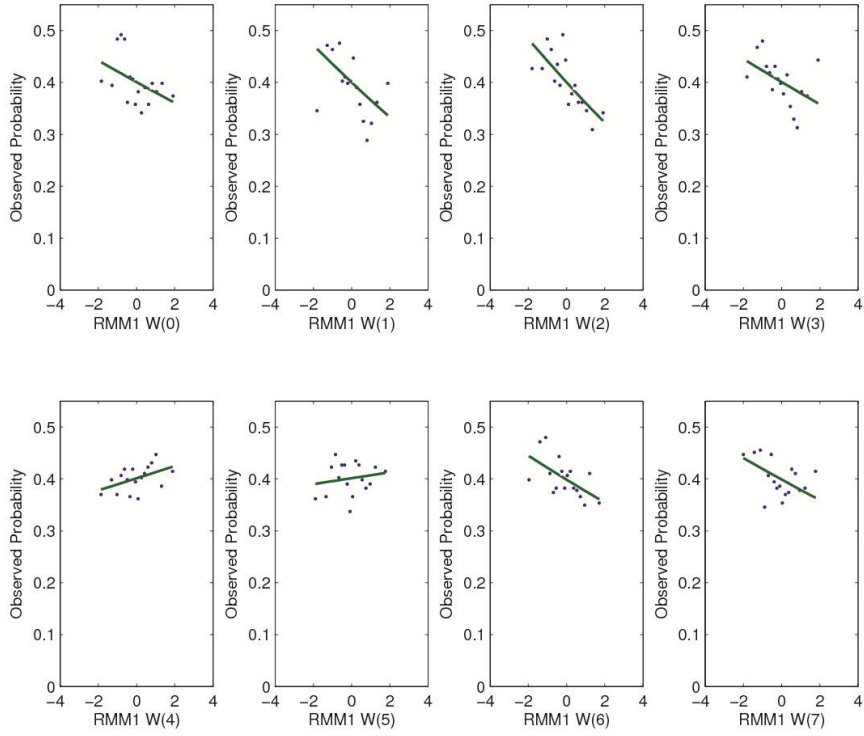


Fig 10: Same as fig. 8 but for the Atlantic basin.

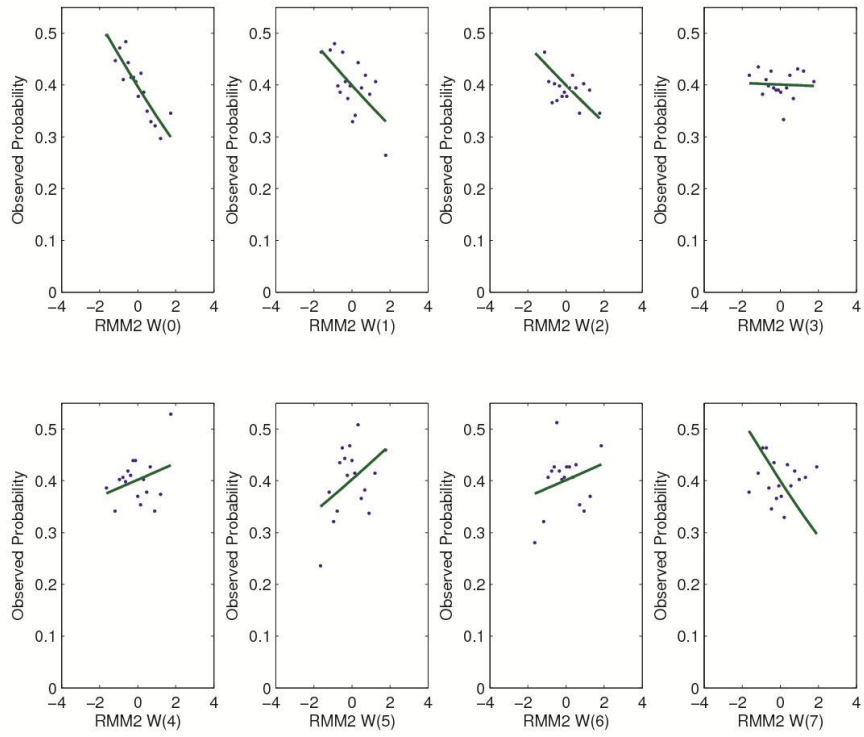


Fig 11: Same as fig. 9 but for the Atlantic basin.

about the curve (shown in table 2). For RMM2 the relationship weakens after a week 1 lead, the strongest being at a week 1 lead. For the Atlantic basin it is expected that the MJO signal would be weaker than for the East Pacific due to its greater distance from the origin of MJO events and weaker dynamical MJO signals. The relationship between the MJO and Atlantic genesis appears to diminish by week 3.

3.1.3 ENSO and PC2 of Equatorial East Pacific SST

Probability curves are generated to show the relationship between the El Niño index (PC1) and TC genesis in both basins. Warm (cold) events are defined when the El Niño index is greater (less) than 1 (-1). Neutral ENSO events are defined when PC1 lies between -1 and 1. Weekly probabilities of cyclone genesis are calculated per event and smoothed using a 1-2-1 filter. Probabilities are denoted as a percentage and shown in figures 12 and 13. The probability of cyclogenesis during warm events, cold events, and neutral events are shown in red, blue, and black, respectively.

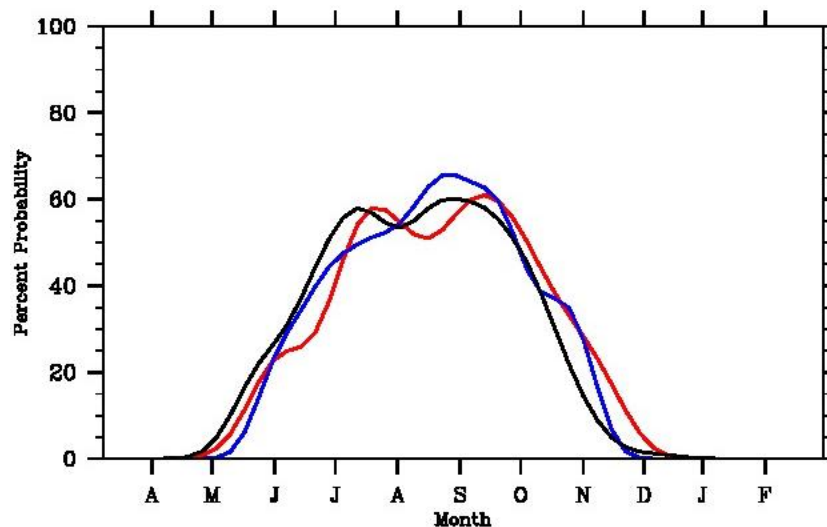


Fig 12: East Pacific TC genesis probability curves based on an El Niño index. Warm events occur when $PC1 > 1$ (red curve) and cold events occur when $PC1 < -1$ (blue curve). Values between -1 and 1 denote neutral ENSO conditions (black curve). The x-axis ranges from March-February.

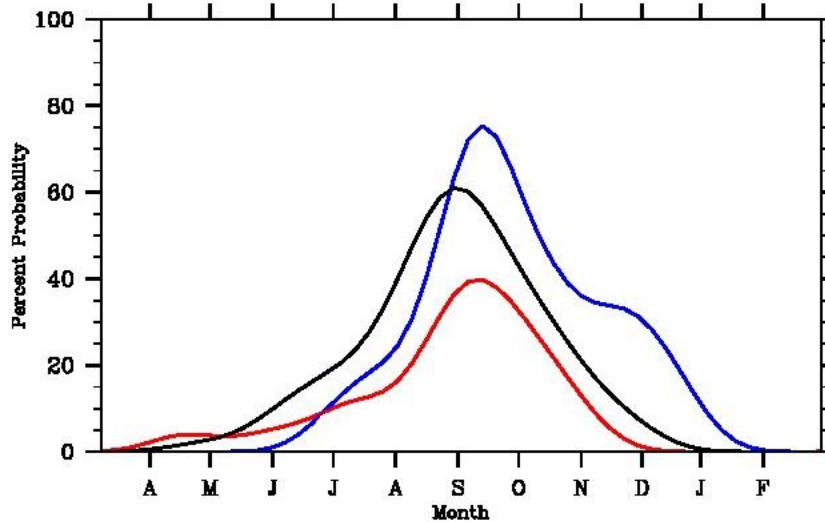


Fig 13: Same as fig. 12 but for the Atlantic.

Higher probabilities in figures 12 and 13 signify that a higher number of tropical cyclone genesis formations were observed from 1975-2009 within a given phase of ENSO relative to the other phases. A relationship between East Pacific TC genesis and the state of ENSO is not evident in figure 12. There does not appear to be a distinctive difference between the probabilities of a storm forming during a certain state of ENSO, therefore ENSO may not be useful as a predictor. This is consistent with the discussion in the introduction. For the Atlantic case, warm ENSO events are associated with a reduction in TC activity (Gray, 1984a; Shaman et al., 2009). Figure 13 demonstrates this relationship and supports the use of ENSO as a predictor in the finalized model.

Univariate logistic regression models are generated in the same method as the RMM indices and shown in figures 14-17. While figure 14 suggests a relationship with TC genesis and ENSO in the logistic regression curve, the goodness of fit between the logistic curves and the probability averages do not depict a definite relationship (table 2). ENSO is kept as a predictor in the finalized East Pacific model due to its previously studied relationship with genesis location and storm frequency at higher intensities (Chu,

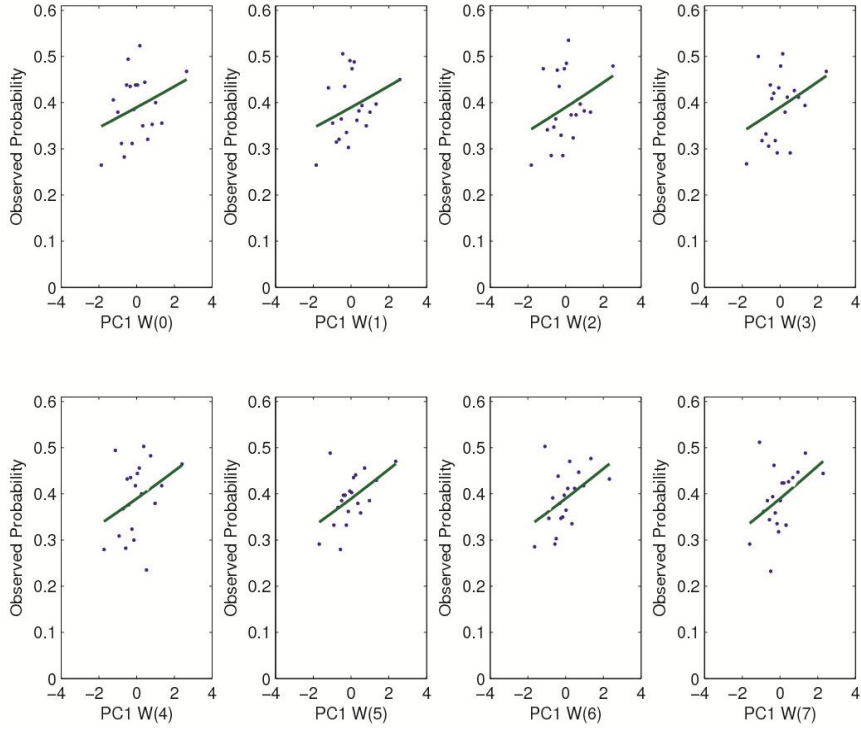


Fig 14: East Pacific genesis binned according to PC1 (El Niño index) and averaged (dots) out to a week 7 lead. Solid curve - Logistic regression models

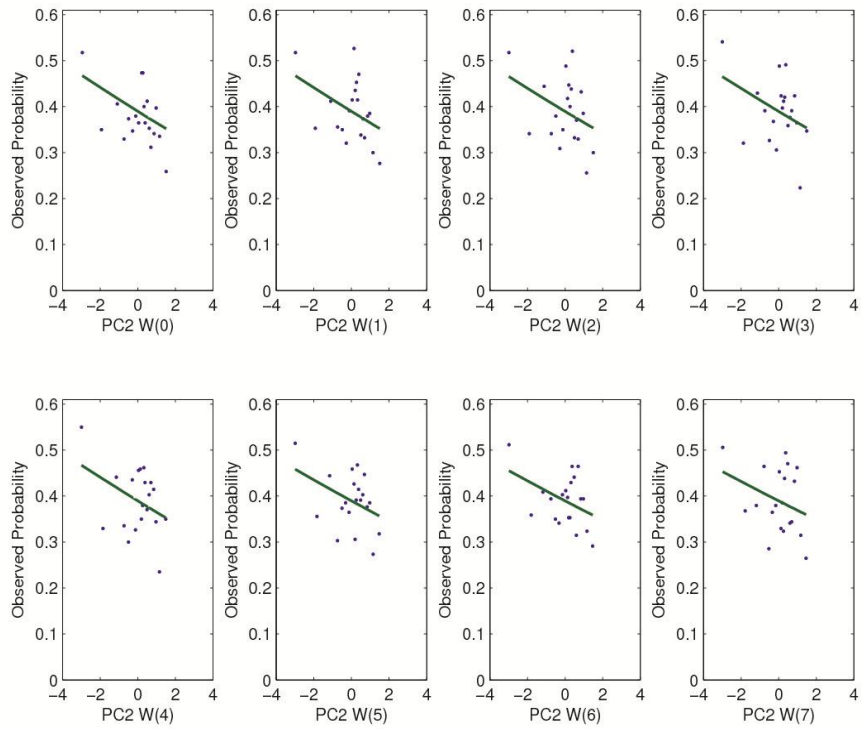


Fig 15: Same as fig. 14 but for PC2

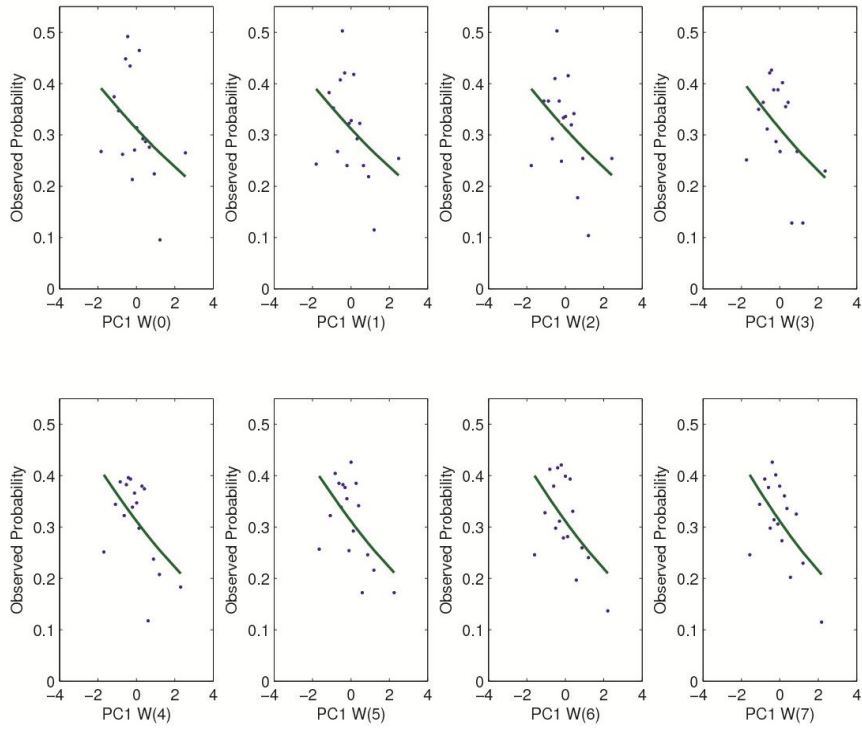


Fig 16: Same as fig. 14 but for the Atlantic

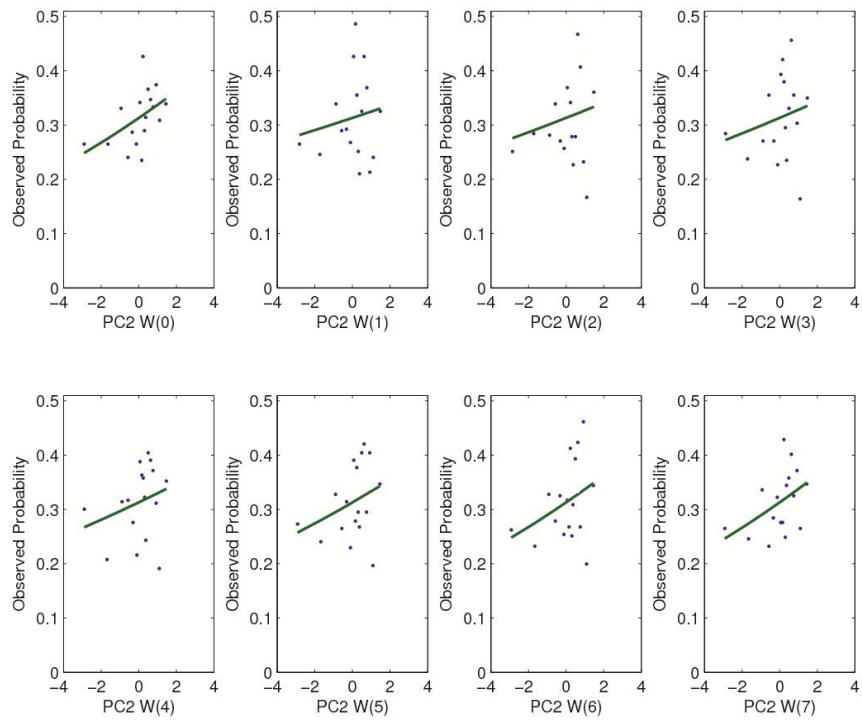


Fig 17: Same as fig. 16 but for PC2

2004; Gray and Sheaffer, 1991; Whitney and Hobgood, 1997). Model results using only storms which become hurricanes are later discussed, and ENSO may become an important factor for those. If ENSO does not benefit the finalized model, the forward selection scheme discussed previously will not select it; therefore having it in the model will not adversely affect the results.

Despite a relatively high degree of scatter, figure 16 shows logistic regression captures the suppression of TC genesis during El Niño events for the Atlantic. Based on previous studies of ENSO's effects on genesis and the results shown by figure 13, the use of ENSO as a predictor for the Atlantic is supported. The second PC over the El Niño 3 region is also investigated; however, there does not appear to be a relationship between PC2 and genesis in either basin. Based on this and lack of physical reasoning, PC2 is not included in the model.

3.1.4 Goodness of Fit

Sections 3.1.1 through 3.1.3 describe univariate logistic regression models developed to check the relationship between the predictors investigated and tropical cyclogenesis, as well as the fit between the predictors and logistic regression. Correlations are calculated between the binned predictor probabilities and the logistic regression curves as a measure of the goodness of fit about the regression curves. While correlations are typically used in linear regression schemes, the relationships shown are largely linear. Other verification methods, however, are used for the finalized model (section 5). The correlation values are shown in table 2. A p-value of each correlation is computed using $N-2$ degrees of freedom to measure the significance of the correlation, where N is the number of samples (in this case the number of bins).

Table 2: Correlations between binned averages of the predictor values and the corresponding logistic fit per forecast lead for each basin. Since the same climatology is used at all forecast leads, only one correlation is calculated for climatology.

Basin	Week Lead	Clim	PC1	PC2	RMM1	RMM2
East Pacific	0	0.97	0.31	0.34	0.82	0.49
	1		0.32	0.40	0.75	0.81
	2		0.33	0.36	0.89	0.12
	3		0.35	0.37	0.63	0.10
	4		0.34	0.38	0.43	0.53
	5		0.51	0.39	0.22	0.51
	6		0.45	0.41	0.68	0.0004
	7		0.44	0.31	0.50	0.50
Atlantic	0	0.97	0.46	0.32	0.44	0.90
	1		0.53	0.08	0.50	0.64
	2		0.51	0.06	0.74	0.62
	3		0.49	0.08	0.48	0.05
	4		0.49	0.11	0.47	0.32
	5		0.51	0.14	0.18	0.43
	6		0.55	0.17	0.59	0.26
	7		0.53	0.22	0.41	-0.01

As observed in figure 6, the climatology binned averages appear to fit the logistic regression curve well, corresponding to a correlation of 0.97 between the averages and the logistic fit for both basins, which is significant at the 99% level, signifying a 1% chance the correlation is not actually significant. For the East Pacific, PC1 p-values are significant for weeks 5 and 6 at the 95% significance level, meaning there is a 1 in 20 chance (i.e., 5% chance) that the correlation is not actually significant. For the PC2 logistic curve and binned averages, there are no significant correlations at the 95% level. RMM1 correlations are significant for week leads 0, 1, 2, 3, and 6 at the 99% level, while week 7 is significant at the 95% level. For RMM2, a 99% level significance exists at week 1, while a 95% level significance occurs for weeks 0, 4, 5, and 7.

For the Atlantic basin, p-values of PC1 are 95% significant for all week leads with the exception of week 0, while no significant correlations are observed between the PC2 binned averages and logistic curve. P-values of RMM1 are significant at the 95% level during week leads 1, 3, 5, and 6; the week 2 p-value is significant at the 99% level.

For RMM2, p-values for weeks 0, 1, and 2 are significant at the 99% level. A significant correlation is not analogous to a useful regression; a high correlation can exist between two variables which have a relative horizontal regression curve (i.e., a low regression coefficient). Correlation is only a measure of the goodness of fit about the regression.

3.2 Predictor Selection

An advantage of using a forward selection scheme is that it ranks the selected predictors by level of “importance” based on a significance criterion (Hosmer and Lemeshow, 2000). This provides information on which predictors have the greatest statistical influence on tropical cyclogenesis in each basin for each lead. Using the full data set, table 3 lists the ranks given by the forward selection scheme for each basin at every lead. A box is left blank if the predictor is not selected.

Table 3: Predictor selection rank according to the forward selection scheme for each basin from a zero to a seven week forecast lead. Data from 1975-2009 is used. A “1” designates the first predictor chosen by the selection scheme, and so on. Spaces left blank indicate the predictor did not meet the criteria and therefore was not chosen.

Basin	Week Lead	Clim	ENSO	RMM1	RMM2
East Pacific	0	1	4	2	3
	1	1	4	3	2
	2	1	3	2	
	3	1	3	2	
	4	1	2	3	4
	5	1	2		
	6	1	2		
Atlantic	0	1	2	4	3
	1	1	2	3	4
	2	1	2	3	4
	3	1	2	3	
	4	1	2		
	5	1	2		3
	6	1	2	3	4
	7	1	2		

Climatology is the first chosen predictor for both basins at every lead, meaning it accounts for the most variability in the tropical cyclone observations. Not surprisingly,

ENSO was chosen second for all forecast leads in the Atlantic basin. Interestingly, ENSO was always chosen as a predictor in the East Pacific basin. Although always chosen last with the exception of week 4, it shows ENSO may have some statistically significant influence, although minor, in East Pacific cyclogenesis. One of the MJO indices was typically chosen as the second predictor for the East Pacific out to week 4. The selection between RMM1 and RMM2 for both basins agrees with the univariate curves shown in figures 8-11; the selection scheme tends to choose first the RMM index with the steepest curve, or not at all if there appears to be no relationship (has a “flat” logistic curve). It also “catches” and excludes those predictors which appear to have a relationship in the univariate logistic regression curves but have no significant relationship when comparing to the TC observations, such as the univariate RMM2 week 7 model for the Atlantic basin (fig. 11), which is also shown to have an almost-zero correlation with the logistic curve (correlation of -0.01; see table 2).

4. Hindcasts

4.1 Probability Hindcasts

Probability hindcasts are generated for each year and forecast lead in this study as a form of cross-validating the model. Although week 0 provides no predictability, it is shown as a means of comparison. Regression coefficients utilizing data from the full dataset, excluding the hindcasted year, are found and applied to equation 2.1. These coefficients represent the relationship between TC genesis and the predictors. The probability that a cyclone will form, based on the hindcasted year's predictor values, is found for tropical cyclones reaching at least tropical storm strength.

Tropical storm strength cyclogenesis probability curves are hindcasted and four examples per ocean basin are shown in figures 18-25. Results from all years are shown in Appendix I (East Pacific) and Appendix II (Atlantic). The hindcasted probability curves generated by the logistic regression model using a forward selection scheme are shown by the black curve. An independent logistic regression model and forward selection scheme is used per forecast lead, so a predictor may be chosen at a certain week lead and not another. Overlaid in red is the climatology of each basin from figure 3 for comparison. This is useful as it allows the probability curves to show a difference from the known climatology due to the predictors chosen by the selection scheme. The gray

bars along the x-axis represent a week which underwent cyclogenesis. Due to the overlapping weeks previously defined, each gray bar is at least one week long.

4.1.1 East Pacific Hindcasts

The East Pacific hindcasts range from May 15 (shown as M15 in the x-axis) to November 30. The RMM indices provide the short term variability, in the order of days to a week, in the probability hindcasts. ENSO, on the other hand, is slow varying on the order of months; it has the tendency to shift most of the full season hindcast curve. When the hindcasted probability has the shape of climatology (with either a different or the same amplitude), there is no small order variability, meaning neither RMM index was selected. East Pacific hindcast probability curves are shown for years 2001, 2002, 2007, and 2008 in figures 18-21.

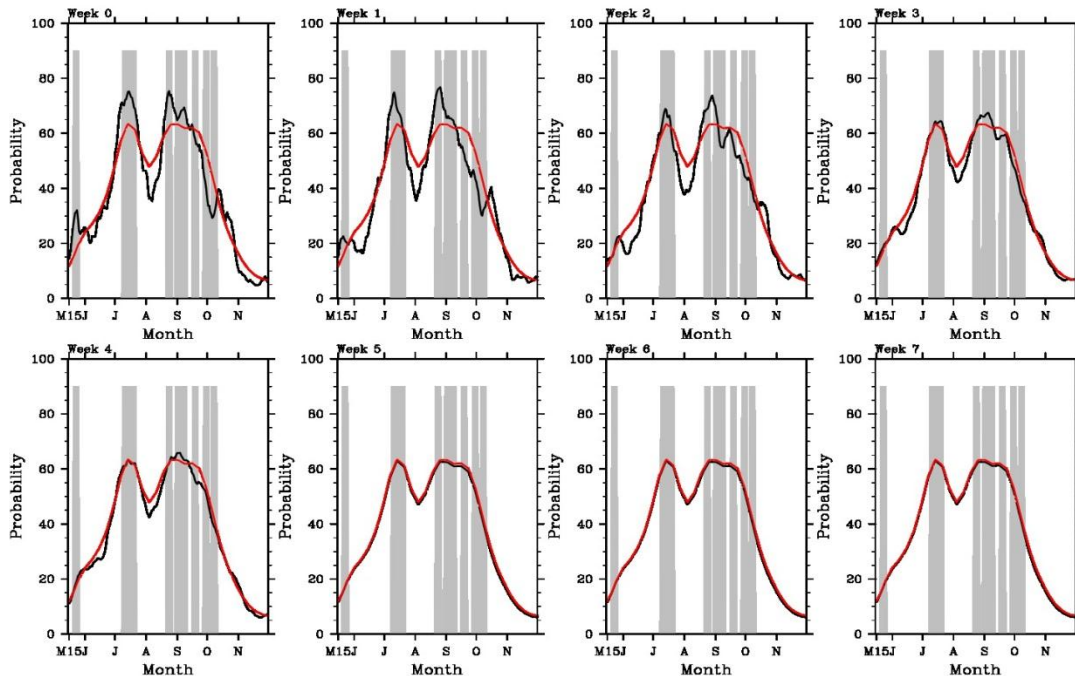


Fig 18: East Pacific 2001 probability hindcast (black curve) for a week 0 (top left) to a week 7 (bottom right) lead. Climatology is shown in red for comparison. Gray bars are shown for weeks that underwent tropical storm (≥ 34 kt) cyclogenesis. The x-axis ranges from May 15 - Nov 30.

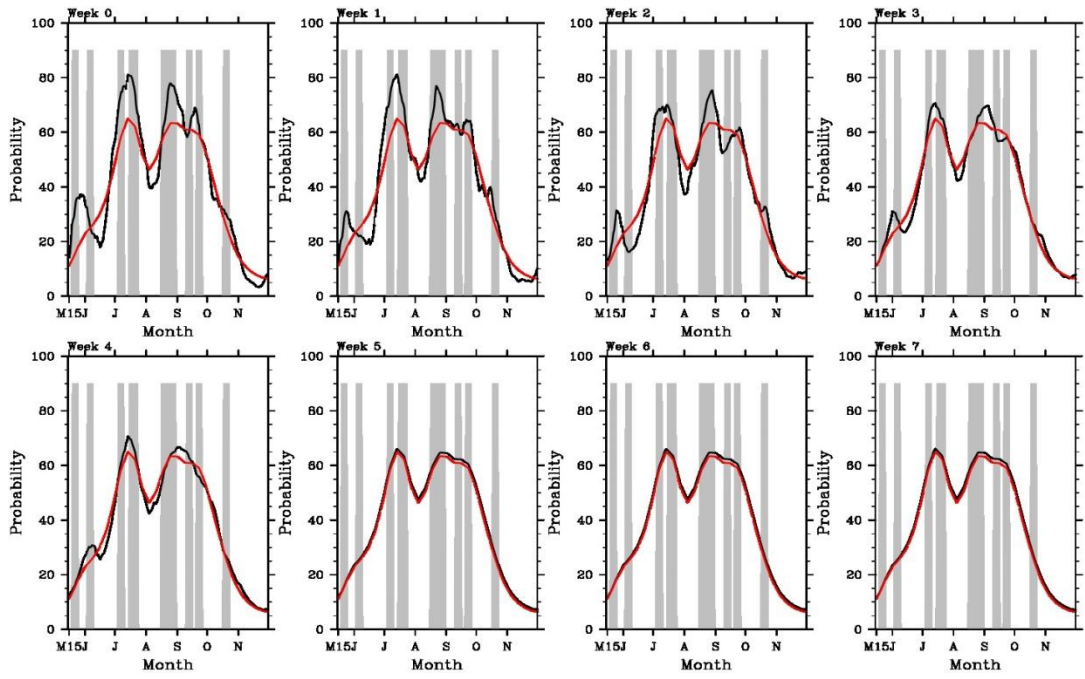


Fig 19: Same as fig. 18 but for 2002

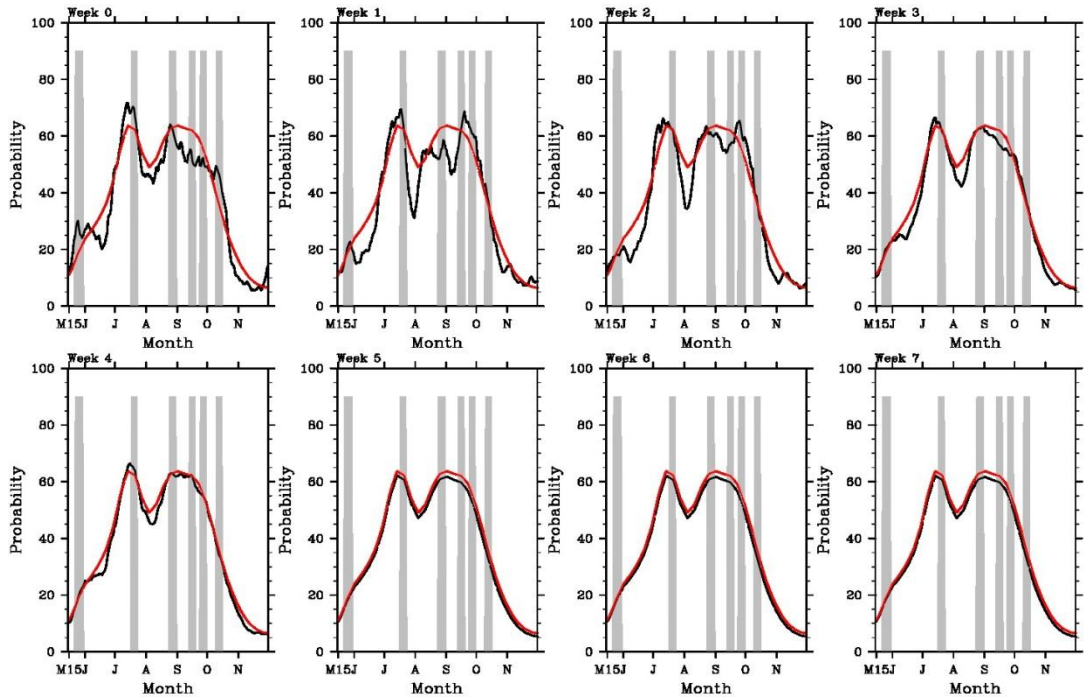


Fig 20: Same as fig. 18 but for 2007

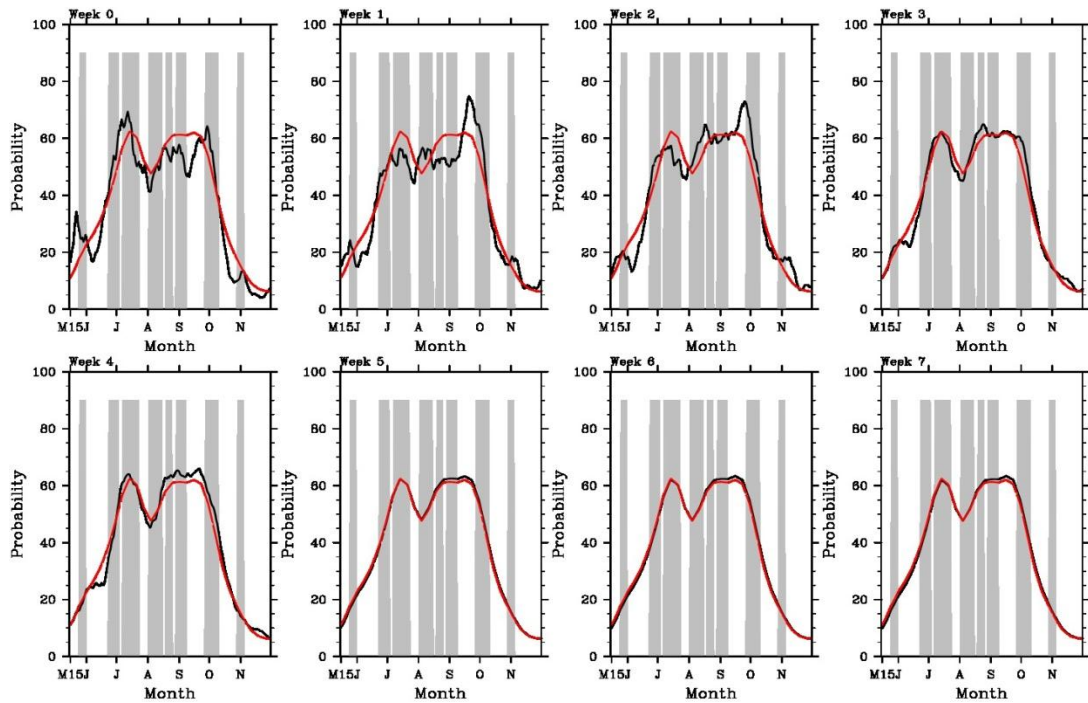


Fig 21: Same as fig. 18 but for 2008

The 2001 and 2008 East Pacific hurricane seasons are characterized by MJO amplitudes typically greater than 1 and neutral ENSO conditions. In the 2001 hindcast probabilities increase above climatology by as much as ~15% due to the MJO; this peak in mid-July coincides with an observed cyclogenesis event (gray bars; a more quantitative measure of skill is later discussed). At a week 1 forecasting lead, the probabilities peak at the end of phase 6 and beginning of phase 7, consistent with the RMM univariate curves (fig. 8-9; see Wheeler and Hendon (2004) for phase definition based on the RMM values). The favorable conditions for genesis during phase 8 are represented in the peaks at the week 0 lead. This is common in the hindcasted years; once the end of phase 6 and the beginning of phase 7 occurs, climatologically the following week phase 8 will commence, so the week 1 forecast lead shows an increase in cyclogenesis probability.

The 2002 season consisted of strong MJO variability from the beginning of the season through August (with the exception of the last week of July) then again in

November, along with moderate El Niño conditions. Most of the variability in the probability hindcasts occurs during the high amplitude MJO variability. The week 1 forecast lead shows a probability increase of ~20% in mid-July, escalating the probability of cyclogenesis to almost 80%; again as the MJO approaches phase 8. Observations (gray bars) tend to coincide with high peaks in probability. The moderate El Niño had little effect on the probability curves, only slightly increasing probabilities.

The 2007 season consisted of an early season neutral ENSO followed by a moderate La Niña and MJO amplitudes that varied from weak to strong. The week 1 and week 2 forecast leads show a deep decrease from climatology by ~20% (week 1 lead) and ~15% (week 2 lead) during the midsummer drought (Magaña et al., 1999). This drop in genesis probability is associated with the oncoming phase 3 during a strong MJO event; the week 1 lead shows this at phase 2 while the week 2 lead at phase 1; no cyclogenesis events occur during this probability minimum. The moderate La Niña shows little consequence, only slightly decreasing mid to late season genesis probabilities. East Pacific hindcast results from other years are shown in Appendix I.

4.1.2 Atlantic Hindcasts

Probability hindcasts shown for the North Atlantic basin include 1975, 1997, 2003, and 2007 in figures 22-25. The Atlantic hindcasts range from July 1 to October 31. A moderate La Niña event in 1975 caused a 5-10% increase in genesis probabilities throughout the season. MJO activity is responsible for the shorter time scale variability in probabilities, increasing mid-late July probabilities by an additional 7% during forecast

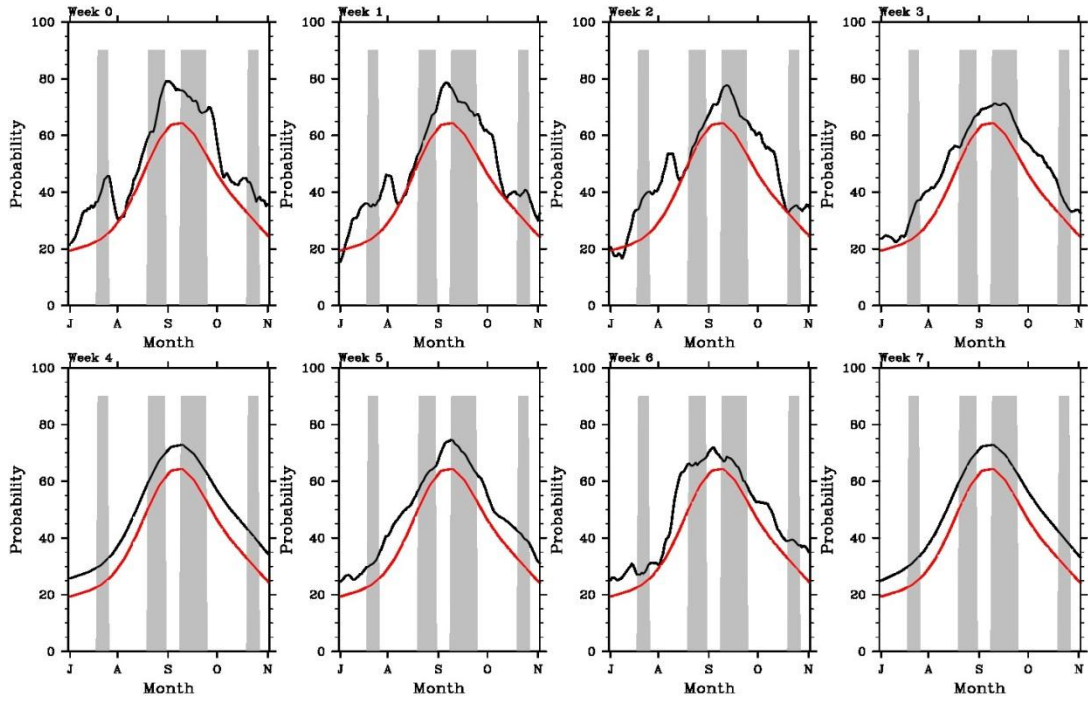


Fig 22: Atlantic 1975 Probability hindcast (black curve) for a week 0 (top left) to a week 7 (bottom right) lead. Climatology is shown in red for comparison. Gray bars are shown for weeks that underwent tropical storm cyclogenesis. The x-axis ranges from July 1- Oct 31.

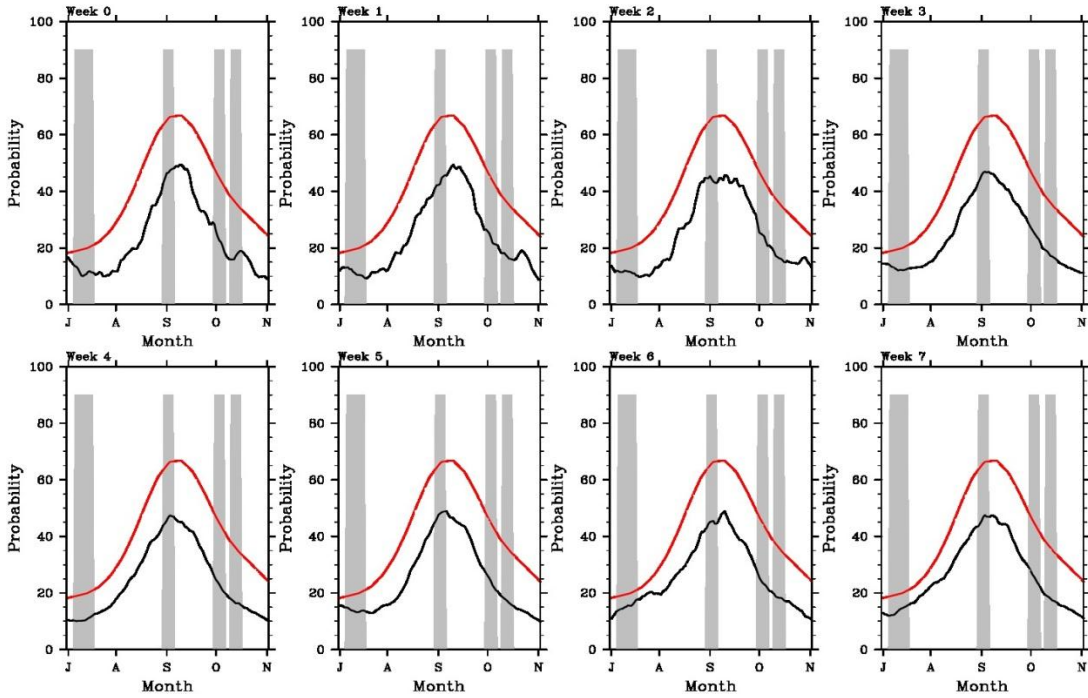


Fig 23: Same as fig. 22 but for 1997

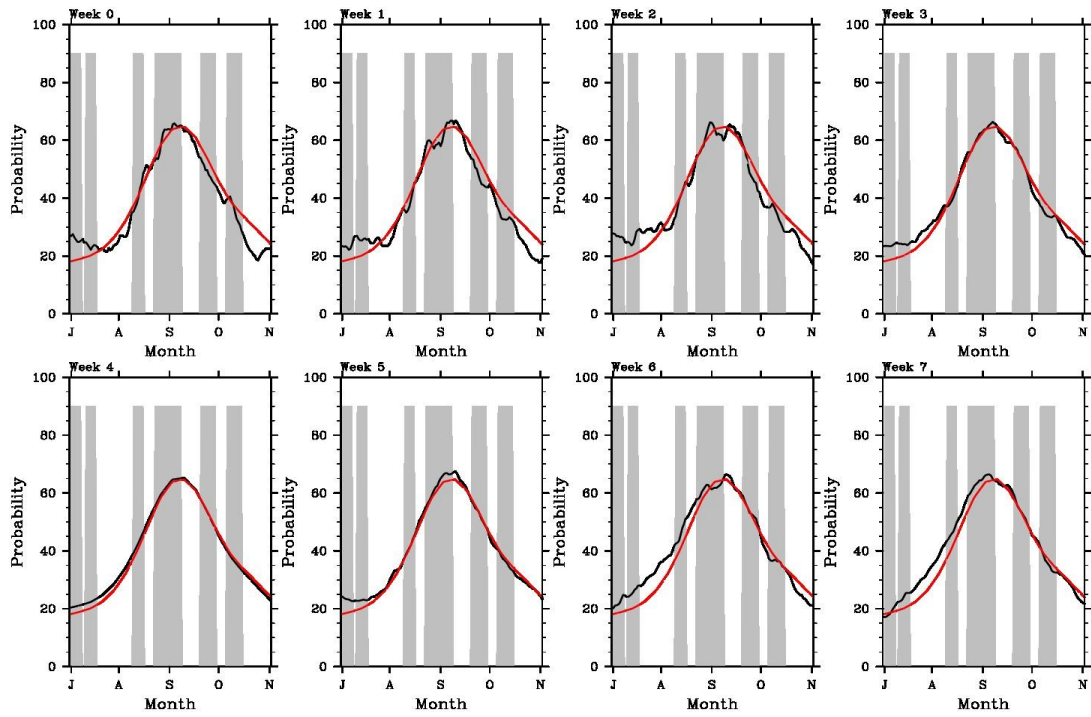


Fig 24: Same as fig. 22 but for 2003

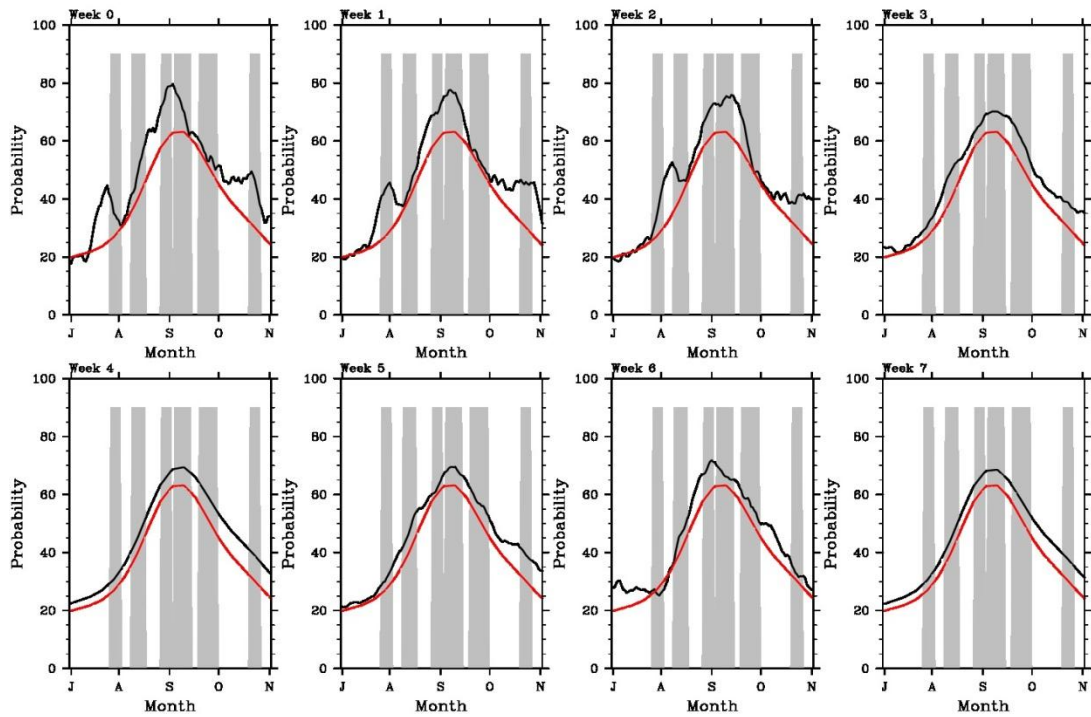


Fig 25: Same as fig. 22 but for 2007

lead weeks 1 and 2. This increase is associated with phase 2 of the MJO, known to create favorable conditions for cyclogenesis as previously discussed. Also observed in the 1975 season are probability increases in the month of September and in late October corresponding to phases 1 and 2 of the MJO. Furthermore, decreases of 5-7% are observed due to the MJO early-mid August and early-mid October.

A strong El Niño in 1997 decreased cyclogenesis probabilities at every forecast lead by as much as 20%. In agreement with this overall drop in climatology, the 1997 hurricane season was below average in terms of TC activity (Rappaport, 1997). This suppression of cyclogenesis due to an El Niño event is also consistent with figures 13 and 16. Although some modest variations in probabilities were due to the MJO, the hindcast is primarily influenced by the strong El Niño.

The ENSO-neutral 2003 season is primarily interesting due to the month of July. A moderate MJO event early-mid July created favorable conditions for tropical cyclogenesis. This is depicted as a cyclogenesis probability increase in forecast leads 1, 2, 3, and interestingly (perhaps coincidentally) week 5. This increase ranges between 5-10%, with the greatest increase observed at a week 2 lead, and coincides with the observed formation of 2 hurricanes. Additionally, a decrease of ~7% at lead weeks 1 and 2 is notable in late October due to the suppression of cyclogenesis that occurs during phase 6 of the MJO. Very little change in genesis probability occurred due to ENSO.

The last hindcast year shown is 2007, an above-average hurricane season with 15 tropical storms and 6 hurricane strength storms. The mid-late season La Niña increases probabilities by ~7% in late October. Most of the variability in the hindcasts, however, is due to the MJO. The late July and early August peak and the late August and early

September peak in probabilities are prominent in lead weeks 1 and 2 and are associated with phase 2 of the MJO; the latter peak coincides with the formation of Hurricane Felix, a category 5 hurricane (this does not signify causality, it means that conditions were more favorable for genesis). The late October probability increase is a result of the La Niña, increasing probabilities by approximately 7%, and MJO phase 1 conditions increasing probabilities by an additional 10%. In correspondence with the probability increase is the formation of a hurricane strength storm. Atlantic hindcast results from other years are shown in Appendix II.

5. Model Skill and Reliability

5.1 Brier Skill Scores

Qualitatively it can be observed from the hindcasts if an increase or decrease in probability corresponds to a cyclogenesis event (gray bars) or lack thereof. In order to assess the validity of the hindcasts, a quantitative statistical approach is used. A Brier score using all hindcasted values and corresponding observational values of TCs is generated per basin and forecast lead by equation 2.8. A logistic regression model using only a seasonal mean climatology is used to generate reference hindcasted probabilities; hence the same value is predicted for every day representing the seasonal average probability of cyclogenesis within that basin. These reference probabilities are then used to calculate the reference Brier score in equation 2.9.

Four separate sets of Brier scores are calculated per basin per week lead and plotted in figure 26. The black dash curve denotes the Brier skill scores for the hindcast probabilities generated with all available predictors using the selection scheme. Individual hindcast probabilities are calculated using only a set of predictors: MJO + climatology only, ENSO + climatology only, and climatology only. The Brier skill scores for these hindcasts are plotted in dashed blue, dashed green, and solid red, respectively. A comparison can then be made to represent the relative importance of the predictors and the skill improvement when compared to a mean seasonal climatology.

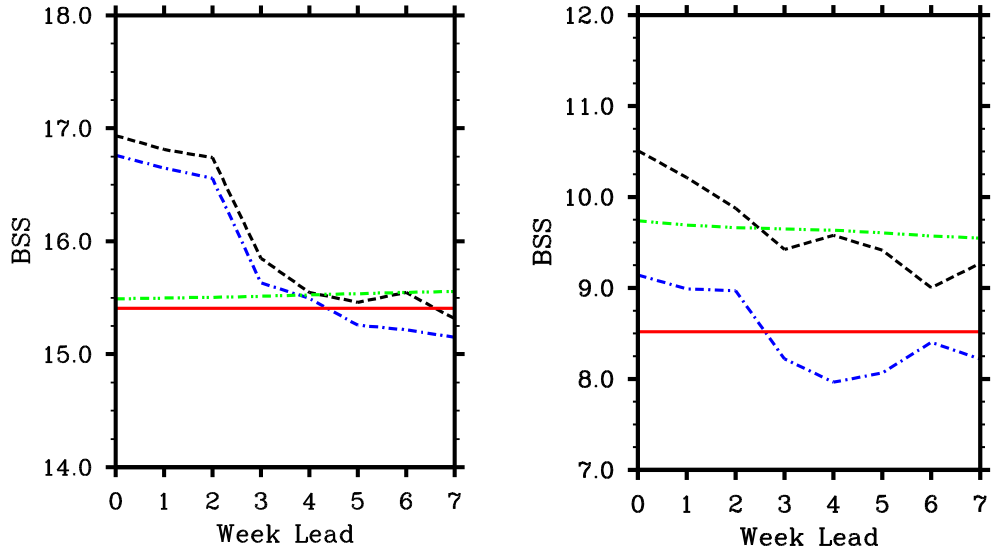


Fig 26: Brier skill scores (%) for the East Pacific (left) and Atlantic (right) tropical storm probability hindcasts. Shown are Brier skill scores for the stepwise scheme selected predictors (dashed black), MJO + climatology (dashed blue), ENSO + climatology (dashed green), and climatology only (solid red). Skill scores are calculated using a seasonal mean reference climatology; y-axis denotes % improvement over the reference climatology.

The East Pacific climatology Brier skill score alone shows over a 15% improvement over using a mean seasonal climatology. The skill does not change over lead week since climatology is always known and is therefore the same for each forecast week. Not surprisingly, including ENSO as a predictor adds only an additional small fraction of a percent improvement without much change over week lead. Including the MJO to climatology improves the skill by almost an additional 1.5% during weeks 1-2, with further slight improvement given the predictor selection scheme; these tend to decrease towards the climatology model skill over longer forecast leads. Overall, including all selected predictors improves the skill of the model by almost 17% at the shortest leads. These results are similar to those of Leroy and Wheeler (2008) for the Southern Hemisphere; in their study they found Brier skill score improvements of up to

9.5% from a mean seasonal climatology due to the inclusion of the seasonal cycle of TCs, the MJO, and the leading modes of SST. The Brier skill score values found in this study are of a similar magnitude as those in Leroy and Wheeler (2008).

The Atlantic climatology Brier skill score shows an improvement of approximately 8.5% over the model using a mean seasonal climatology. The addition of the MJO to climatology shows a skill increase out to forecast lead week 2 of around 0.5%. The Brier skill score of the model using ENSO + climatology generates an improvement greater than 1% over climatology alone, decreasing only slightly at the longest lead times. Including all selected predictors, there is a skill improvement of almost 2% over the model using only climatology, this skill generally decreasing over forecast lead. Overall, the model of the selected predictors improves the skill of the model by almost 10.5% at the shortest leads.

5.2 Reliability Diagrams

Testing the reliability of a model is commonly done via reliability diagrams. This is done by binning the dichotomous genesis observations and the hindcasted probabilities according to the hindcasted probability. For the East Pacific, observations and hindcasted probabilities are binned into 20 groups of approximately 340 values each. For the Atlantic the bins consist of 17 groups of roughly 246 values each. For each group the bins are averaged and plotted to form the reliability curve.

The perfect forecast, shown by the solid black diagonal lines in figures 27 and 28, occurs when the forecasted probability equals the observed probability. A 10% interval about that perfect curve is shown by the blue dotted diagonal lines. When the reliability

curve lies above (below) the perfect diagonal, the forecast is underestimated (overestimated). The mean observed probability is shown by the solid horizontal line.

5.2.1 East Pacific

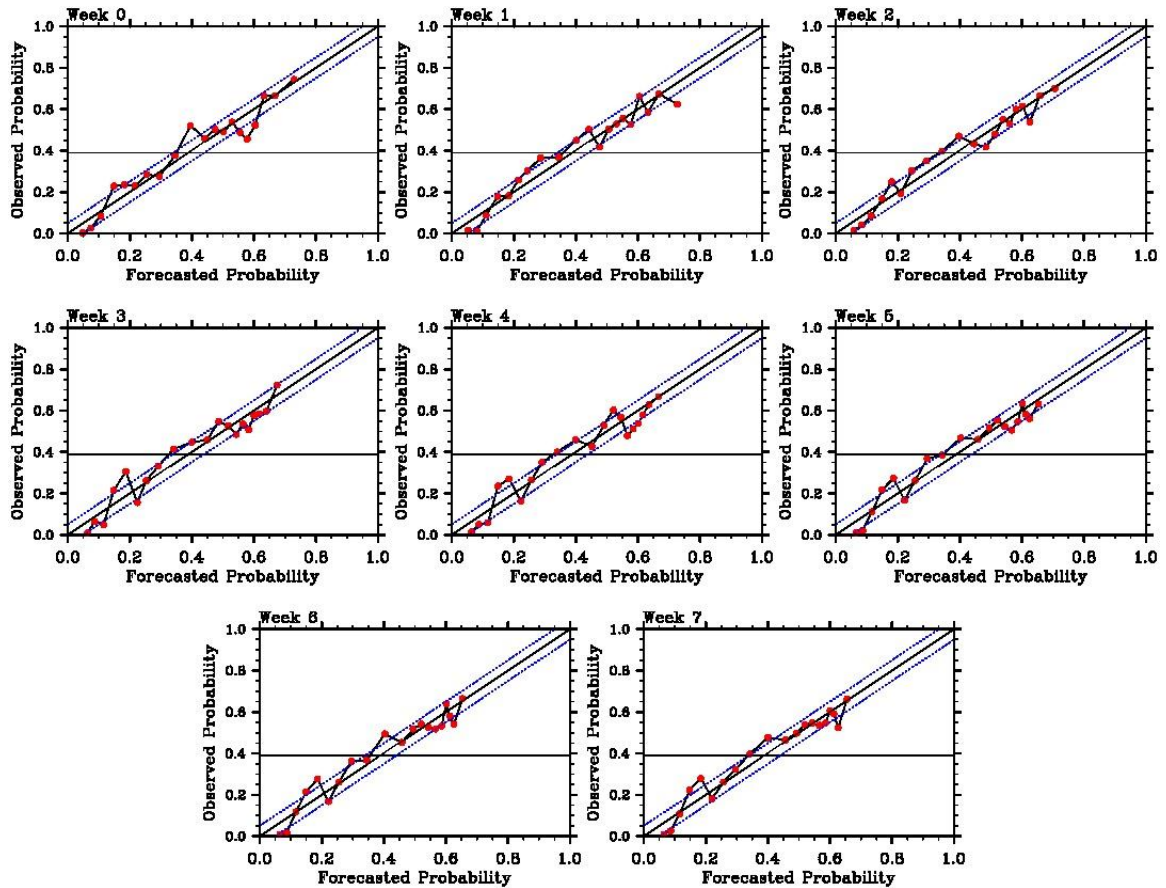


Fig 27: East Pacific reliability diagrams for forecast lead weeks 0 - 7. Observational and hindcasted data used is from 1975-2009. Hindcasts and observations are binned into 20 groups of ~340 values based on the hindcasted probabilities. Each group is averaged and portrayed as a red circle. The line connecting the circles forms the reliability curve. The perfect forecast and a 10% interval about the perfect forecast is shown by the solid black and blue dotted diagonals, respectively. The solid horizontal line indicates the average observed probability.

For every week lead, the East Pacific probability of TC genesis is slightly overestimated by 5% for the first two bins (the two lowest probability groups).

Reliability diagrams generated using the ENSO + climatology hindcasts and the MJO + climatology hindcasts (not shown) also contain this overestimation, suggesting that it is likely due to climatology. Sensitivity tests on the smoothing of climatology found the overestimation is not due to the smoothing; rather, figure 6 suggests the logistic fit causes the overestimation of the lowest probabilities.

A smoothing sensitivity test on the climatology reveals the reason for the overestimation observed between the 0.4 and 0.5 observed probability (y-axis). These errors are due to the smoothing of climatology during the midsummer drought, as illustrated in figure 3. Interestingly, this overestimation is most eminent at lead week 0, which does not represent a prediction; a weaker overestimation is evident in the forecasted values out to forecast lead week 2.

5.2.2 Atlantic

The Atlantic basin reliability curves are shown in figure 28. The use of only July 1 – October 31 is prominent in the Atlantic reliability diagrams, with the first average category (first red circle) near 0.15 probability. Above the mean horizontal line there appears to be less overall deviation from the perfect forecast than the East Pacific. The decrease in deviance is largely due to the greater effects of ENSO on the Atlantic, demonstrated by removing the effects of the MJO from the hindcasted values (not shown). While it is difficult to define causality for each deviation from the perfect forecast, the addition of other indices as predictors may help to account for some of the deviance.

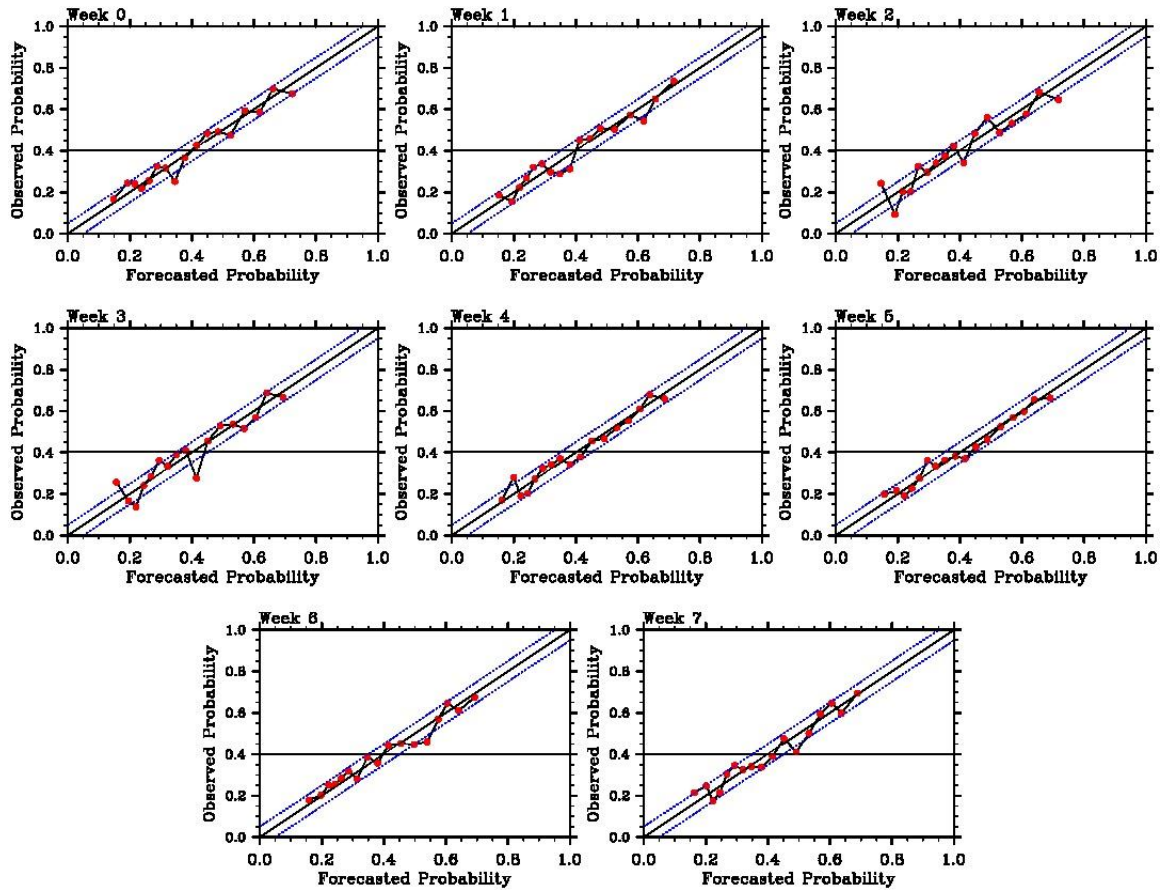


Fig 28: Same as fig. 27 but for the Atlantic. Hindcasts and observations are binned into 17 groups of ~246 values based on the hindcasted probabilities prior to averaging.

5.3 Hurricane Strength Skill

Various studies have analyzed the relationship between hurricane strength storms (≥ 64 kt) and the MJO for the Atlantic (Barrett and Leslie, 2009; Maloney and Hartmann, 2000b; Klotzbach, 2010) and the East Pacific (Chu, 2004; Collins and Mason, 2000). Hindcast probabilities are calculated using cyclogenesis observations of only storms reaching hurricane strength in the same method as the tropical storm hindcasts. Brier skill scores are found as described in section 2.5. A hindcast model of mean seasonal climatology of hurricane strength genesis is used as a reference brier score.

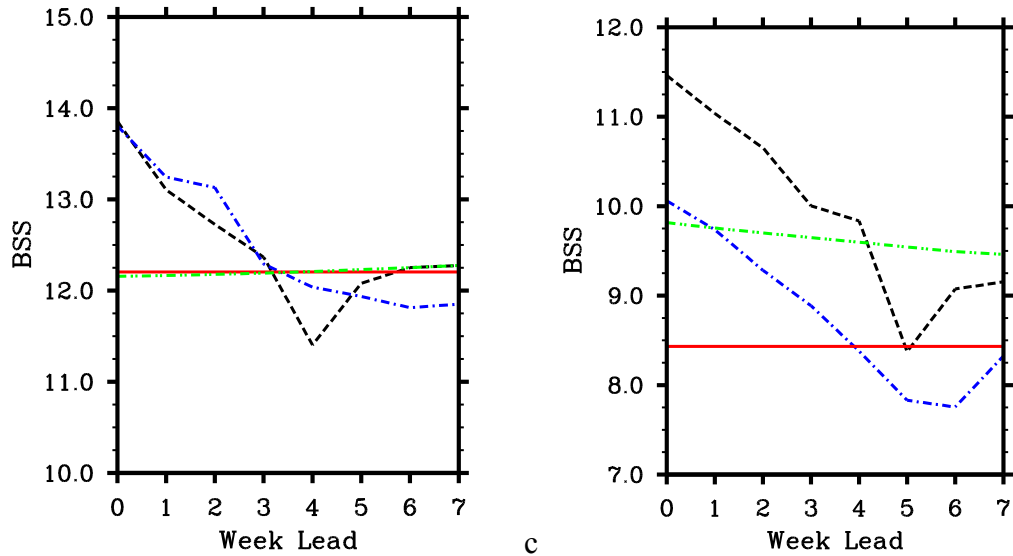


Fig 29: Brier skill scores (%) for the East Pacific (left) and Atlantic (right) hurricane strength probability hindcasts. Shown are Brier scores for the stepwise scheme selected predictors (dashed black), MJO + climatology (dashed blue), ENSO + climatology (dashed green), and climatology (solid red). Calculated using a hurricane seasonal mean reference climatology; y-axis denotes % improvement over the reference climatology.

A primary interest in the inclusion of the ENSO index in the East Pacific model is the predictor's effects given the increase in TC strength. Studies have theorized the influence of ENSO on the East Pacific, noting an increase in intense hurricane frequency during an El Niño event (Gray and Sheaffer, 1991; Whitney and Hobgood, 1997) and genesis location (Irwin and Davis, 1999). Although intense and lesser strength hurricanes are analyzed in unison, figure 29 does not hint any improvement in skill due to the inclusion of ENSO.

A reason for the lack in skill improvement due to ENSO may be due to the separation of the East Pacific basin into subregions, as pointed out by Collins and Mason (2000). Collins and Mason (2000) found that when separating the East Pacific region at 116° longitude, a significant relationship between ENSO and hurricane strength storms is

found only for the western region; the eastern region had no significant relationship with ENSO at the hurricane or intense hurricane level. The East Pacific boundary in this study lies at 120°, and hence the region analyzed is similar to the Collins and Mason (2007) eastern subregion of the East Pacific and therefore it may not be surprising that we see no strong ENSO modulation.

The Atlantic hurricane strength brier scores show an improvement in the MJO predictor skill, expanding the skill of the MJO + climatology model to a week 3 forecast lead. At week 1 the MJO appears as equally skilled as ENSO. The impact of the MJO on hurricane strength storms has been outlined in studies such as Maloney and Hartmann (2000b) and Klotzbach (2010), as discussed in the introduction.

6. Summary and Conclusions

This study proposes an intraseasonal prediction model for tropical cyclone genesis in the East Pacific and Atlantic Ocean basins based on multiple logistic regression. Predictors used include ENSO, the MJO, and a climatology of genesis for each basin. A prediction model for each basin is generated out to a week 7 forecast lead. After undergoing a forward selection scheme process, the predictors selected generate regression coefficients which are used to produce hindcasts for each year from 1975-2009.

Brier skill scores and reliability diagrams were generated to determine the skill and dependability of the models. Results show a significant increase in model skill at predicting tropical cyclogenesis by the inclusion of the MJO out to a three week forecast lead for the East Pacific and a two week forecast lead for the Atlantic. When only considering storms that reach hurricane strength, the inclusion of the MJO in the Atlantic models show further increase in skill out to a 3 week forecast lead, with similar skill improvements above a time-varying climatology as ENSO for a week 1 forecast lead. Including ENSO increased the skill of the tropical storm Atlantic model significantly out to a 7 week forecast lead, while only slightly improving the skill of the East Pacific model. The model generated by the forward selection scheme showed improvements above a mean seasonal climatology of almost 17% for the East Pacific and 10.5% for the Atlantic.

The results found in this study are similar to those in the Southern Hemisphere statistical model of Leroy and Wheeler (2008). The primary differences between the models depend on the strength of the predictor for each basin (e.g., the MJO has a stronger influence over the Indian-West Pacific Ocean region than over the Atlantic basin). However, skill improvements due to the inclusion of the selected predictors are within the same order of scale as Leroy and Wheeler (2008) and reliability curves show a dependable model. Reliability curves are highly influenced by the tendency of tropical cyclone observations to follow climatology, while the other predictors work to increase skill and “tighten” the reliability curve about the perfect forecast.

A caveat to the model is the lower sharpness (the capability of the model to deviate from its mean climatology; Vitart et al., 2010) that comes with statistical models. As discussed in the introduction, statistical models rarely predict very low or very high probabilities largely because of the great influence of climatology. Furthermore, the model currently requires ENSO and MJO activity to be present to improve skill over the time-varying climatology. ENSO-neutral seasons with weak MJO activity follow the known climatological probabilities in the forecasts.

Future work will focus on improving forecasting skill and forecast lead times. The inclusion of other predictors will also be considered. Predictors under consideration include the QBO (Gray, 1984b, 1990), an index of West African monsoon intraseasonal variability (Bunting et al., 1975; Gray, 1990; Gray et al., 1993; Landsea and Gray, 1992; Maloney and Shaman, 2008), the North Atlantic Oscillation (NAO; Elsner, 2003; Elsner et al. 2000, 2001; Molinari and Mestas-Nuñez, 2003), the Atlantic Multi-decadal

oscillation (AMO; Trenberth and Shea, 2006) and the Pacific Decadal Oscillation (PDO; Lupo et al., 2008).

Furthermore, additional spatial improvements can be examined. Differences in tropical cyclogenesis mechanisms have been observed in subregions of the Atlantic basin, therefore regional-scale prediction might benefit from different predictors (Ballenzweig, 1959; Goldenberg and Shapiro, 1993; Hess and Elsner, 1994; Hess et al., 1995).

Sensitivity tests conducted in this study by dividing the Atlantic basin into two and three subregions found that the logistic fitted MJO signal was strongest for the full basin.

Further sensitivity tests may reveal a better definition of subregions that may improve forecast skill. While spatial improvements can benefit predictor selection, it can also benefit preparedness. Knowing more specifically where a cyclone is likely to form will benefit those living nearby who may be affected (Lehmiller et al., 1997).

Ultimately, the goal of this study and the future work discussed is a successful operational real-time forecasting model. Once additional predictors have been implemented in the model, further work may also get at a better understanding of the physical basis behind some of the forecast relationships shown. This includes relationships between tropical cyclones and the predictors and between the various predictors.

References

1. Ballenzweig, E. M., 1959: Relation of long-period circulation anomalies to tropical storm formation and motion. *J. Meteor.*, **16**, 121-139.
2. Barrett, B.S., and L. M. Leslie, 2009: Links between tropical cyclone activity and Madden-Julian oscillation phase in the North Atlantic and northeast Pacific basins. *Mon. Wea. Rev.*, **137**, 727-744.
3. Battisti, D. S., and A. C. Hirst, 1989: Interannual variability in a tropical atmosphere-ocean model: Influence of basic state, ocean geometry and non-linearity. *J. Atmos. Sci.*, **46**, 1687-1712.
4. Bender, M. A., 1997: The effect of relative flow on the asymmetric structure in the interior of hurricanes. *J. Atmos. Sci.*, **54**, 703-724.
5. Bister, M., and K. Emanuel, 1997: The genesis of Hurricane Guillermo: TEXMEX analyses and a modeling study. *Mon. Wea. Rev.*, **125**, 2662-2682
6. Bosart, L. F., and J. A. Bartlo, 1991: Tropical storm formation in a baroclinic environment. *Mon. Wea. Rev.*, **119**, 1979-2013.
7. Brunkard, J., G. Namulanda, and R. Ratard, 2008: Hurricane Katrina Deaths, Louisiana, 2005. *Disaster Med Public Health Preparedness*, **2**, 215-223.
8. Bunting, A. H., M. D. Dennett, J. Elston, and J. R. Milford, 1975: Seasonal rainfall forecasting in West Africa. *Nature*, **253**, 622-623.
9. Camargo, S. J., K. A. Emanuel, A. H. Sobel, 2007: Use of a Genesis Potential Index to Diagnose ENSO Effects on Tropical Cyclone Genesis. *J. Climate*, **20**, 4819-4834.
10. Charney, J. G. and M. E. Stern, 1962: On the stability of internal baroclinic jets in a rotating atmosphere. *J. Atmos. Sci.*, **19**, 159-172.
11. Collins, J.M., 2007: The Relationship of ENSO and Relative Humidity to Interannual Variations of Hurricane Frequency in the North-East Pacific Ocean. *Papers of the Applied Geography Conferences*, **30**, 324-333.
12. Collins, J. M., and I. M. Mason, 2000: Local environmental conditions related to seasonal tropical cyclone activity in the Northeast Pacific basin. *Geophys. Res. Lett.*, **27**, 3881-3884.

13. Collins, J.M. and I.M. Mason, 2003: Seasonal Environmental Conditions Related to Hurricane Activity in the North East Pacific Basin. *New England St. Lawrence Valley Geographical Society Proceedings*, **33**, 44-50.
14. Chu, P.S., 2004: ENSO and tropical cyclone activity. *Hurricanes and Typhoons, Past, Present and Future*, R. J. Murnane and K.-B. Liu, Eds., Columbia University Press, 297–332.
15. DeMaria, M., 1996: The effect of vertical shear on tropical cyclone intensity change. *J. Atmos. Sci.*, **53**, 2076-2087.
16. Dunkerton, T. J., M. T. Montgomery, and Z. Wang, 2009: Tropical Cyclogenesis in a tropical wave critical layer: easterly waves. *Atmos. Chem. Phys.*, **9**, 5587-5646.
17. Elsner, J. B., 2003: Tracking hurricanes. *Bull. Amer. Meteor. Soc.*, **84**, 353-356.
18. Elsner, J. B., and C. P. Schmertmann, 1993: Improving extended-range seasonal predictions of intense Atlantic hurricane activity. *Wea. Forecasting*, **8**, 345-351.
19. Elsner, J. B., and C. P. Schmertmann, 1994: Assessing forecast skill through cross validation. *Wea. Forecasting*, **9**, 619-624.
20. Elsner, J. B., K. B. Liu, and B. Kocher, 2000: Spatial variations in major U.S. hurricane activity: Statistics and a physical mechanism. *J. Climate*, **13**, 2293-2305.
21. Elsner, J. B., B. H. Bossak, and X. -F. Niu, 2001: Secular changes to the ENSO-U.S. hurricane relationship. *Geophys. Res. Lett.*, **28**, 4123-4126.
22. Emanuel, K. A., 1988: Toward a general theory of hurricanes. *Amer. Sci.*, **76**, 370-379.
23. Emanuel, K. A., 1989: The finite-amplitude nature of tropical cyclogenesis. *J. Atmos. Sci.*, **46**, 3431-3456.
24. Emanuel, K. A., 2005. *Divine Wind: The History and Science of Hurricanes*. Oxford University Press, 285 pp.
25. Emanuel, K. A. and David S. Nolan, 2004: Tropical Cyclone Activity and the Global Climate System. *Preprints, 26th AMS Conference on Hurricanes and Tropical Meteorology*, Miami Beach, May, 2004.
26. Frank, N. L., 1979: Atlantic tropical systems of 1969. *Mon. Wea. Rev.*, **98**, 124-129.
27. Frank, N. L., and G. B. Clark, 1980: Atlantic tropical systems of 1979. *Mon. Wea. Rev.*, **108**, 966-972.

28. Frank, W. M., and P. E. Roundy, 2006: The role of tropical waves in tropical cyclogenesis. *Mon. Wea. Rev.*, **134**, 2397-2417.
29. Fritz, H. M.; C. D. Blount, S. Thwin, M. K. Thu, and N. Chan, 2009: Cyclone Nargis storm surge in Myanmar. *Nature Geoscience*, **2**, 448-449.
30. Gill, A.E., 1980: Some simple solutions for heat induced tropical circulation. *Quart. J. Roy. Meteor. Soc.*, **106**, 447-462.
31. Goldenberg, S. B., and L. J. Shapiro, 1996: Physical mechanism for the association of El Niño and West African rainfall with Atlantic major hurricane activity. *J. Climate*, **9**, 1169–1187.
32. Gray, W. M., 1968: Global view of the origin of tropical disturbances and storms. *Mon. Wea. Rev.*, **96**, 669–700.
33. Gray, W. M., 1979: Hurricanes: Their formation, structure and likely role in the tropical circulation. *Meteorology over Tropical Oceans*, D. B. Shaw, Ed., Royal Meteorological Society, 155–218.
34. Gray, W. M., 1990: Strong association between West African rainfall and U.S. landfall of intense hurricanes. *Science*, **249**, 1251-1256.
35. Gray, W. M., 1998: The Formation of Tropical Cyclones. *Meteorol. Atmos. Phys.*, **67**, 37-69.
36. Gray, W. M., 1984a: Atlantic Seasonal Hurricane Frequency. Part I: El Niño and 30 mb Quasi-Biennial Oscillation Influences. *Mon. Wea. Rev.*, **112**, 1649–1668.
37. Gray, W. M., 1984b: Atlantic Seasonal Hurricane Frequency. Part II: Forecasting its Variability. *Mon. Wea. Rev.*, **112**, 1669–1683.
38. Gray, W. M. and J. D. Sheaffer, 1991: El Niño and QBO influences on tropical cyclone activity. *Teleconnections linking worldwide climate anomalies*, M. H. Glantz, R. W. Katz, and N. Nicholls, Ed., Cambridge University Press, 257-284.
39. Gray, W. M., Christopher W. Landsea, Paul W. Mielke, Kenneth J. Berry, 1992: Predicting Atlantic Seasonal Hurricane Activity 6–11 Months in Advance. *Wea. Forecasting*, **7**, 440–455.
40. Gray, W. M., C. W. Landsea, P. W. Mielke, Jr., and K. J. Berry, 1993: Predicting Atlantic basin seasonal tropical cyclone activity by 1 August. *Wea. Forecasting*, **8**, 73-86.

41. Gray, W. M., C. W. Landsea, P. W. Mielke, Jr., and K. J. Berry, 1994: Predicting Atlantic basin seasonal tropical cyclone activity by 1 June. *Wea. Forecasting*, **9**, 103-115.
42. Halpern, D., 2002: Offshore Ekman transport and Ekman pumping off Peru during the 1997–1998 El Niño, *Geophys. Res. Lett.*, **29**, 1075, doi:10.1029/2001GL014097.
43. Halpert M. S., and C. F. Ropelewski, 1992: Surface temperature patterns associated with the Southern Oscillation. *J. Climate*, **5**, 577-593.
44. Hastenrath, S., 1990: Tropical climate prediction: a progress report, 1985-1990. *Bull. Amer. Meteor. Soc.*, **71**, 819-825.
45. Heckley, W. A., and A. E. Gill, 1984: Some simple solutions to the problem of forced equatorial long waves. *Quart. J. Roy. Meteor. Soc.*, **110**, 203–217.
46. Hendon, H. H. and M. L. Salby, 1994: The life cycle of the Madden-Julian Oscillation. *J. Atmos. Sci.*, **51**, 2225-2237.
47. Hess, J. C., and J. B. Elsner, 1994: Historical developments leading to current forecast models of annual Atlantic hurricane activity. *Bull. Amer. Meteor. Soc.*, **75**, 1611-1621.
48. Hess, J. C., J. B. Elsner, and N. E. LaSeur, 1995: Improving seasonal predictions for the Atlantic basin. *Wea. Forecasting*, **10**, 425-432.
49. Holland, G.J. (ed.), 1993: The Global Guide to Tropical Cyclone Forecasting. WMO/TD-560, World Meteorological Organization, Geneva, 337.
50. Horel, J. D., and J. M. Wallace, 1981: Planetary-scale atmospheric phenomena associated with the Southern Oscillation. *Mon. Wea. Rev.*, **109**, 813-829.
51. Hosmer, D. W. and S. Lemeshow, 2000: Applied Logistic Regression. 2nd ed. Wiley, 373 pp.
52. Irwin, R. P., and R. E. Davis, 1999: The relationship between the Southern Oscillation Index and tropical cyclone tracks in the eastern North Pacific. *Geophys Res. Lett.*, **20**, 2251-2254.
53. Jarvinen, B.R., C.J. Neumann, and M.A.S. Davis, 1984: A tropical cyclone data tape for the North Atlantic basin, 1886-1983. NOAA Tech. Memo. NWS-NHC 22, 21 pp. (available at <http://www.nhc.noaa.gov/pdf/NWS-NHC-1988-22.pdf>)
54. Kalnay, E., and Coauthors, 1996: The NCEP/NCAR 40-Year Reanalysis Project. *Bull. Amer. Meteor. Soc.*, **77**, 437-471.

55. Kim, H. -M., P. J. Webster, and J. A. Curry, 2009: Impact of shifting patterns of Pacific Ocean warming on North Atlantic tropical cyclones. *Science*, **325**, 77-80.
56. King, G., and L. Zeng, 2001: Logistic Regression in Rare Events Data. *Political Analysis*, **9**, 137-163.
57. Kloesel, K. A., and B. A. Albrecht, 1989: Low-Level Inversions over the Tropical Pacific—Thermodynamic Structure of the Boundary Layer and the Above-Inversion Moisture Structure. *Mon. Wea. Rev.*, **117**, 87–101.
58. Klotzbach, Philip J., 2010: On the Madden–Julian Oscillation–Atlantic Hurricane Relationship. *J. Climate*, **23**, 282–293.
59. Landsea, C. W., 1993: A climatology of intense (or major) Atlantic hurricanes. *Mon. Wea. Rev.*, **121**, 1703-1713.
60. Landsea, C. W., and W. M. Gray, 1992: The strong association between western Sahelian monsoon rainfall and intense Atlantic hurricanes. *J. Climate*, **5**, 435-452.
61. Landsea, C. W., R. A. Pielke Jr., A. M. Mestas-Nuñez, and J. A. Knaff, 1999: Atlantic basin hurricanes: Indices of climatic changes. *Climatic Change*, **42**, 89–129.
62. Lau, K. M., L. Peng, C. H. Sui, and T. Nakazawa, 1989: Dynamics of super cloud clusters, westerly wind bursts, 30–60 day oscillations, and ENSO: A unified view. *J. Meteor. Soc. Japan*, **67**, 205–219.
63. Lehmiller, G. S., T. B. Kimberlain, and J. B. Elsner, 1997: Seasonal prediction models for North Atlantic basin hurricane location. *Mon. Wea. Rev.*, **125**, 1780-1791.
64. Leroy, A., and M. C. Wheeler, 2008: Statistical Prediction of Weekly Tropical Cyclone Activity in the Southern Hemisphere. *Mon. Wea. Rev.*, **136**, 3637–3654.
65. Liebmann, B., and C. A. Smith, 1996: Description of a complete (interpolated) outgoing longwave radiation dataset. *Bull. Amer. Meteor. Soc.*, **77**, 1275-1277.
66. Lighthill, J., G.J. Holland, W.M. Gray, C. Landsea, K. Emanuel, G. Craig, J. Evans, Y. Kurihara, and C.P. Guard, 1994: Global climate change and tropical cyclones. *Bull. Amer. Met. Soc.*, **75**, 2147-2157.
67. Lin, J. –L., and Coauthors, 2006: Tropical intraseasonal variability in 14 IPCC AR4 climate models. Part I: Convective signals. *J. Climate*, **19**, 2665-2690.

68. Lupo, A. R., T. K., Latham, T.H. Magill, J.V. Clark, C.J.Melick, and P. S. Market, 2008: The interannual variability of hurricane activity in the Atlantic and East Pacific regions. *Nat. Wea. Digest*, **32** (2), 119-135.
69. Madden, R. A., and P. Julian, 1971: Detection of a 40-50 day oscillation in the zonal wind in the Tropical Pacific. *J. Atmos. Sci.*, **28**, 702-708.
70. Madden, R. A., and P. Julian, 1972: Description of a global-scale circulation cells in the tropics with a 40-50 day period. *J. Atmos. Sci.*, **29**, 1109-1123.
71. Madden, R. A., and P. Julian, 1994: Observations of the 40-50 day tropical oscillation – a review. *Mon. Wea. Rev.*, **123**, 814-837.
72. Magaña, V., J. A. Amador, and S. Medina, 1999: The midsummer drought over Mexico and Central America. *J. Climate*, **12**, 1577-1588.
73. Maloney, E. D., and D. L. Hartmann, 1998: Frictional moisture convergence in a composite life cycle of the Madden-Julian oscillation. *J. Climate*, **11**, 2387-2403.
74. Maloney, E. D., and D. L. Hartmann, 2000a: Modulation of eastern North Pacific hurricanes by the Madden-Julian oscillation. *J. Climate*, **13**, 1451-1460.
75. Maloney, E. D., and D. L. Hartmann, 2000b: Modulation of hurricane activity in the Gulf of Mexico by the Madden–Julian oscillation. *Science*, **287**:2002–2004.
76. Maloney, E. D., and D. L. Hartmann, 2001: The Madden–Julian oscillation, barotropic dynamics, and North Pacific tropical cyclone formation. Part I: Observations. *J. Atmos. Sci.*, **58**, 2545–2558.
77. Maloney, E. D., and S. K. Esbensen, 2005: A modeling study of summertime east Pacific wind-induced ocean-atmosphere exchange in the intraseasonal oscillation. *J. Climate*, **18**, 568-584.
78. Maloney, E. D., and J. Shaman, 2008: Intraseasonal variability of the West African monsoon and Atlantic ITCZ. *J. Climate*, **21**, 2898-2918.
79. Mathworks, 2011: Global optimization toolbox: User’s guide (r2011b). Retrieved May 18, 2011.
80. McCullagh, P. and J.A. Nelder, 1989: Generalized Linear Models. 2nd ed. Chapman & Hall/CRC, Boca Raton, Florida.
81. McPhaden, M. C., 1999: Genesis and evolution of the 1997-98 El Niño. *Science*, **283**, 950-954.

82. Meinen, C. S., and M. J. McPhaden, 2000: Observations of warm water volume changes in the equatorial Pacific and their relationship to El Niño and La Niña. *J. Climate*, **13**, 3551-3559.
83. Mo, K. C., 2000: The association between intraseasonal oscillations and tropical storms in the Atlantic basin. *Mon. Wea. Rev.*, **128**, 4097-4107.
84. Molinari, J., and D. Vollaro, 2000: Planetary- and synoptic-scale influences on Eastern Pacific Tropical Cyclogenesis. *Mon. Wea. Rev.*, **128**, 3296-3307.
85. Molinari, J., D. Knight, M. Dickinson, D. Vollaro, and S. Skubis, 1997: Potential vorticity, easterly waves, and eastern Pacific tropical cyclogenesis. *Mon. Wea. Rev.*, **125**, 2699-2708.
86. Molinari, J., S. Skubis, and M. Dickinson, 2000: Origins and mechanisms of eastern Pacific tropical cyclogenesis: A case study. *Mon. Wea. Rev.*, **128**, 125-139.
87. Molinari, R., and A. M. Mestas-Núñez, 2003: North Atlantic decadal variability and the formation of tropical storms and hurricanes. *Geophys. Res. Lett.*, **30** (10), 1541.
88. Moller J. D., and M. T. Montgomery, 1999: Vortex Rossby waves and hurricane intensification in a barotropic model. *J. Atmos. Sci.*, **56**, 1674-1687.
89. Moller J. D., and M. T. Montgomery, 2000: Tropical cyclone evolution via potential vorticity anomalies in a three-dimensional balance model. *J. Atmos. Sci.*, **57**, 3366-3387.
90. Montgomery, M. T., and B. F. Farrell, 1993: Tropical cyclone formation. *J. Atmos. Sci.*, **50**, 285-310.
91. Montgomery, M. T., and J. Enagonio, 1998: Tropical cyclogenesis via convectively forced vortex Rossby waves in a three-dimensional quasi-geostrophic model. *J. Atmos.*, **55**, 3176-3207.
92. Montgomery, M. T., M. E. Nicholls, T. A. Cram, and A. B. Saunders, 2006: A vertical hot tower route to tropical cyclogenesis. *J. Atmos. Sci.*, **63**, 355-386.
93. Nelder, John, and R. Wedderburn, 1972: Generalized linear models. *Journal of the Royal Statistical Society. Series A (General)*, **135** (3): 370-384.
94. Neumann, C. J., B. R. Jarvinen, C. J. McAdie, and G. R. Hammer, 1999: Tropical Cyclones of the North Atlantic Ocean, 1871 -1998, NOAA, Silver Spring, Md., 206 pp.

95. Pegion, K., P. Pegion, T. DelSole, and M. Sirbu, 2008: Subseasonal variability of hurricane activity. *Climate Test Bed Joint Seminar Series*, NOAA, NCEP, Camp Springs, Maryland, 10 December 2008.
96. Pielke Jr., R. A., J. Gratz, C. W. Landsea, D. Collins, M. A. Saunders, and R. Musulin, 2008: Normalized hurricane damage in the United States: 1900–2005. *Nat. Hazards Rev.*, **9**, 29–42.
97. Rappaport, E. N., 1999: Atlantic hurricane season of 1997. *Mon. Wea. Rev.*, **127**, 2012–2026.
98. Rasmusson, E. M., and T. H. Carpenter, 1982: Variations in tropical sea surface temperature and surface wind fields associated with the Southern Oscillation/ El Niño. *Mon. Wea. Rev.*, **110**, 354–384.
99. Rasmusson, E. M. and J. M. Wallace, 1983: Meteorological aspects of the El Niño/Southern Oscillation. *Science*, **222**:1195–1202.
100. Rayner, N. A.; Parker, D. E.; Horton, E. B.; Folland, C. K.; Alexander, L. V.; Rowell, D. P.; Kent, E. C.; Kaplan, A., 2003: Global analyses of sea surface temperature, sea ice, and night marine air temperature since the late nineteenth century, *J. Geophys. Res.*, **108**, No. D14, 4407.
101. Reynolds, R. W., N. A. Rayner, T. M. Smith, D. C. Stokes, and W. Wang, 2002: An Improved In Situ and Satellite SST Analysis for Climate. *J. Climate*, **15**, 1609–1625.
102. Riehl, Herbert, 1948a: On the formation of West Atlantic hurricanes. *Miscellaneous Report*, No. 24, Part 1, Department of Meteorology, University of Chicago, 1-67.
103. Riehl, Herbert, 1948b: On the formation of typhoons. *J. Meteor.*, **5**, 247–264.
104. Riehl, Herbert, 1950: A model of hurricane formation. *J. App. Phys.*, **21**, 917–925.
105. Ritchie, E. A., and G. Holland, 1997: Scale interaction during the formation of typhoon Irving. *Mon. Wea. Rev.*, **125**, 1377–1396.
106. Ross, T. and N. Lott, cited. 2003: A climatology of 1980–2003 extreme weather and climate events. National Climatic Data Center Tech. Rep. 2003–01, NOAA/NESDIS, National Climatic Data Center, Asheville, NC. [Available online at <http://www.ncdc.noaa.gov/ol/reports/billionz.html>.]
107. Rotunno, R., and K. Emanuel, 1987: An air-sea interaction theory for tropical cyclones. Part II: Evolutionary study using a non-hydrostatic axisymmetric numerical model. *J. Atmos. Sci.*, **44**, 542–561.

108. Rui, Hualan, Bin Wang, 1990: Development Characteristics and Dynamic Structure of Tropical Intraseasonal Convection Anomalies. *J. Atmos. Sci.*, **47**, 357–379.
109. Sadler J. C., 1976: A role of the tropical upper tropospheric trough in early season typhoon development. *Mon. Wea. Rev.*, **104**, 1266-1278.
110. Saji, N. H., B. N. Goswami, P. N. Vinayachandran, and T. Yamagata, 1999: A dipole mode in the tropical Indian Ocean. *Nature*, **401**, 360-363.
111. Salby, M. L., and H. H. Hendon, 1994: Intraseasonal behavior of clouds, temperature and motion in the tropics, *J. Atmos. Sci.*, **51**, 2207-2224.
112. Shaman, Jeffrey, Steven K. Esbensen, Eric D. Maloney, 2009: The Dynamics of the ENSO–Atlantic Hurricane Teleconnection: ENSO-Related Changes to the North African–Asian Jet Affect Atlantic Basin Tropical Cyclogenesis. *J. Climate*, **22**, 2458–2482.
113. Shapiro, L. J., 1987: Month-to-month variability of the Atlantic tropical circulation and its relationship to tropical storm formation. *Mon. Wea. Rev.*, **115**, 1598-1614.
114. Shinoda, T., H. H. Hendon, and J. Glick, 1998: Intraseasonal variability of surface fluxes and sea surface temperature in the tropical Indian and Pacific oceans, *J. Clim.*, **11**, 1685–1702.
115. Simpson, R. H., 1974: The hurricane disaster potential scale. *Weatherwise*, **27**, 169,186.
116. Slingo, J. M., and Coauthors, 1996: Intraseasonal oscillation in 15 atmospheric general circulation models: Results from an AMIP diagnostic subproject. *Climate Dyn.*, **12**, 325-357.
117. Sobel, Adam H., Christopher S. Bretherton, 1999: Development of Synoptic-Scale Disturbances over the Summertime Tropical Northwest Pacific. *J. Atmos. Sci.*, **56**, 3106–3127.
118. Thorncroft, C., and K. Hodges, 2001: African easterly wave variability and its relationship to Atlantic tropical cyclone activity. *J. Climate*, **14**, 1166-1179.
119. Trenberth, K. E., and D. P. Stepaniak, 2001: Indices of El Niño evolution. *J. Climate*, **14**, 1697-1701.
120. Trenberth, K. E., and D. J. Shea, 2006: Atlantic hurricanes and natural variability in 2005. *Geophys. Res. Lett.*, **33**, L12704.

121. Uppala, S. M., and Coauthors, 2005: The ERA-40 re-analysis. *Quart. J. Roy. Meteor. Soc.*, **131**, 2961-3012.
122. Vitart, F., 2009: Impact of the Madden-Julian Oscillation on tropical storms and risk of landfall in the ECMWF forecast system. *Geophys. Res. Lett.*, **36**, L15802, doi:10.1029/2009GL039089.
123. Vitart, F., and F. Molteni, 2009: Simulation of the MJO and its teleconnections in an ensemble of 46-day EPS hindcasts. ECMWF Tech Memo. 597, ECMWF, 60 pp. [Available at <http://www.ecmwf.int/publications/library/do/references/list/14>.]
124. Vitart, F., A. Leroy, and M. C. Wheeler, 2010: A comparison of dynamical and statistical predictions of weekly tropical cyclone activity in the southern hemisphere. *Mon. Wea. Rev.*, **138**, 3671-3682.
125. Wheeler, M. C., and H. H. Hendon, 2004: An all-season real-time multivariate MJO index: Development of an index for monitoring and prediction. *Mon. Wea. Rev.*, **132**, 1917-1932.
126. Whitney, L. D., and J. Hobgood, 1997: The relationship between sea surface temperatures and maximum intensities of tropical cyclones in the eastern North Pacific Ocean. *J. Climate*, **10**, 2921-2930.
127. Wilks, D. S., 2006: Statistical methods in the atmospheric sciences. Academic Press, 648 pp.
128. Wolff, J. O., E. Maier-Raimer, and S. Legutke, 1997: The Hamburg ocean primitive equation model. Deutsches Klimarechenzentrum Tech. Rep. 13, Hamburg, Germany, 98 pp.
129. Wyrtki, K., 1982: The Southern Oscillation, ocean-atmosphere interaction and El Niño. *Marine Technical Society Journal*, **16**, 3-10.
130. Yeh, S. -W, J. -S. Kug, B. Dewitte, M. -H. Kwon, B. P. Kirtman, and F. -F. Jin, 2009: El Niño in a changing climate. *Nature*, **461**, 511-514.
131. Yu, W., W. Han, D. Gochis, E.D Maloney, and S.-P. Xie, 2011: Observations of eastward propagation of atmospheric intraseasonal oscillations from the Pacific to the Atlantic. *J. Geophys. Res.*, **116**, D02101, doi:10.1029/2010JD014336.
132. Zehr, R. M., 1992: Tropical cyclogenesis in the western North Pacific. NOAA Tech. Rep. NESDIS 61, 181 pp. [Available from U.S. Department of Commerce, NOAA/NESDIS, 5200 Auth Rd., Washington, D.C. 20233.]
133. Zhang, C., 2005: The Madden-Julian Oscillation. *Rev. Geophys.*, **43**, RG2003, doi:10.1029/2004RG000158.

Appendix I

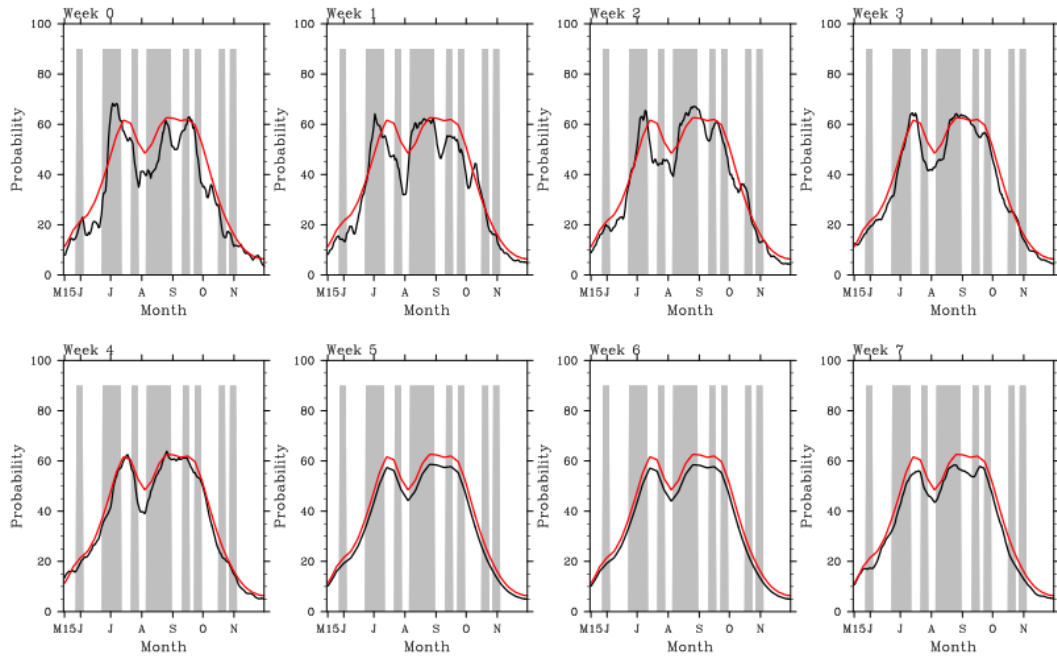


Fig. 30: East Pacific hindcast for 1975

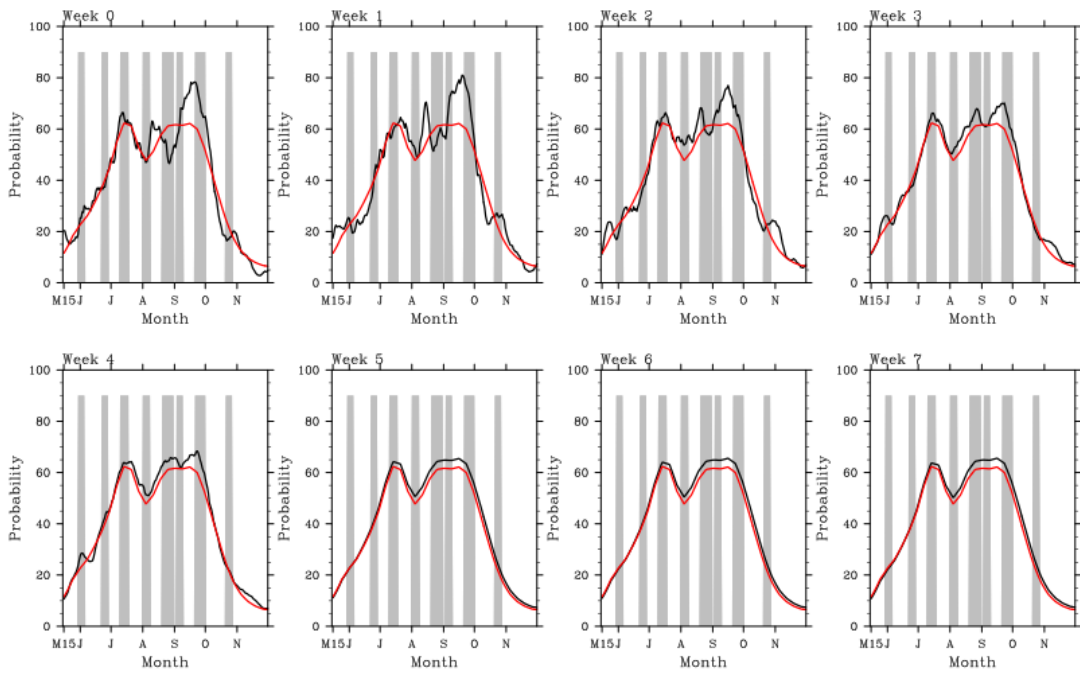


Fig. 31: East Pacific hindcast for 1976

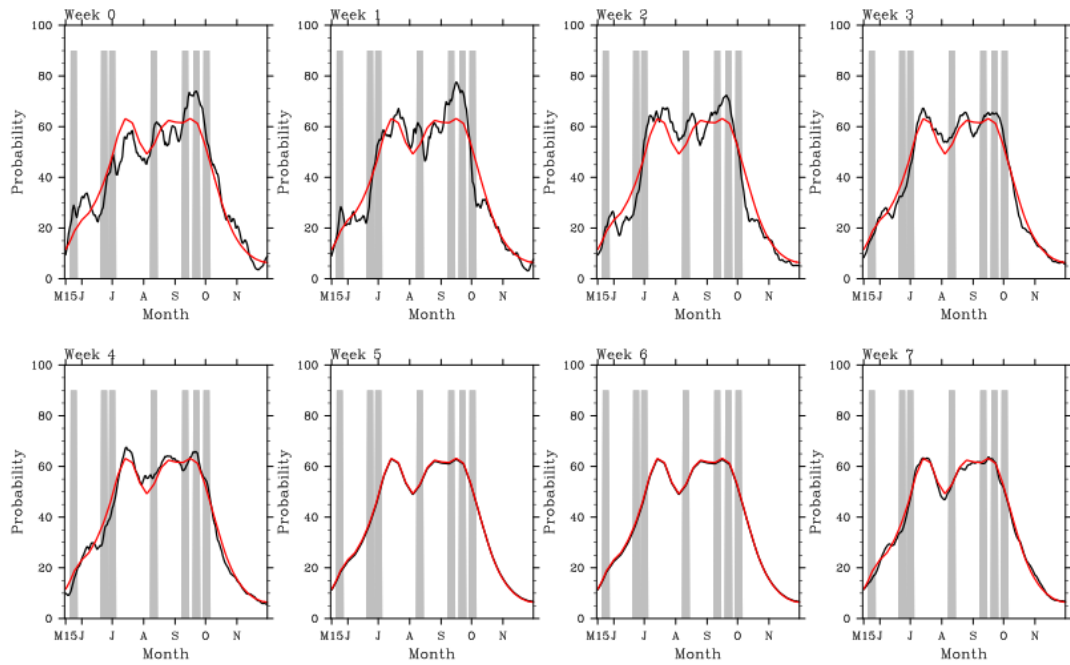


Fig. 32: East Pacific hindcast for 1977

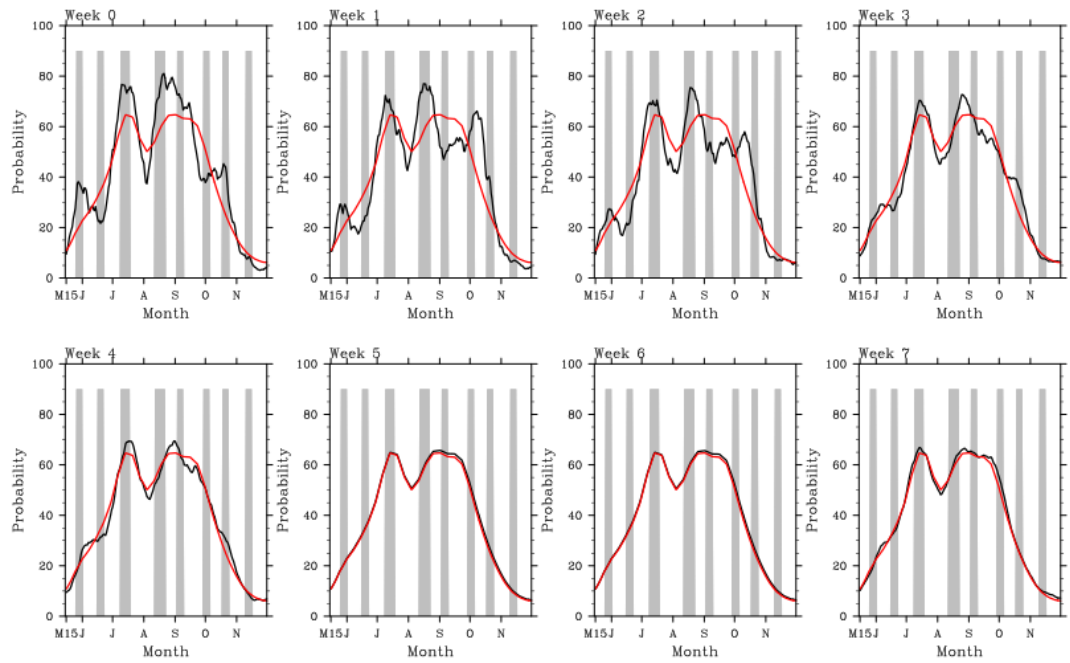


Fig. 33: East Pacific hindcast for 1979

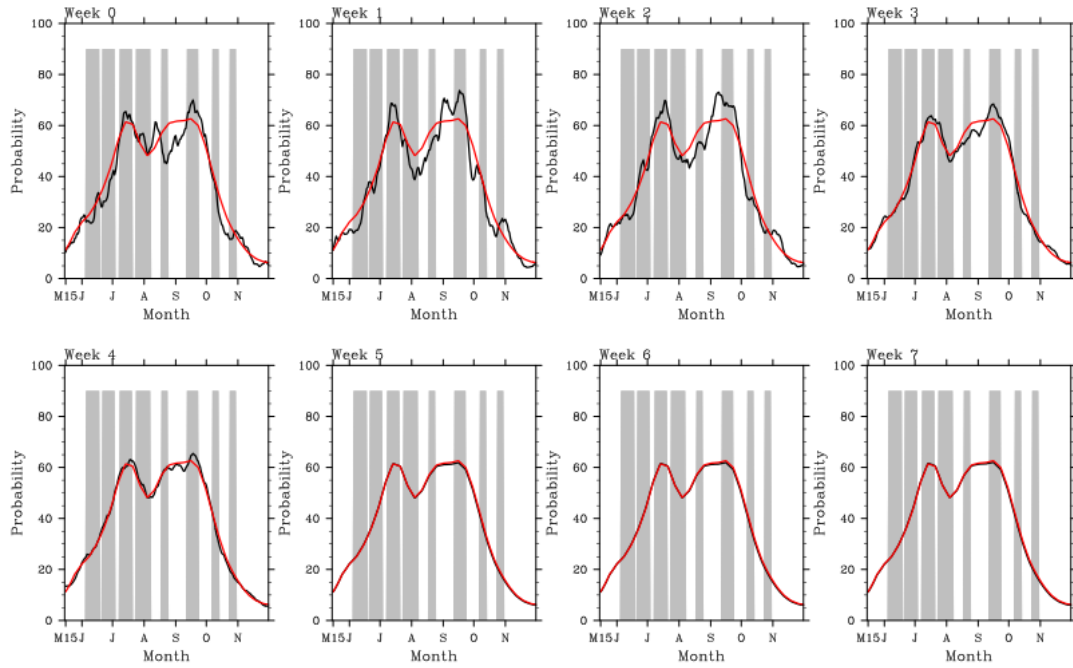


Fig. 34: East Pacific hindcast for 1980

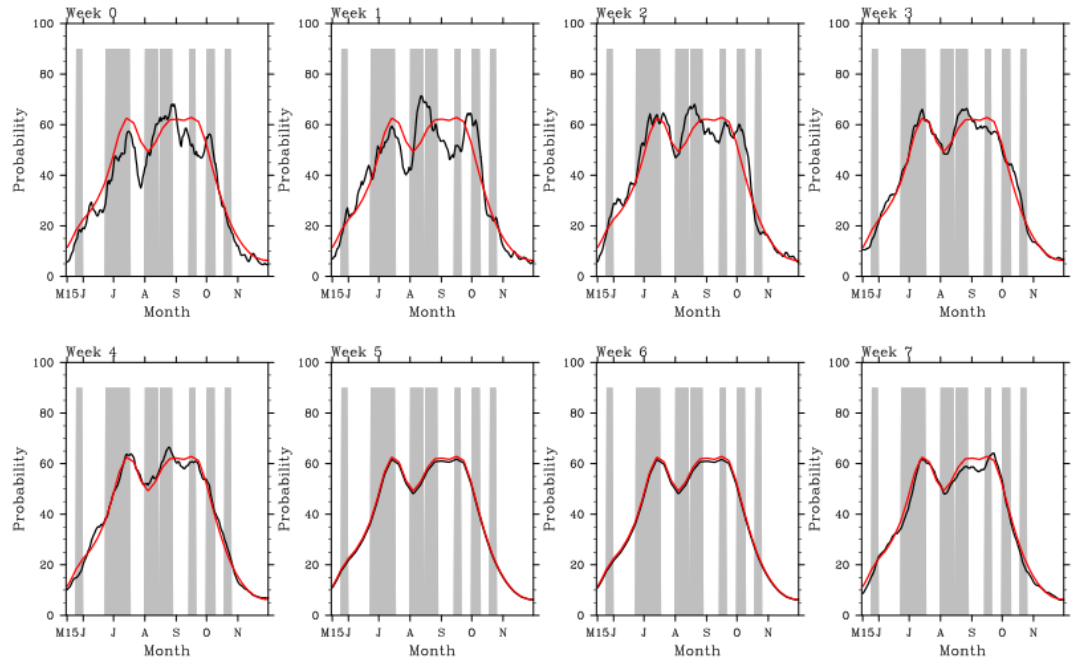


Fig. 35: East Pacific hindcast for 1981

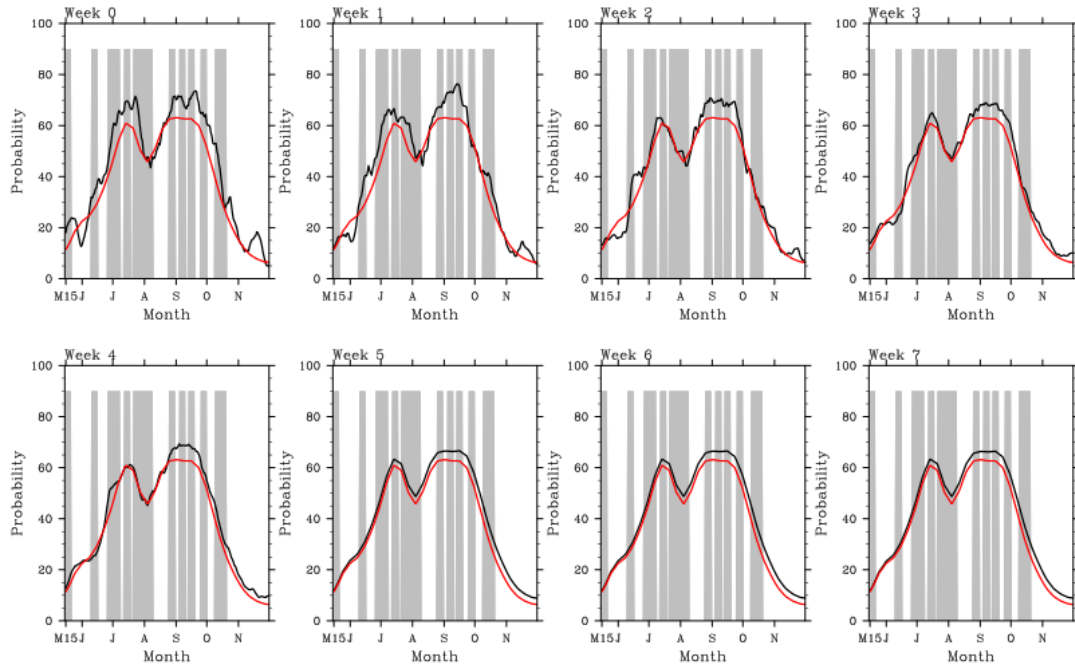


Fig. 36: East Pacific hindcast for 1982

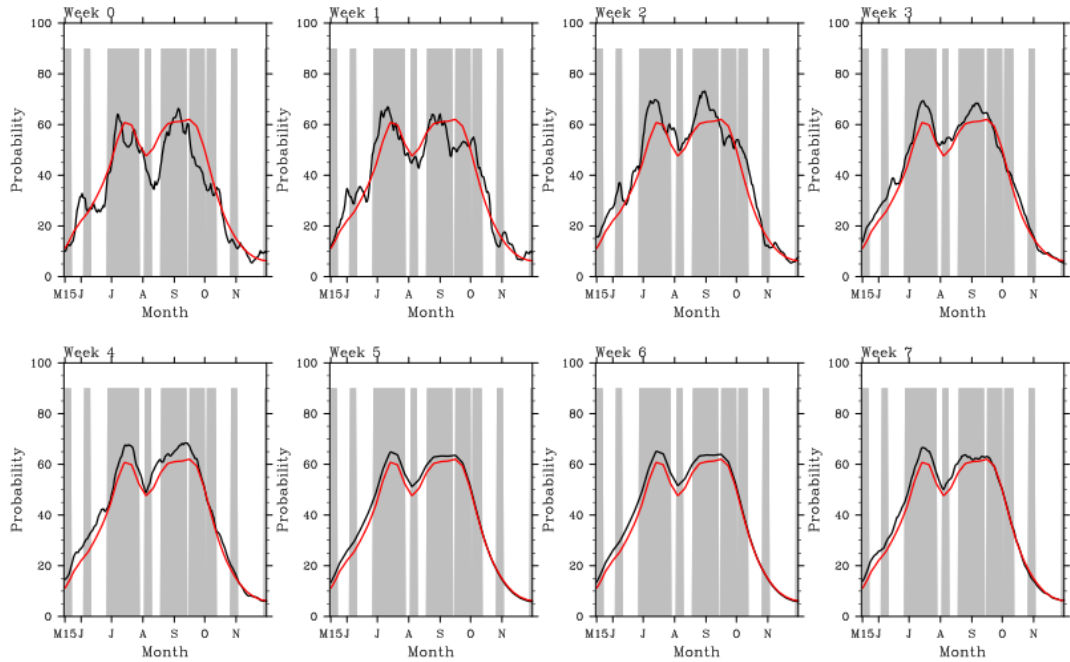


Fig. 37: East Pacific hindcast for 1983

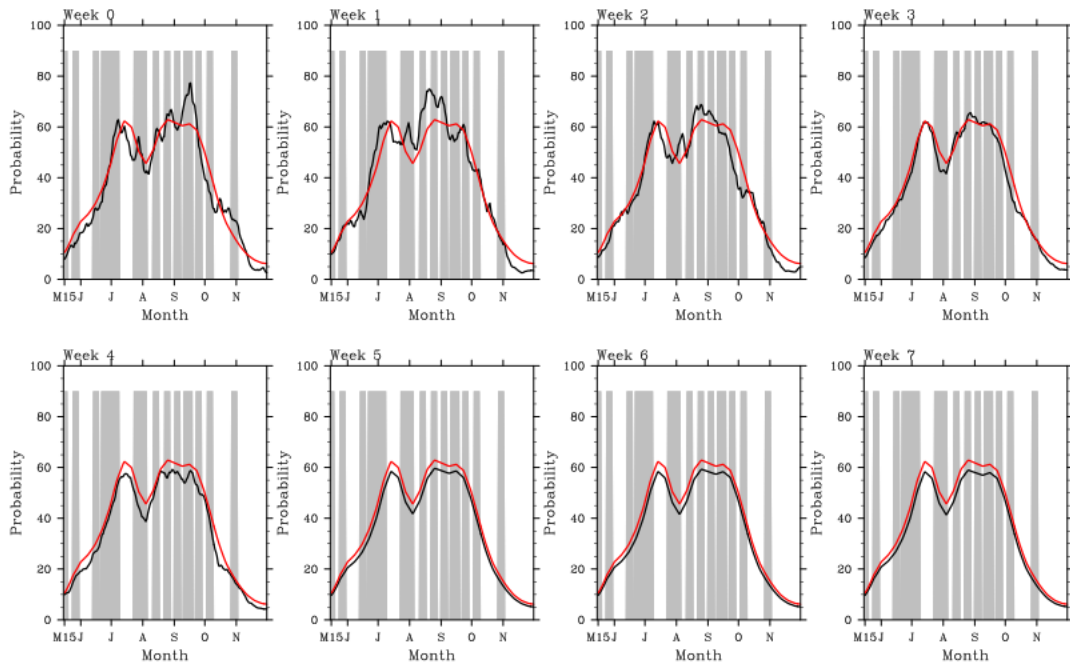


Fig. 38: East Pacific hindcast for 1984

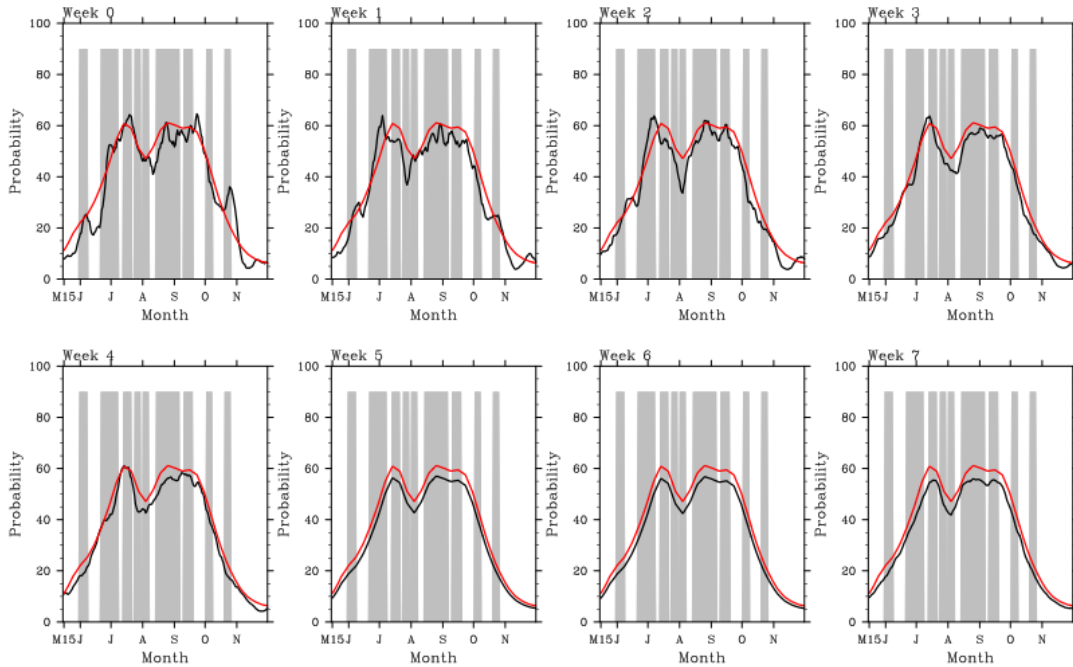


Fig. 39: East Pacific hindcast for 1985

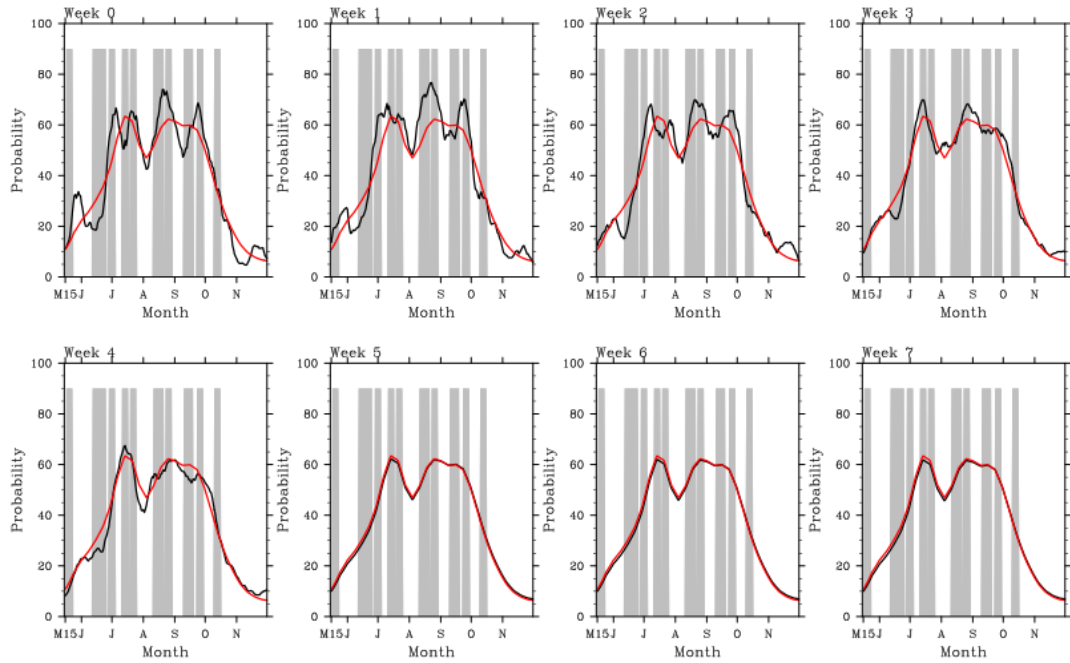


Fig. 40: East Pacific hindcast for 1986

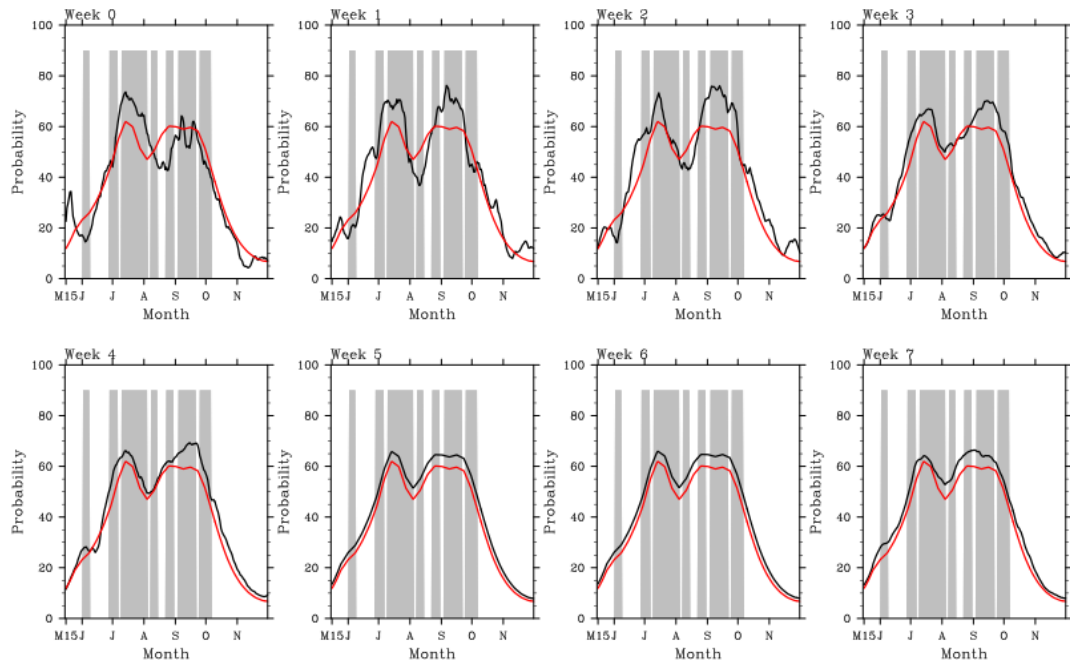


Fig. 41: East Pacific hindcast for 1987

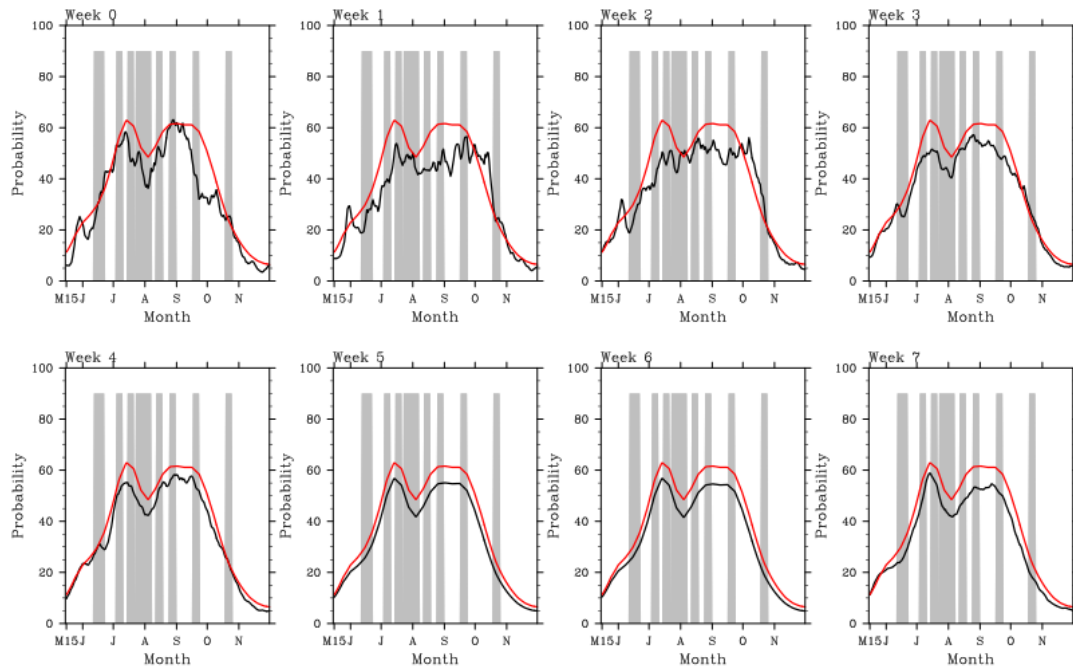


Fig. 42: East Pacific hindcast for 1988

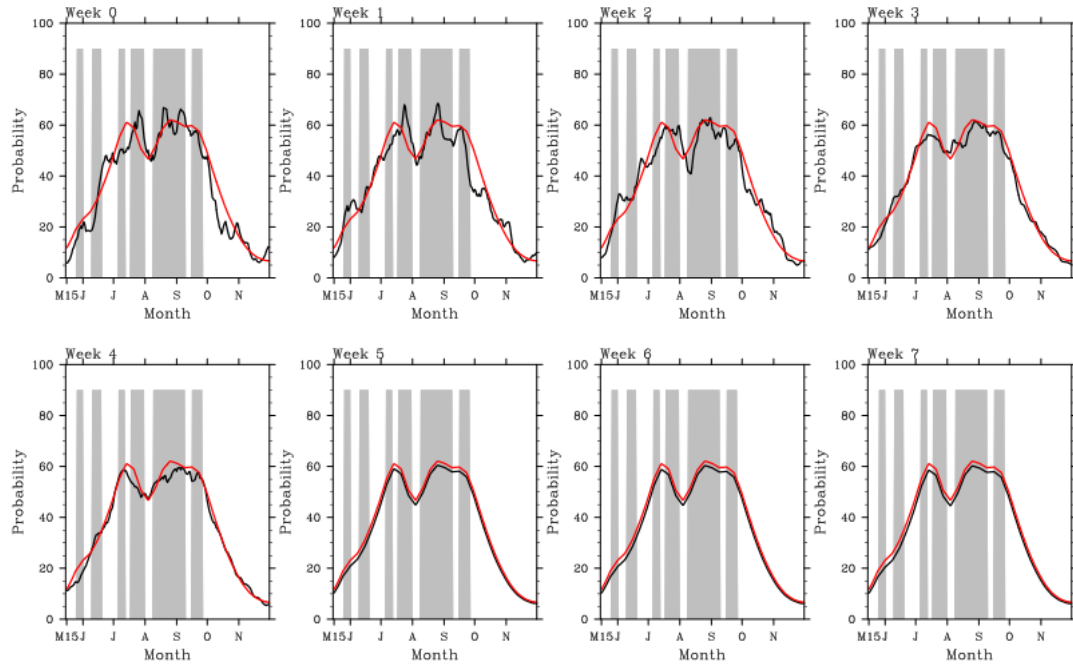


Fig. 43: East Pacific hindcast for 1989

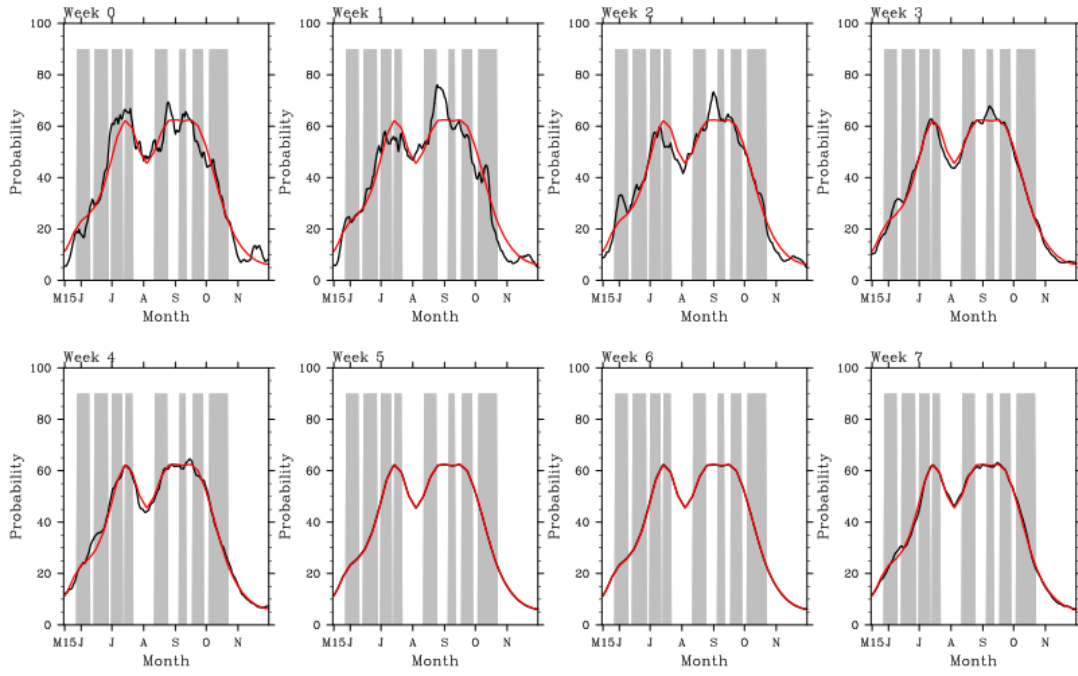


Fig. 44: East Pacific hindcast for 1990

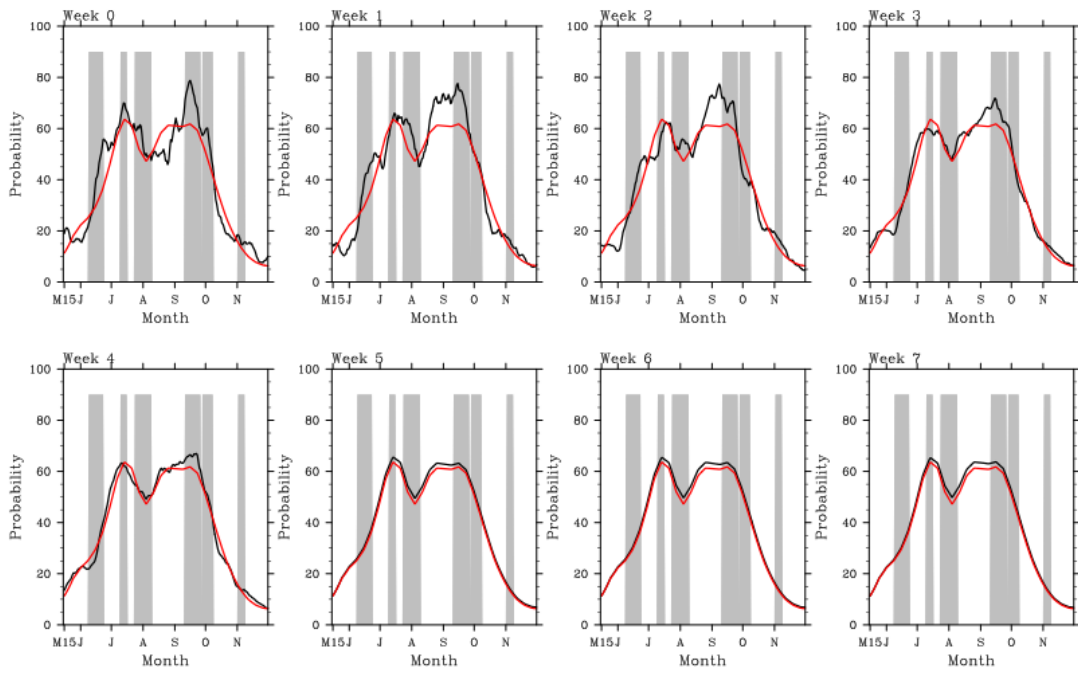


Fig. 45: East Pacific hindcast for 1991

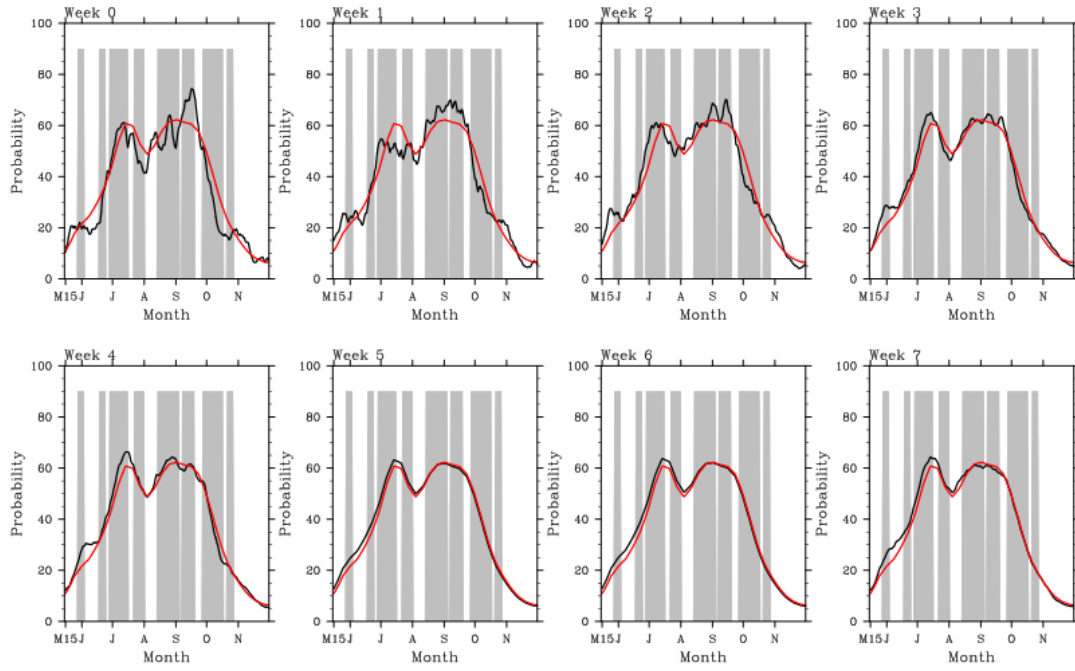


Fig. 46: East Pacific hindcast for 1992

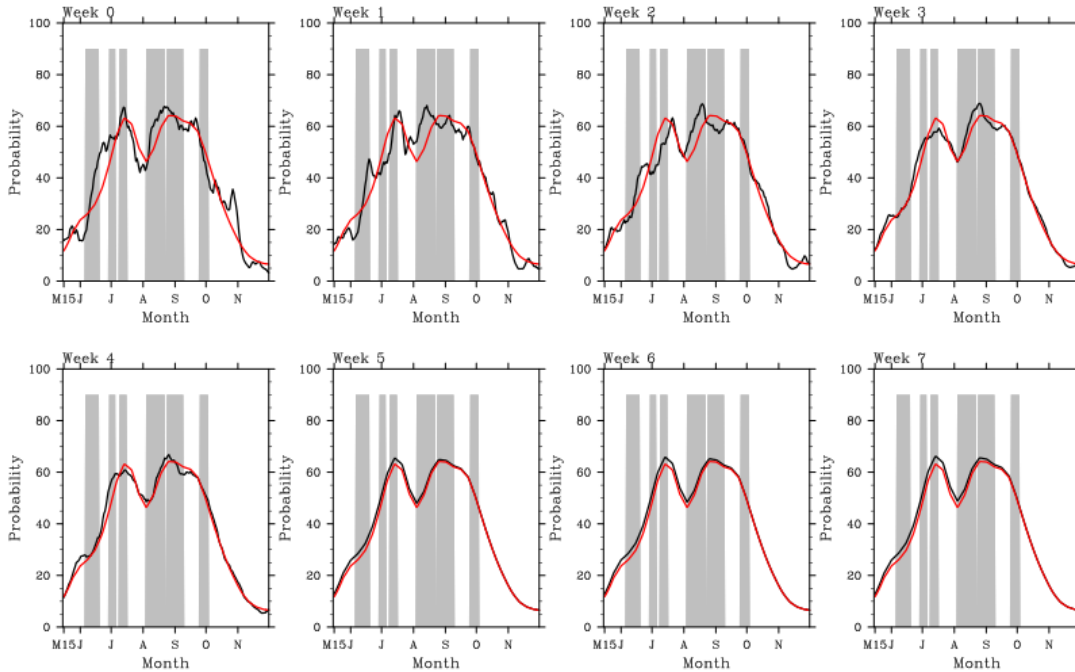


Fig. 47: East Pacific hindcast for 1993

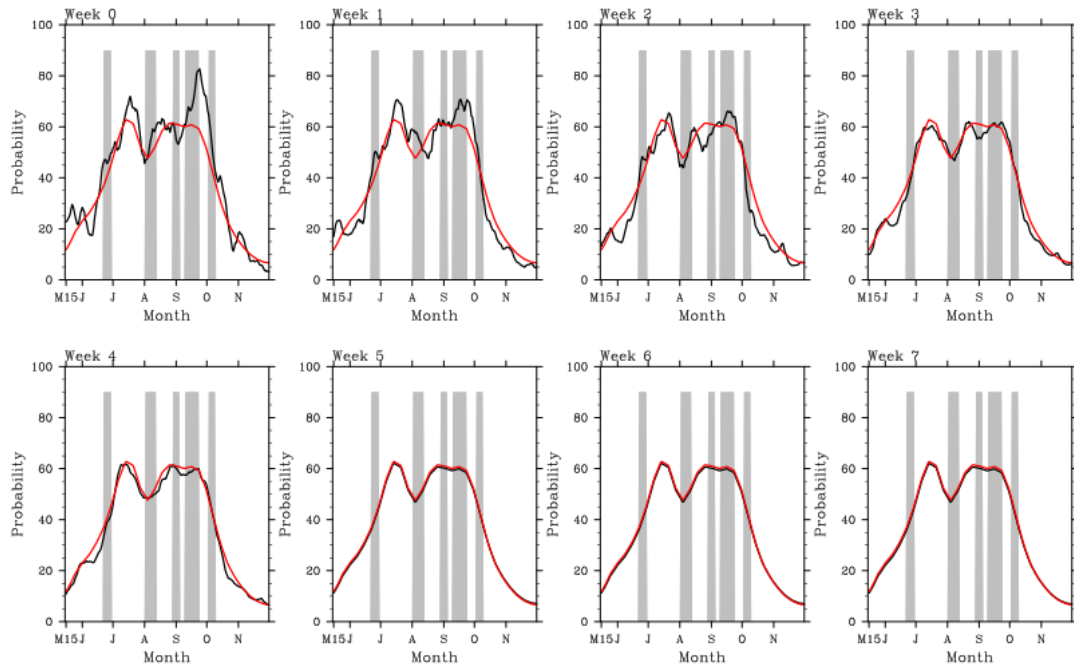


Fig. 48: East Pacific hindcast for 1994

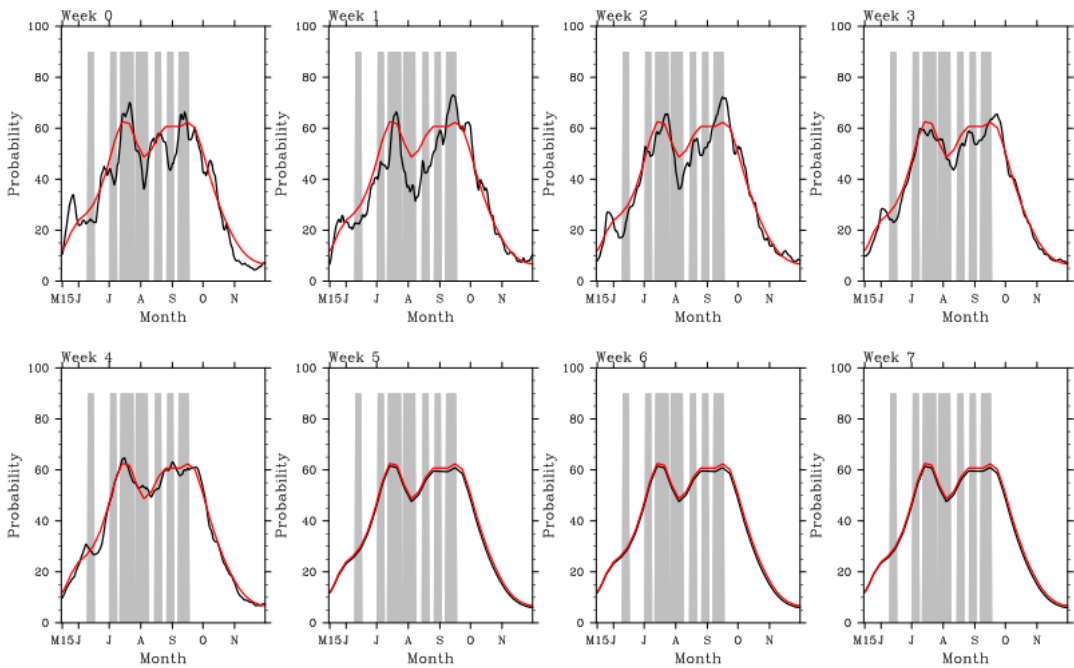


Fig. 49: East Pacific hindcast for 1995

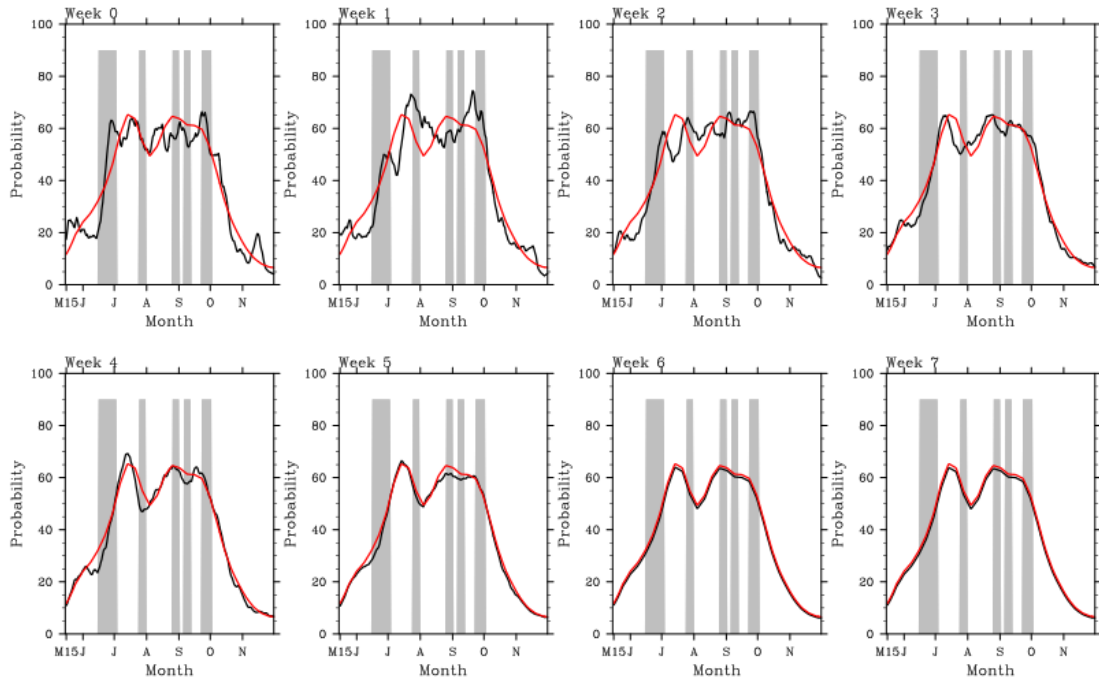


Fig. 50: East Pacific hindcast for 1996

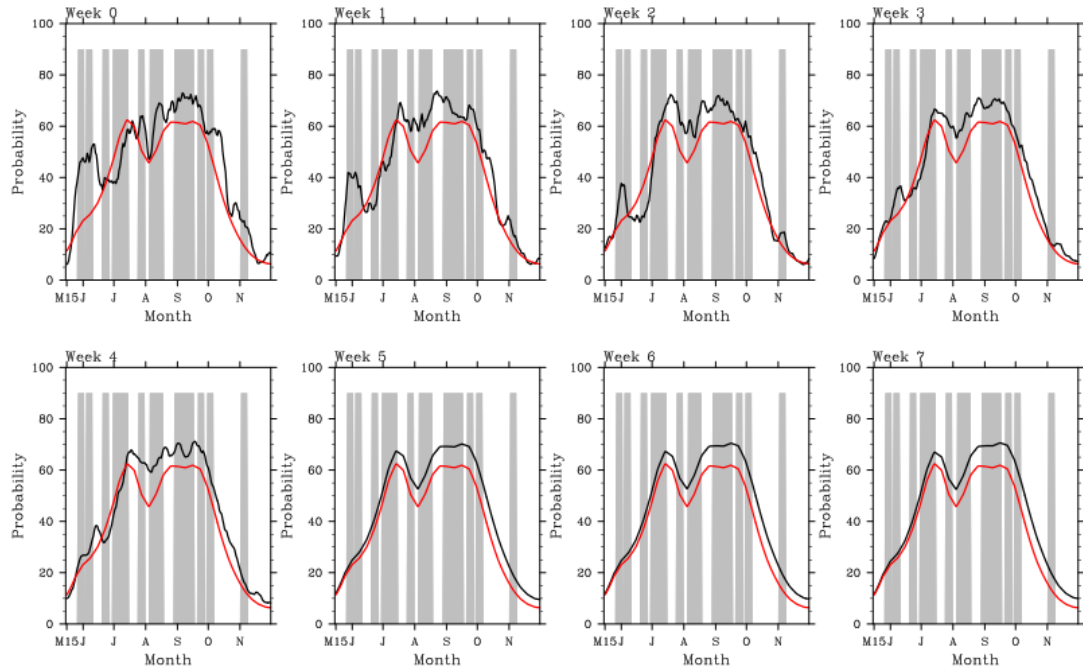


Fig. 51: East Pacific hindcast for 1997

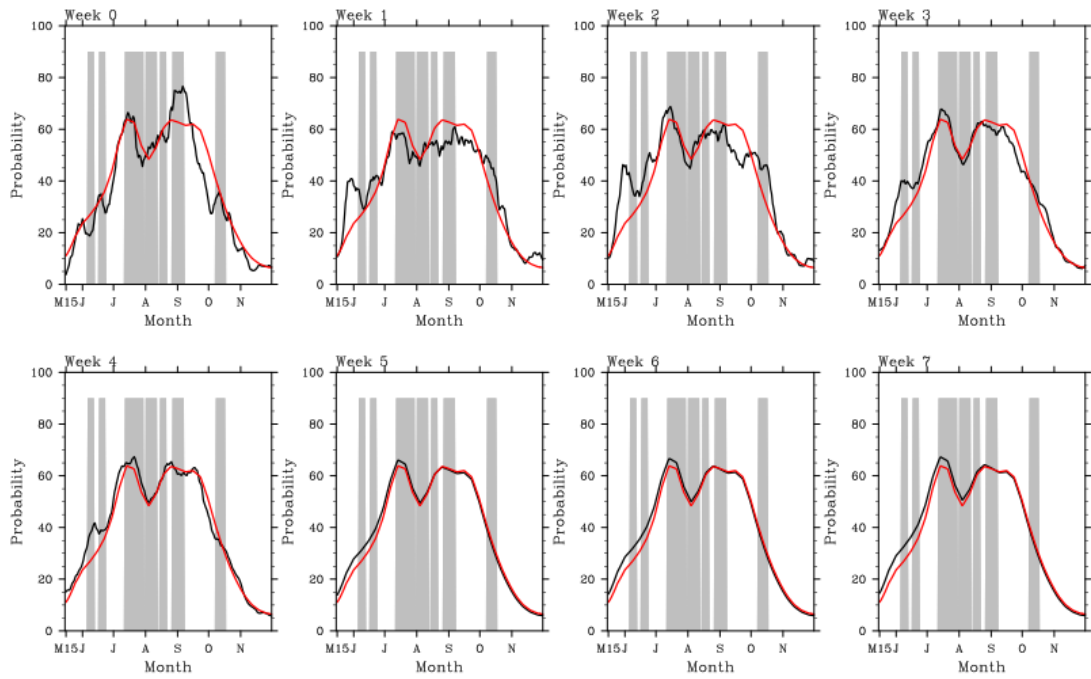


Fig. 52: East Pacific hindcast for 1998

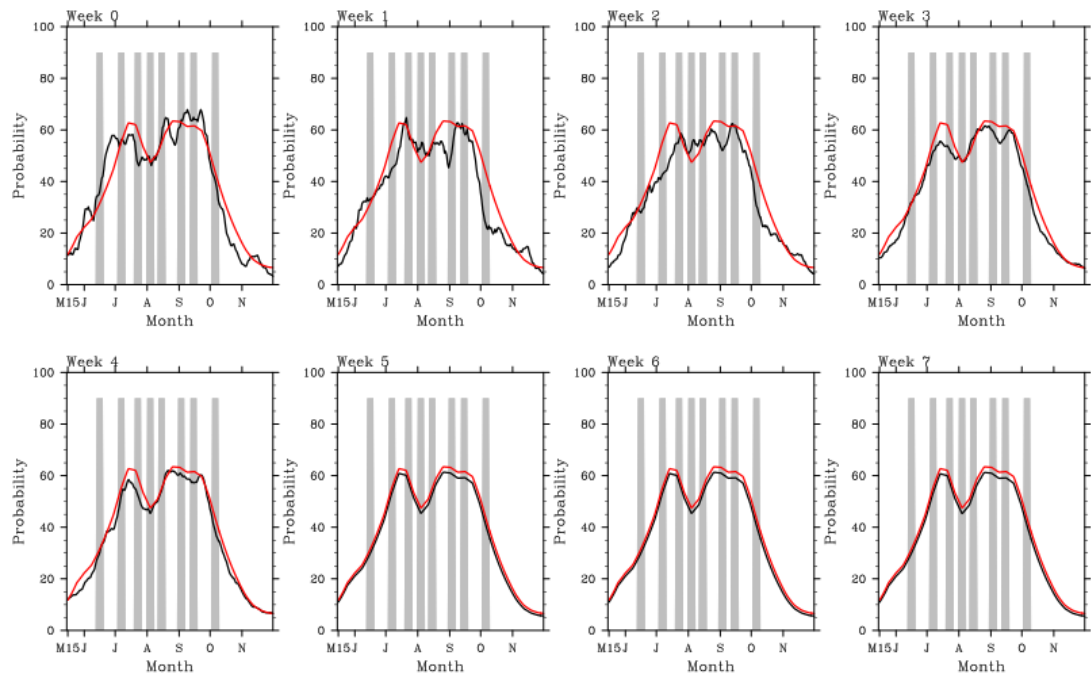


Fig. 53: East Pacific hindcast for 1999

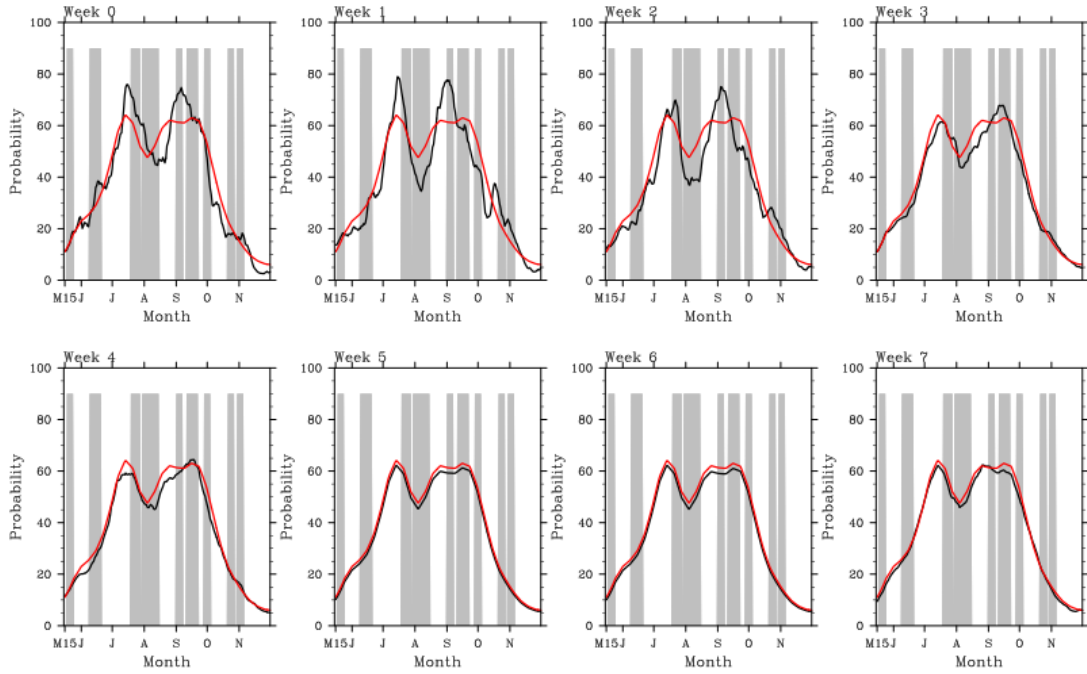


Fig. 54: East Pacific hindcast for 2000

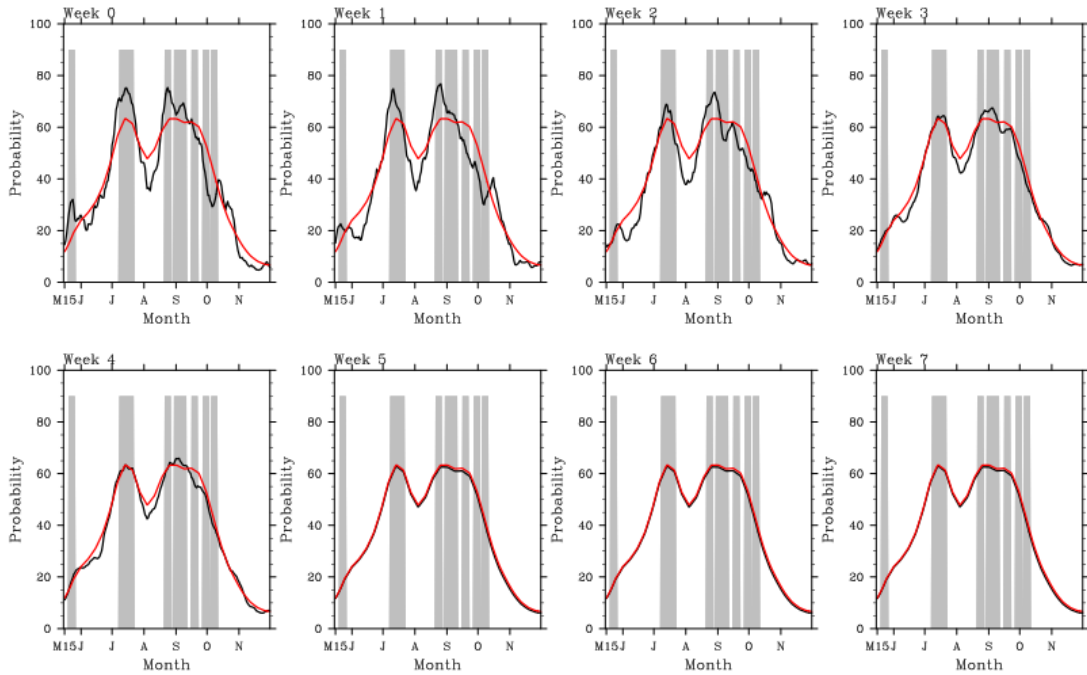


Fig. 55: East Pacific hindcast for 2001

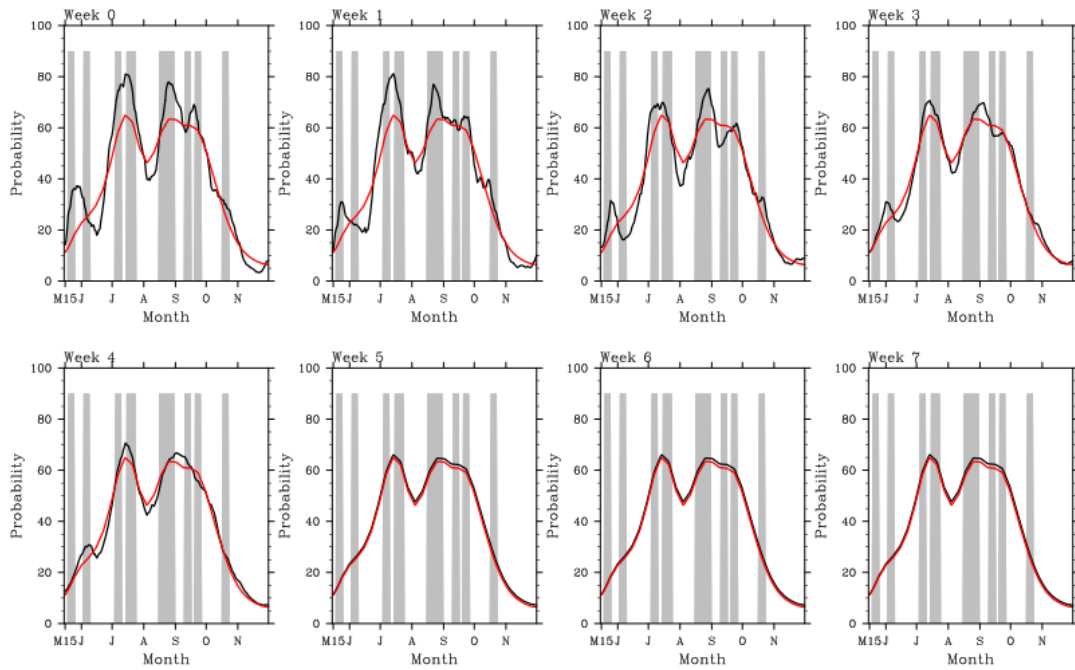


Fig. 56: East Pacific hindcast for 2002

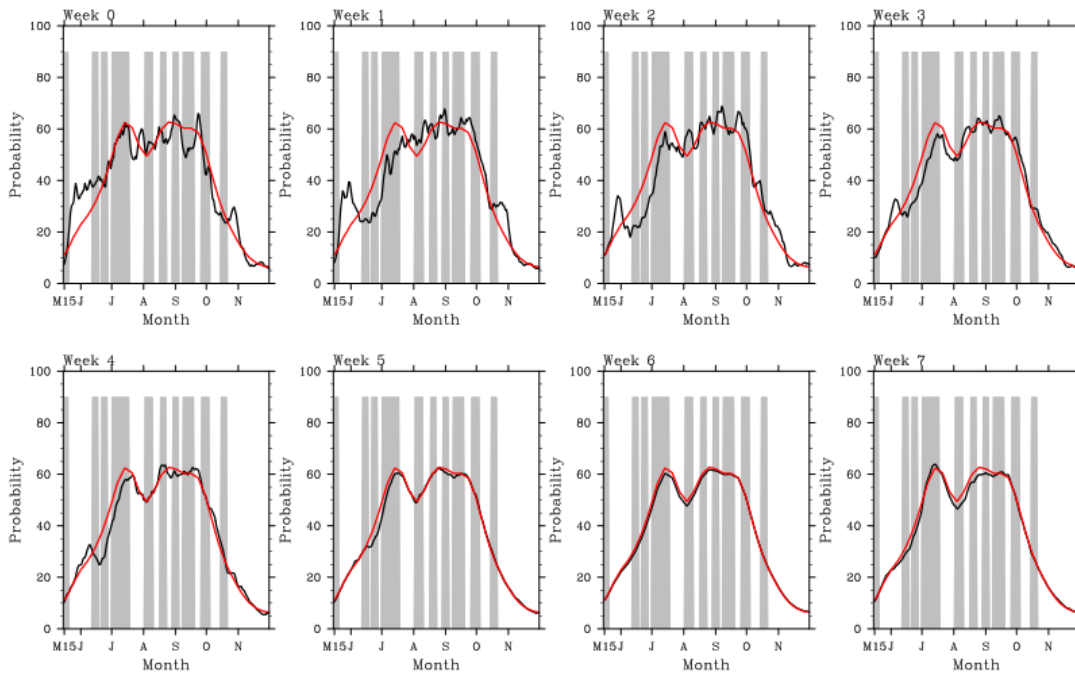


Fig. 57: East Pacific hindcast for 2003

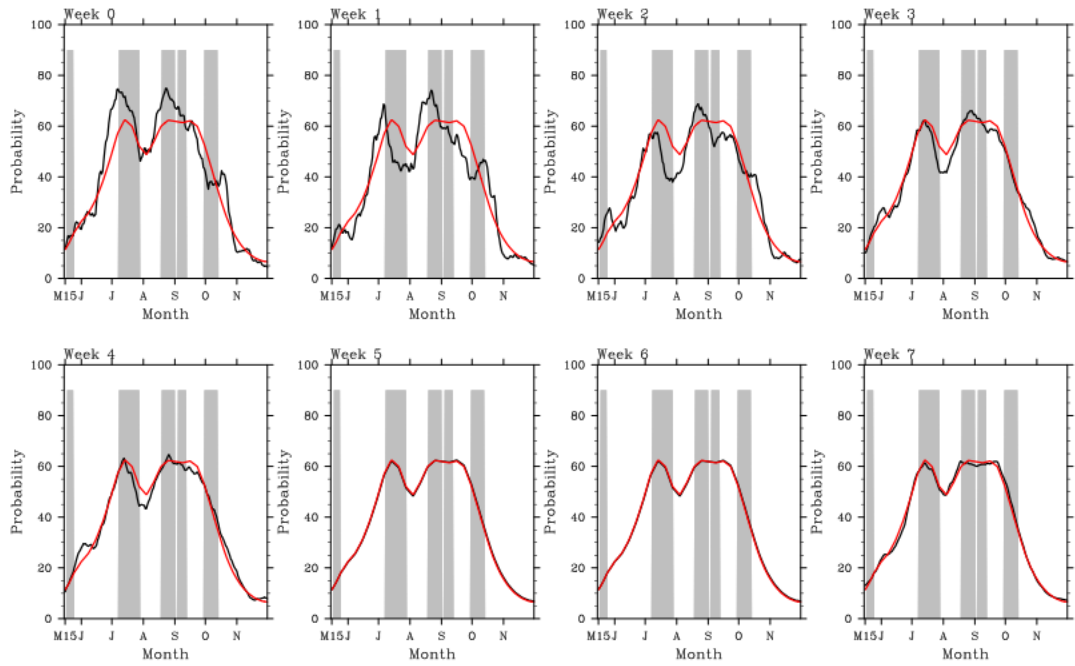


Fig. 58: East Pacific hindcast for 2004

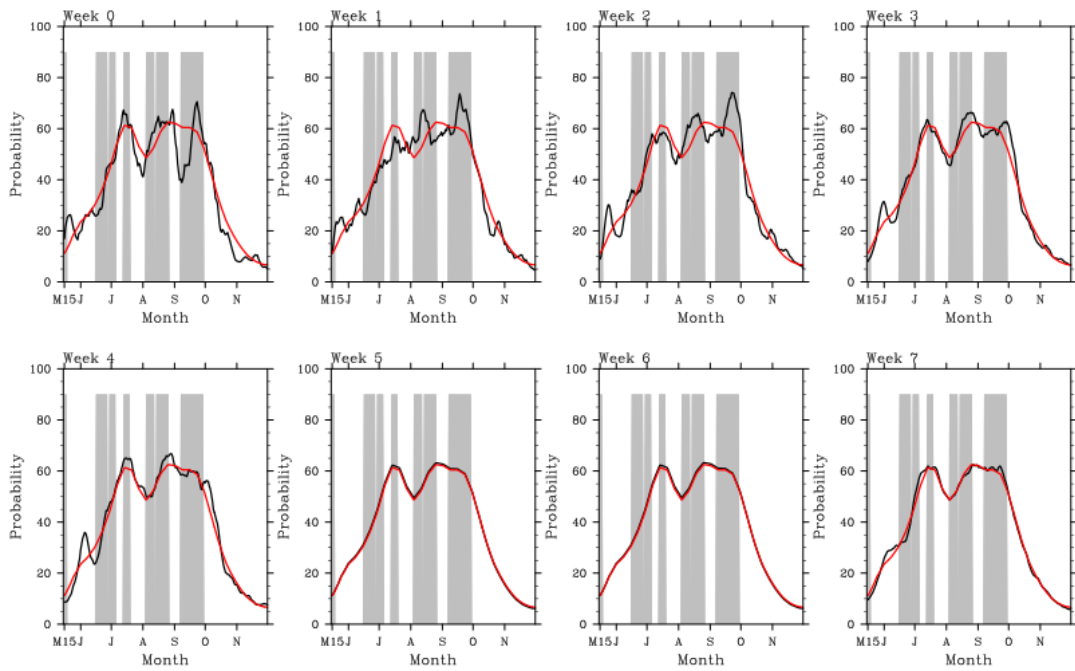


Fig. 59: East Pacific hindcast for 2005

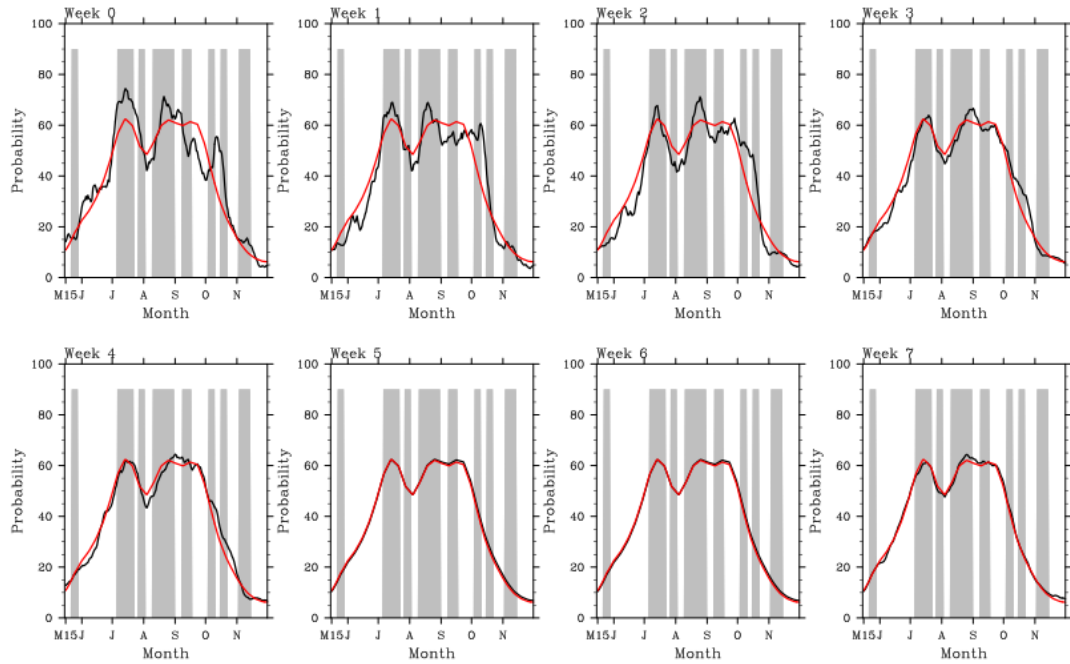


Fig. 60: East Pacific hindcast for 2006

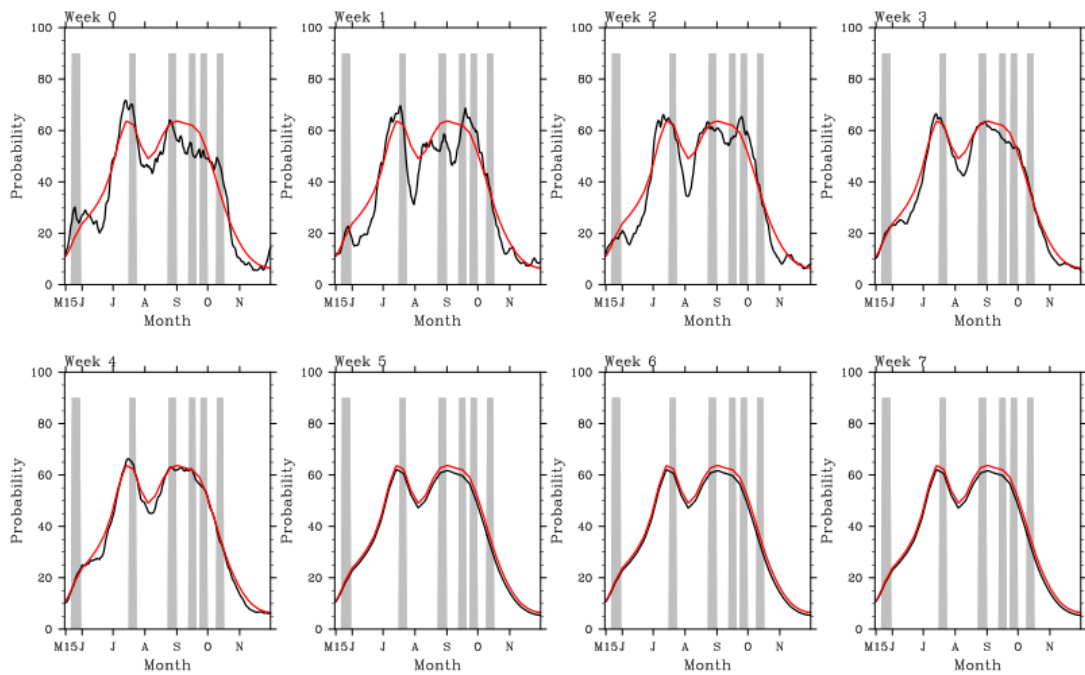


Fig. 61: East Pacific hindcast for 2007

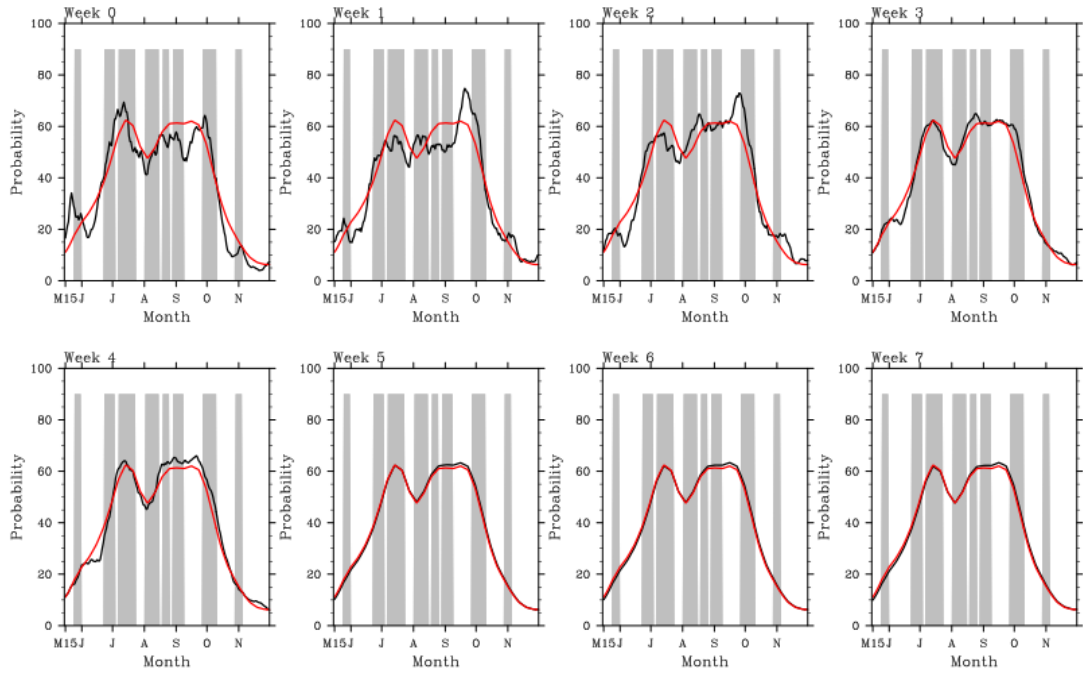


Fig. 62: East Pacific hindcast for 2008

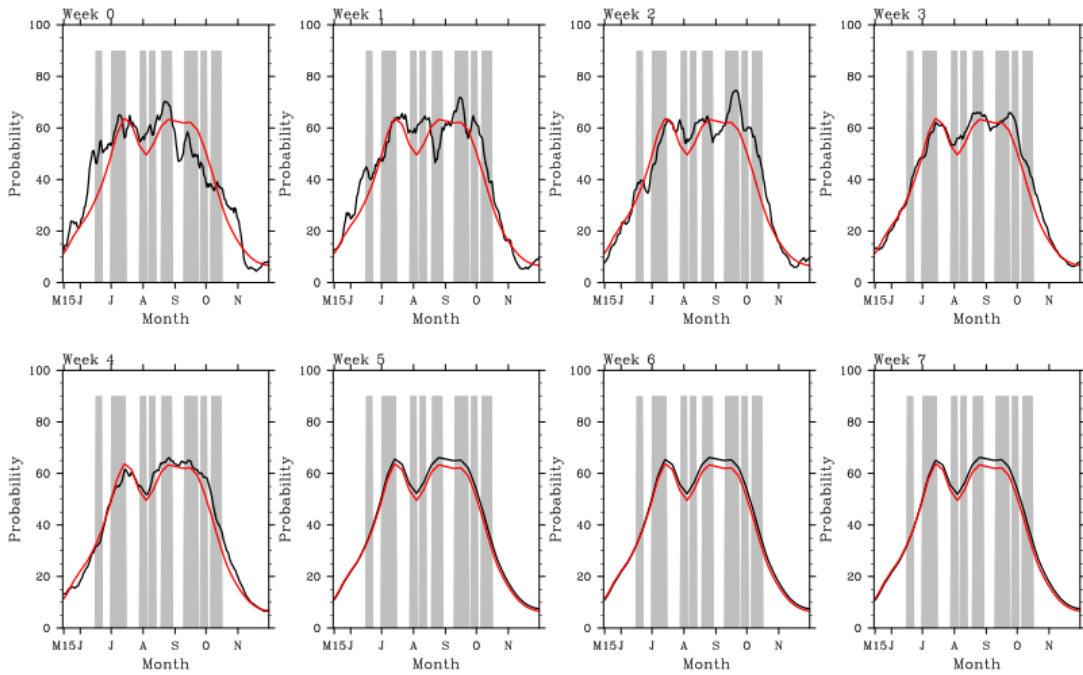


Fig. 63: East Pacific hindcast for 2009

Appendix II

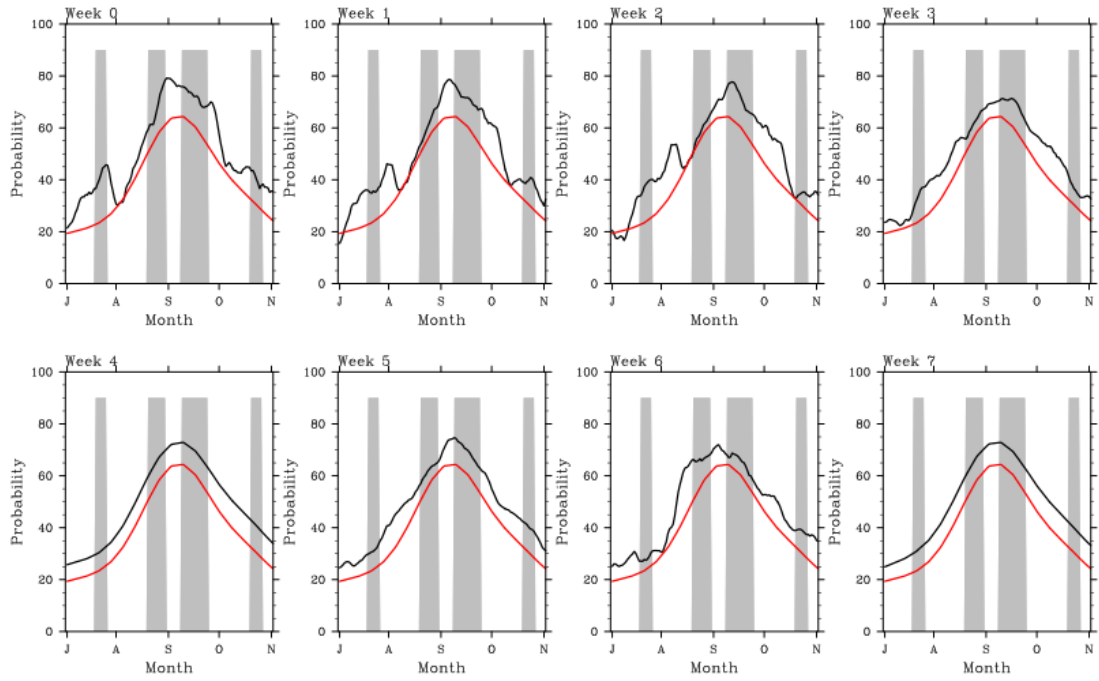


Fig. 64: Atlantic hindcast for 1975

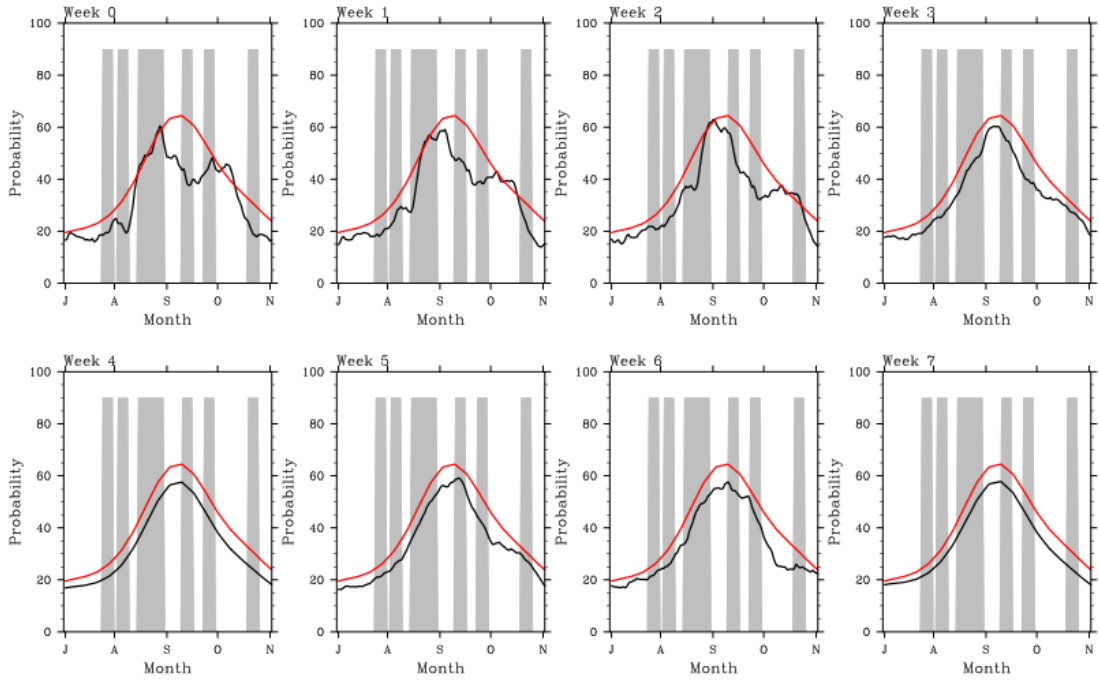


Fig. 65: Atlantic hindcast for 1976

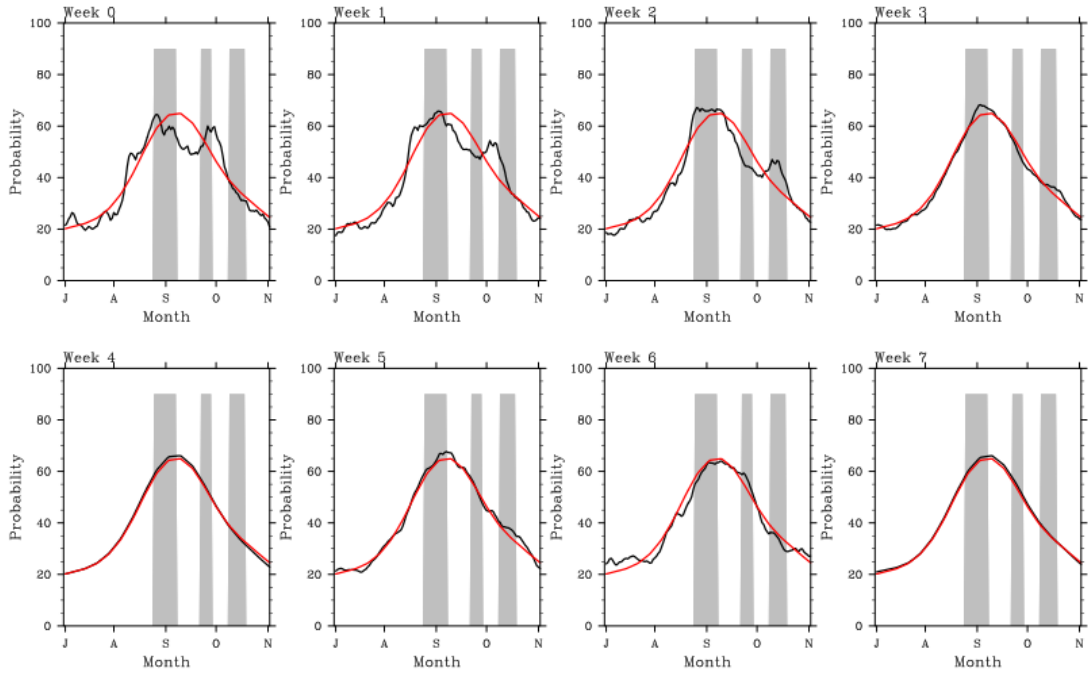


Fig. 66: Atlantic hindcast for 1977

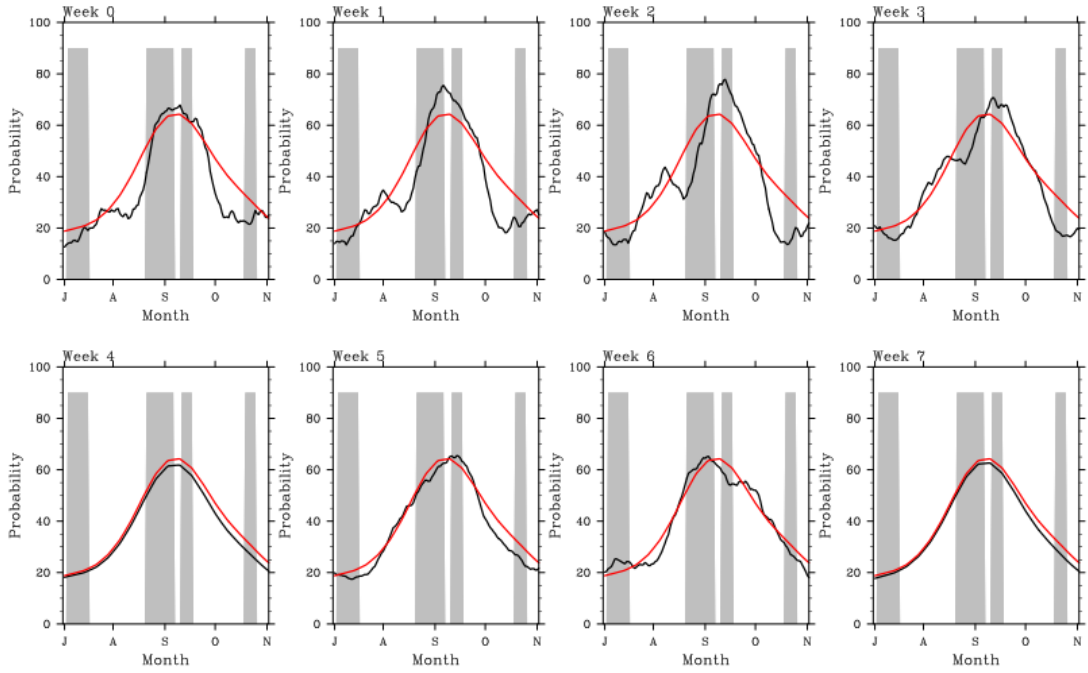


Fig. 67: Atlantic hindcast for 1979

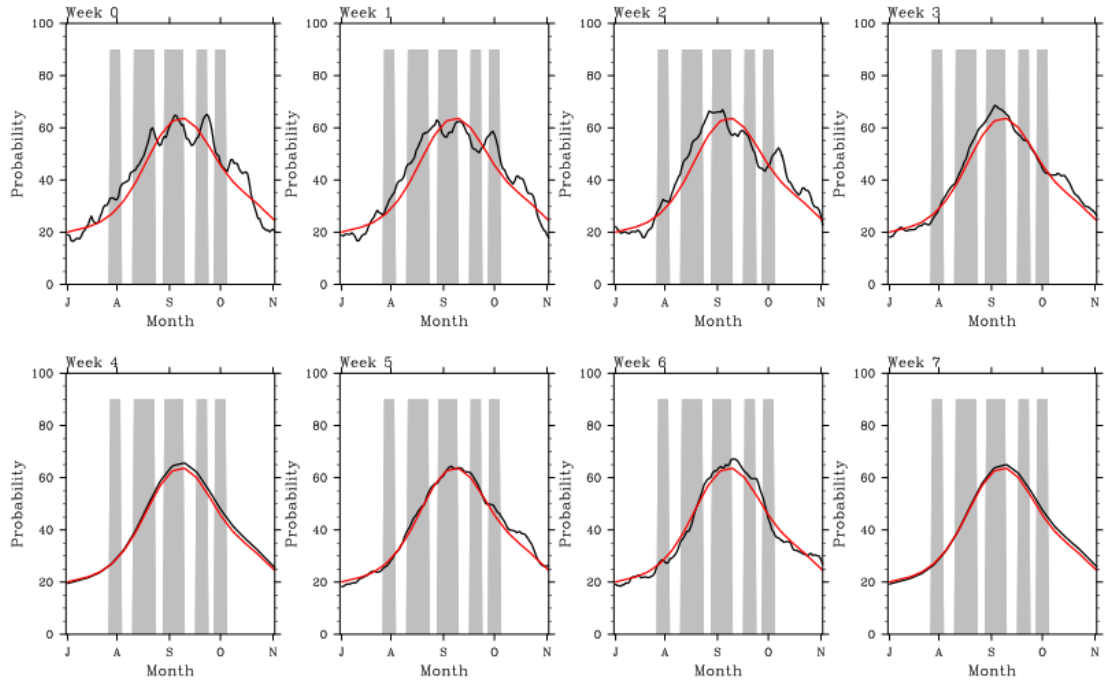


Fig. 68: Atlantic hindcast for 1980

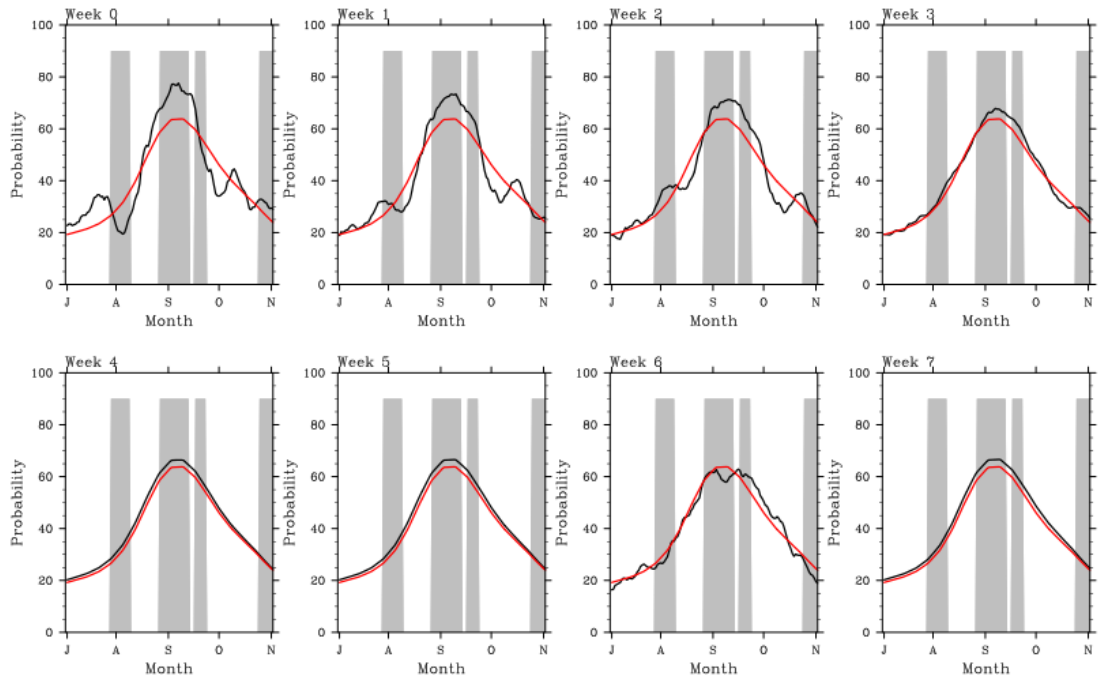


Fig. 69: Atlantic hindcast for 1981

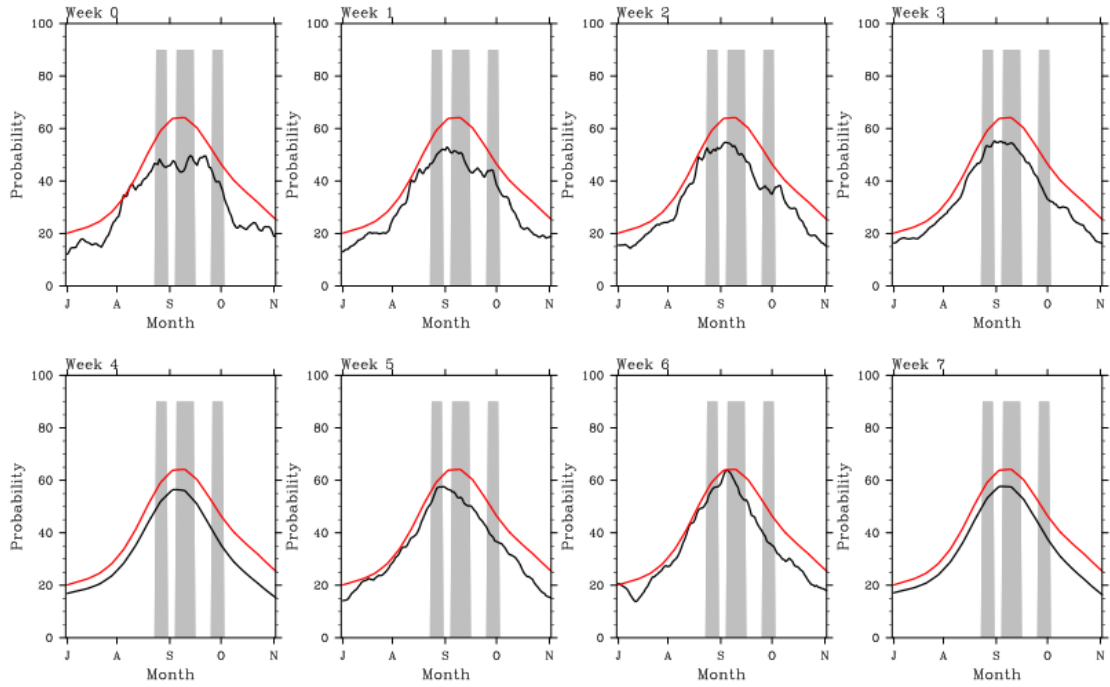


Fig. 70: Atlantic hindcast for 1982

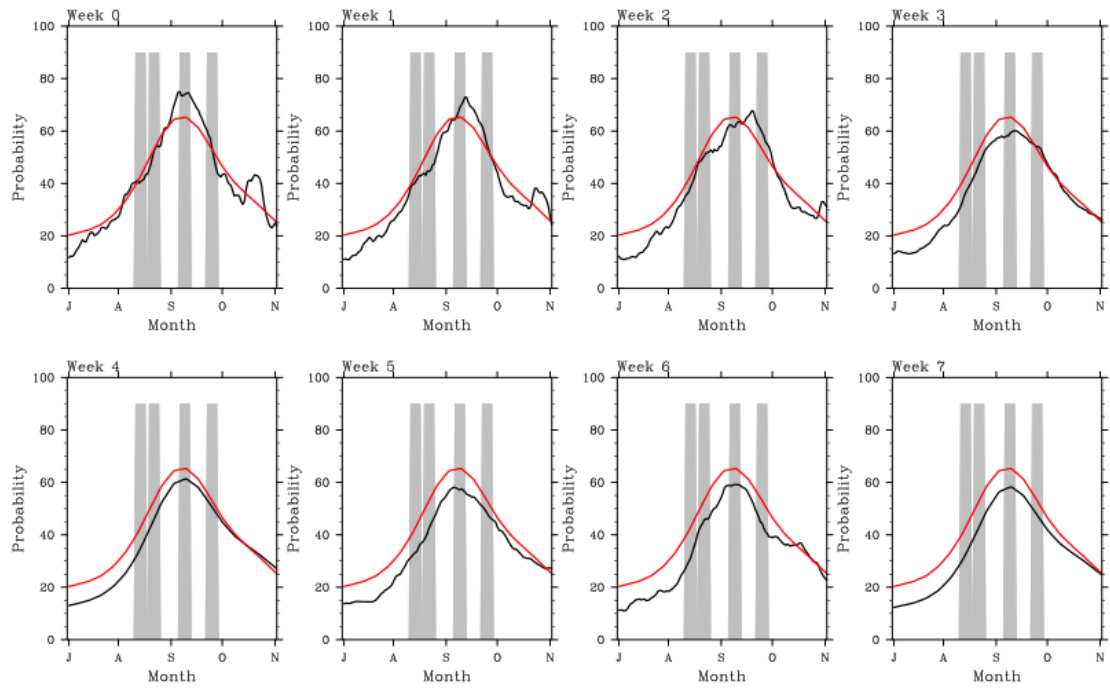


Fig. 71: Atlantic hindcast for 1983

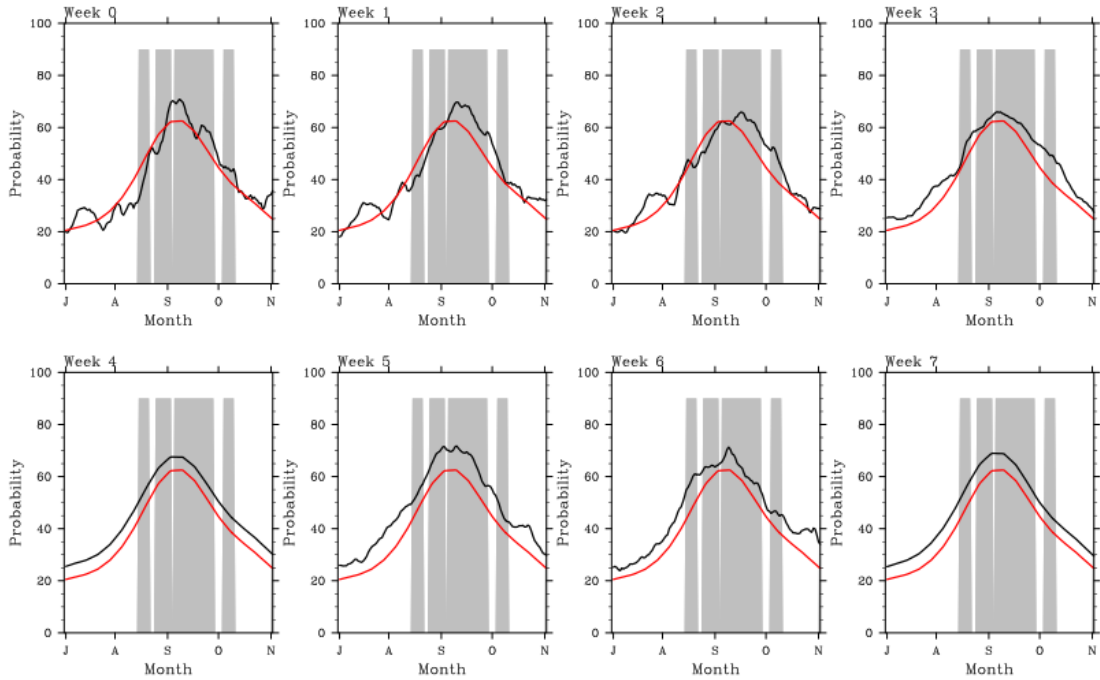


Fig. 72: Atlantic hindcast for 1984

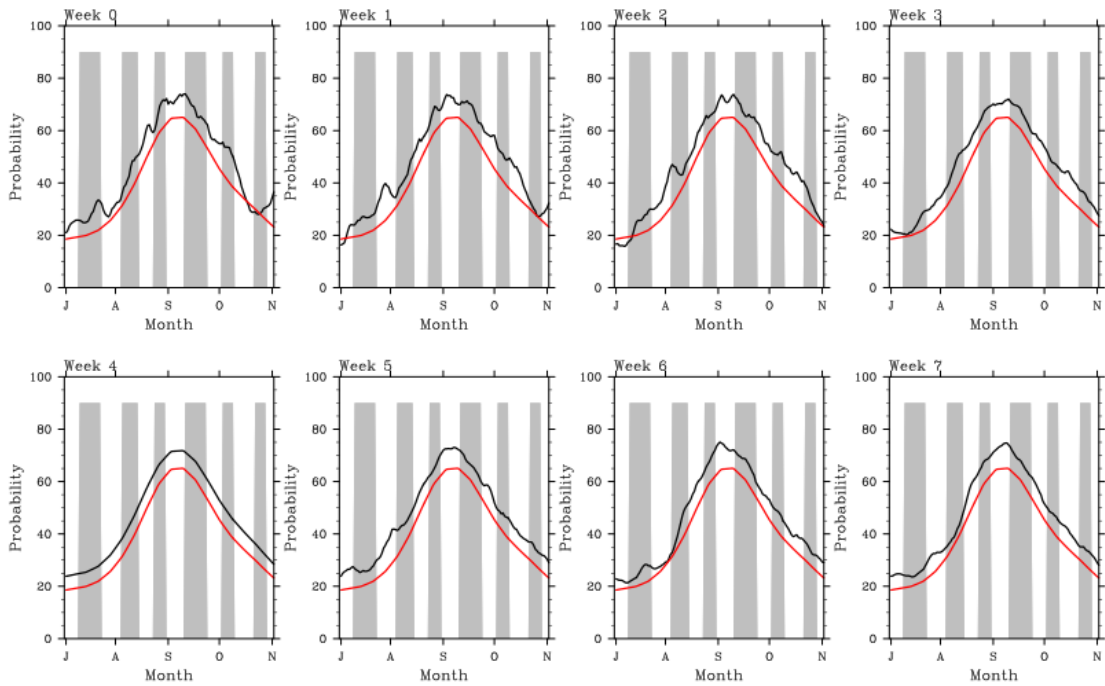


Fig. 73: Atlantic hindcast for 1985

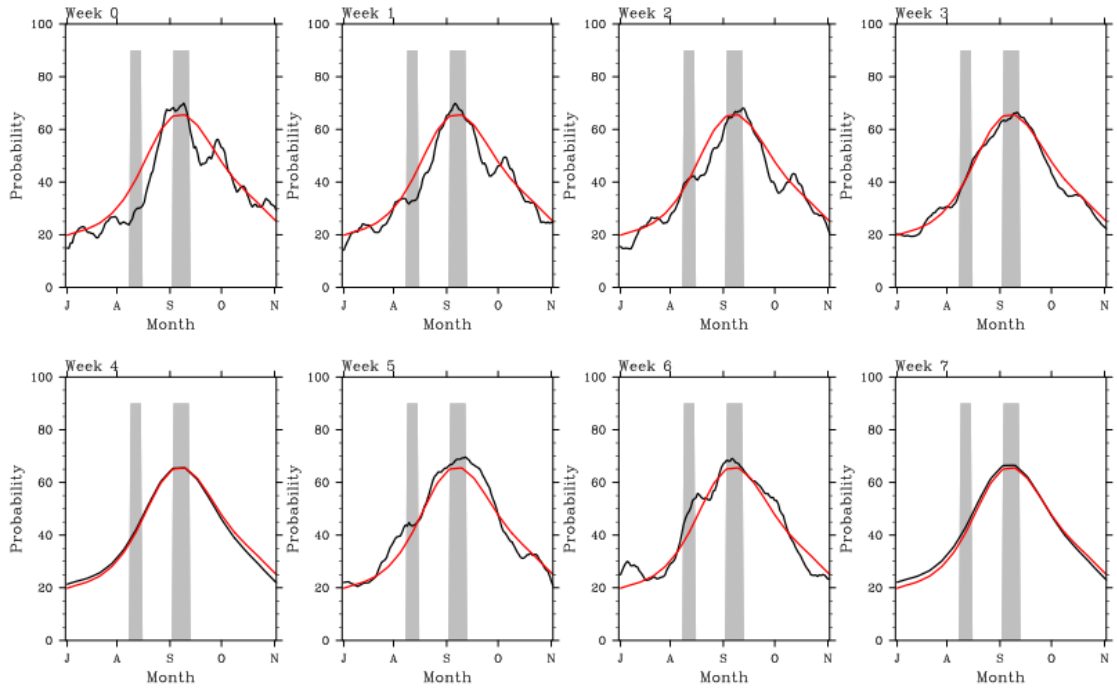


Fig. 74: Atlantic hindcast for 1986

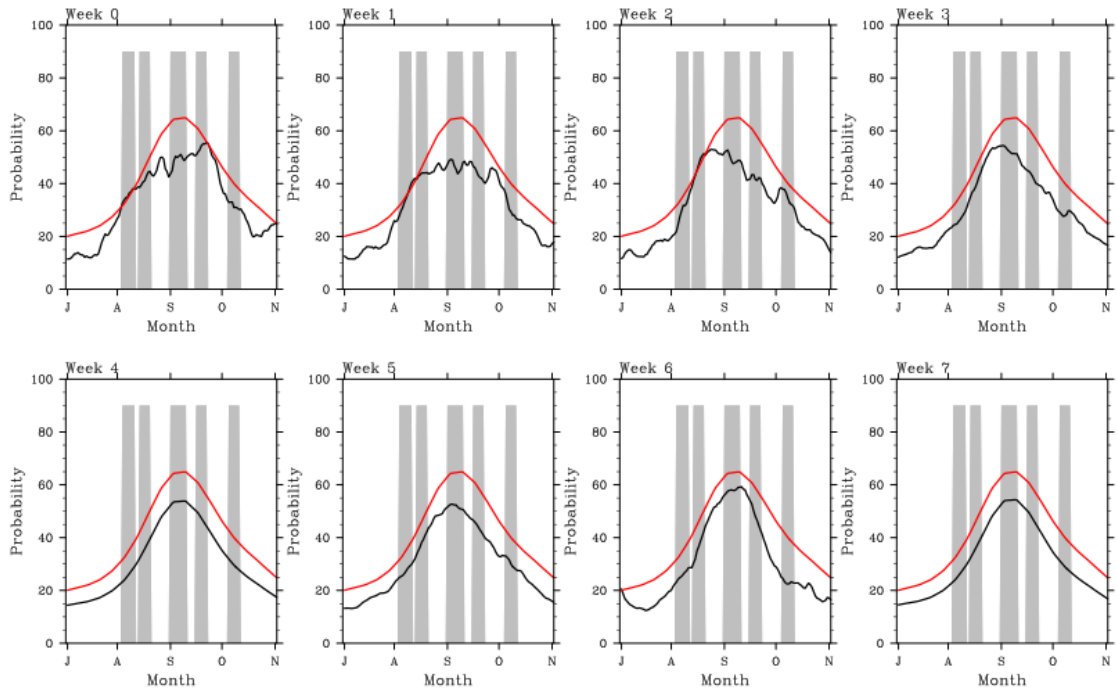


Fig. 75: Atlantic hindcast for 1987

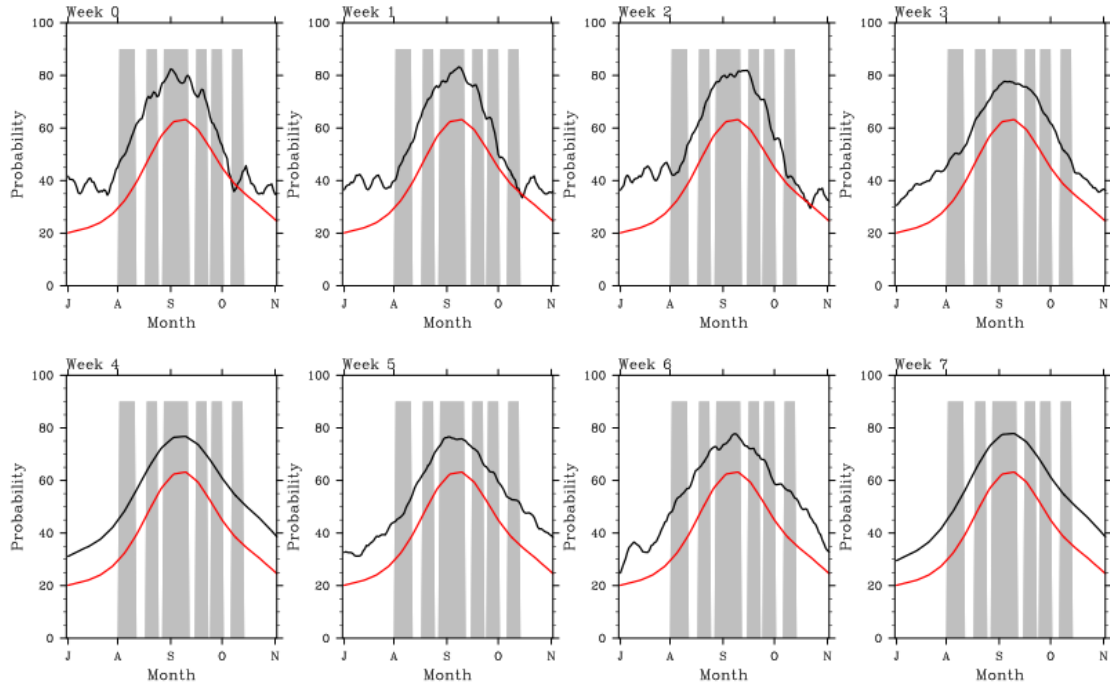


Fig. 76: Atlantic hindcast for 1988

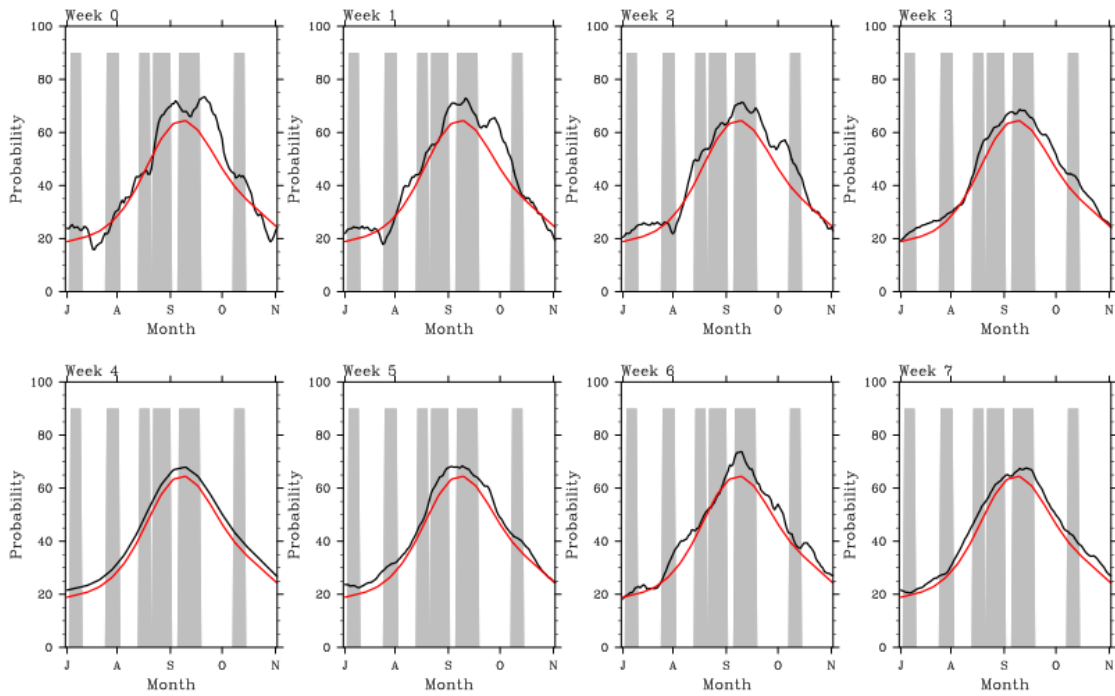


Fig. 77: Atlantic hindcast for 1989

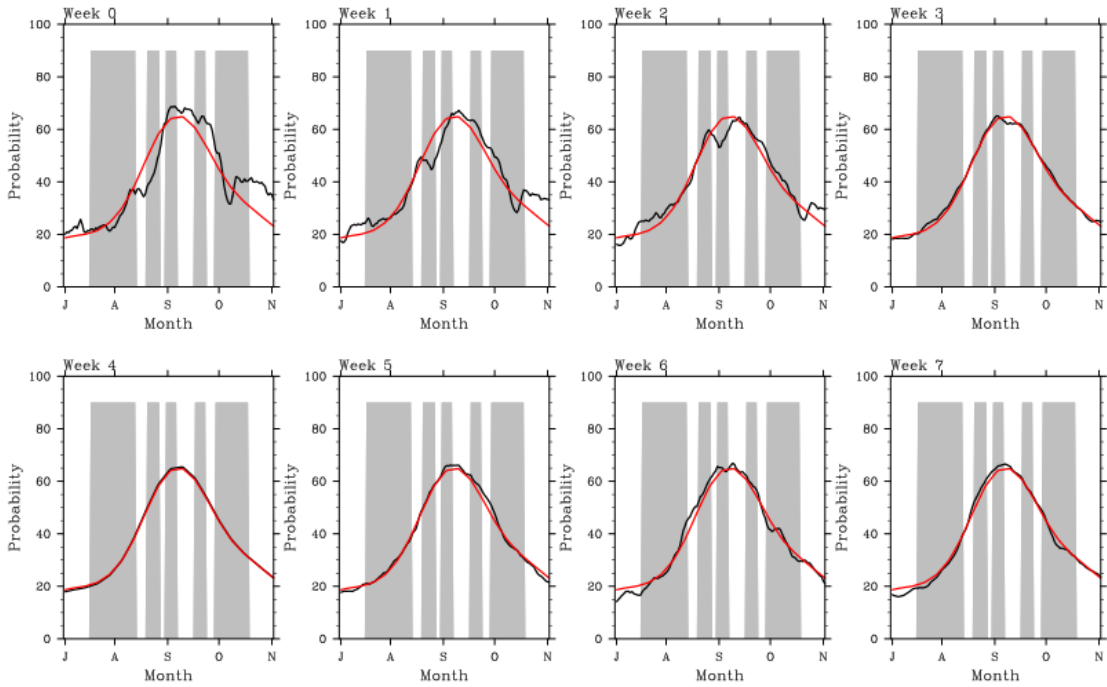


Fig. 78: Atlantic hindcast for 1990

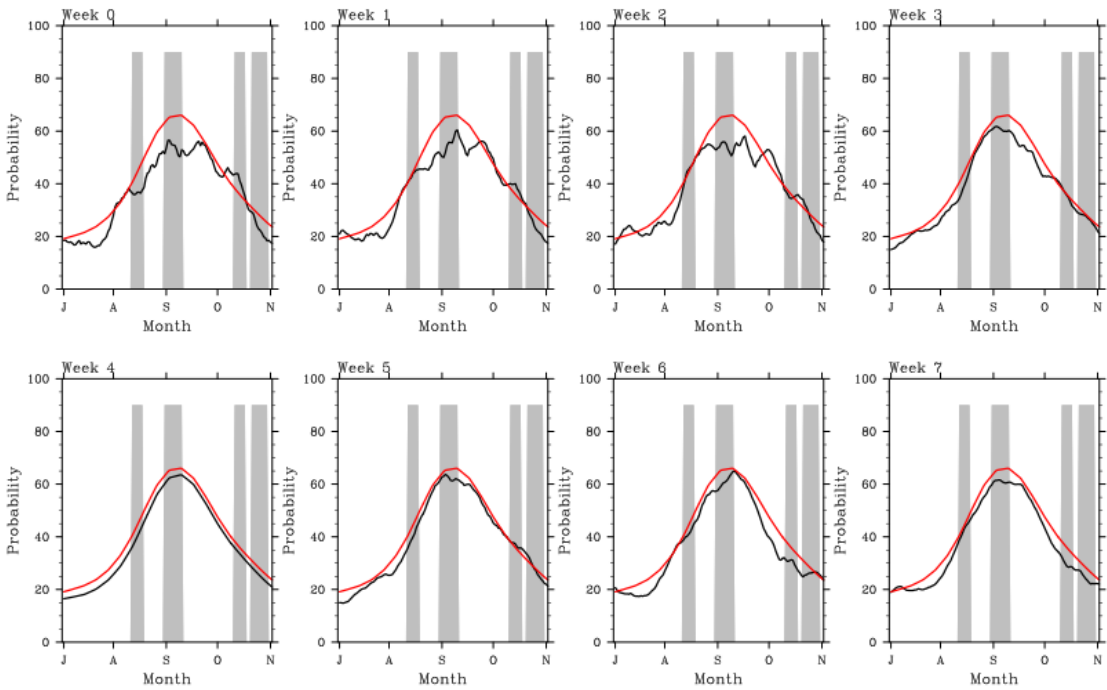


Fig. 79: Atlantic hindcast for 1991

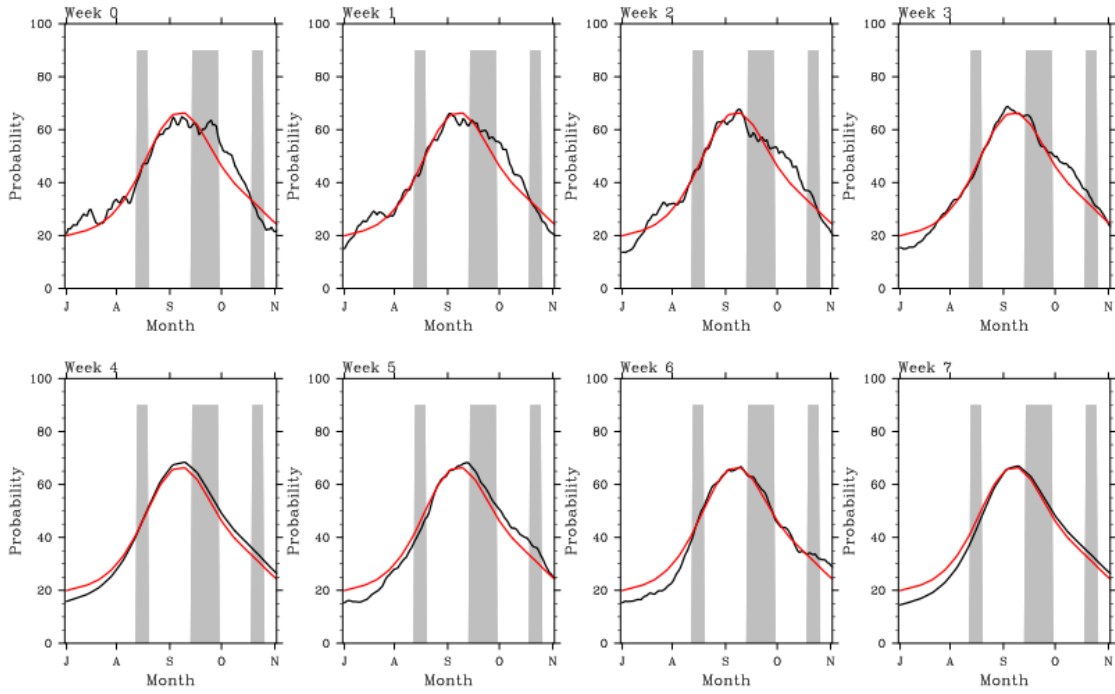


Fig. 80: Atlantic hindcast for 1992

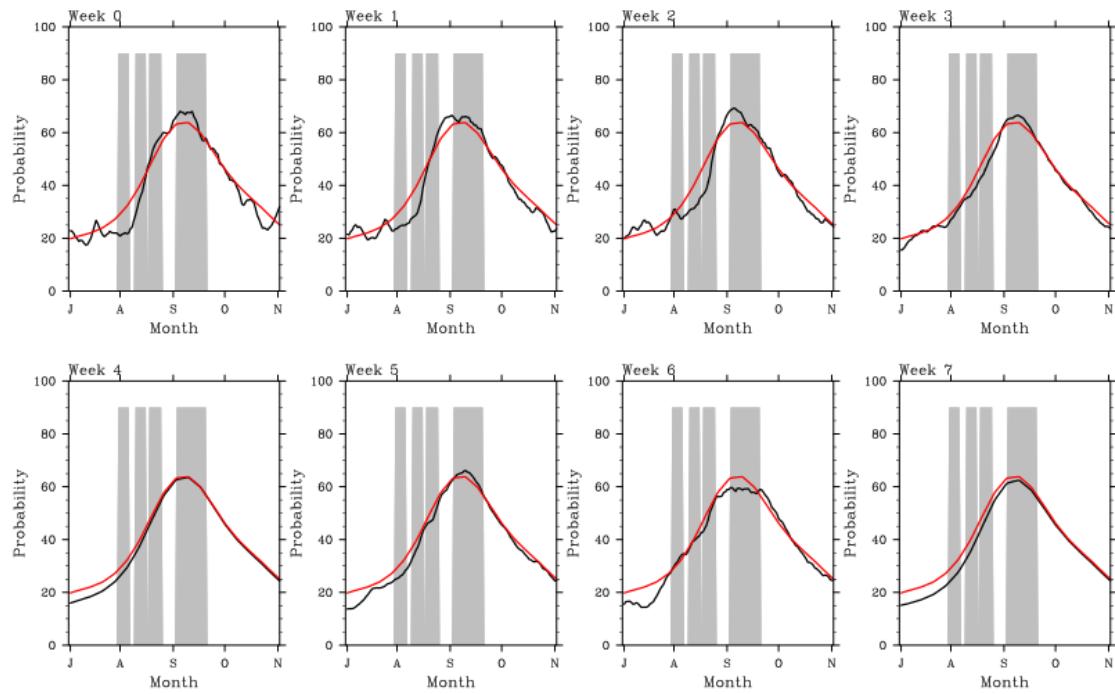


Fig. 81: Atlantic hindcast for 1993

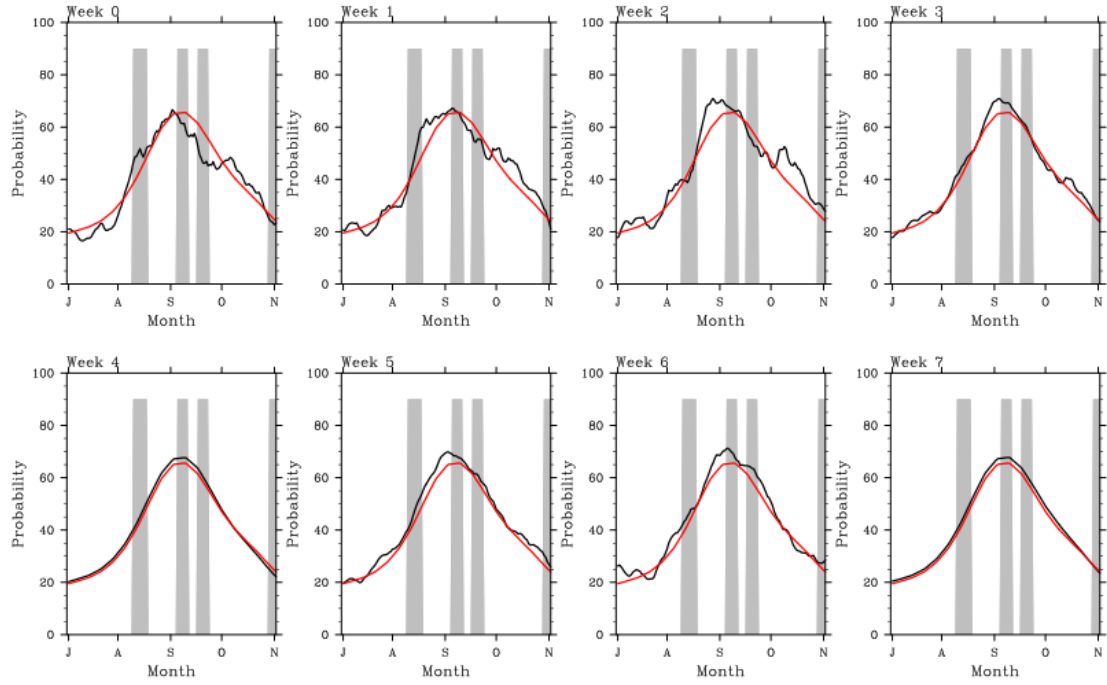


Fig. 82: Atlantic hindcast for 1994

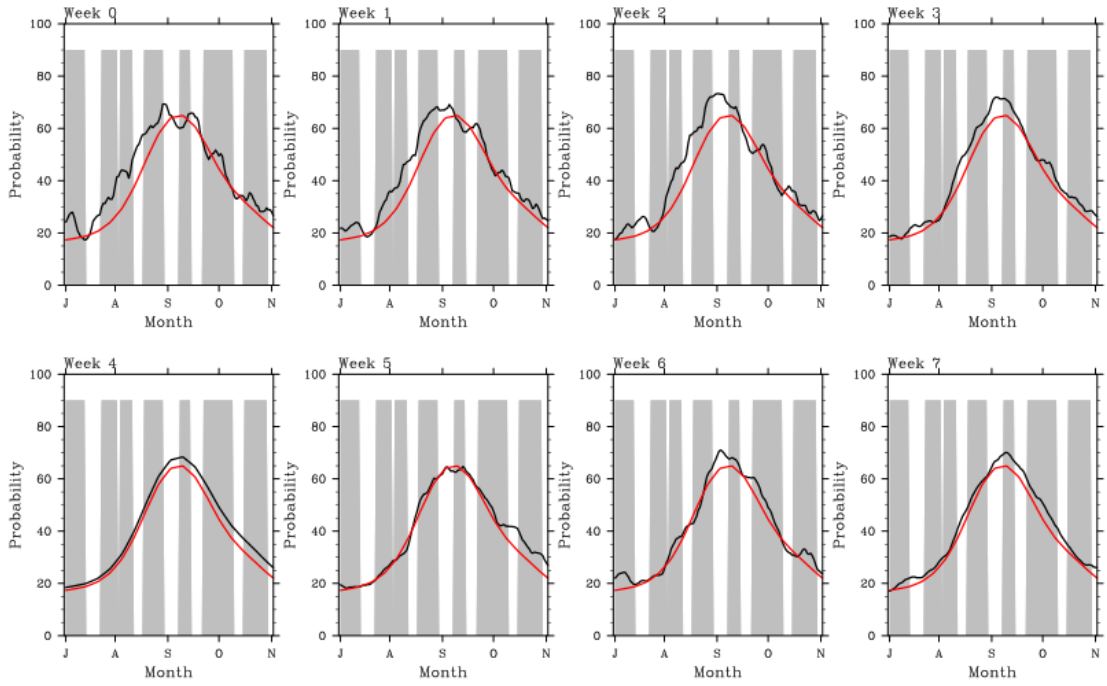


Fig. 83: Atlantic hindcast for 1995

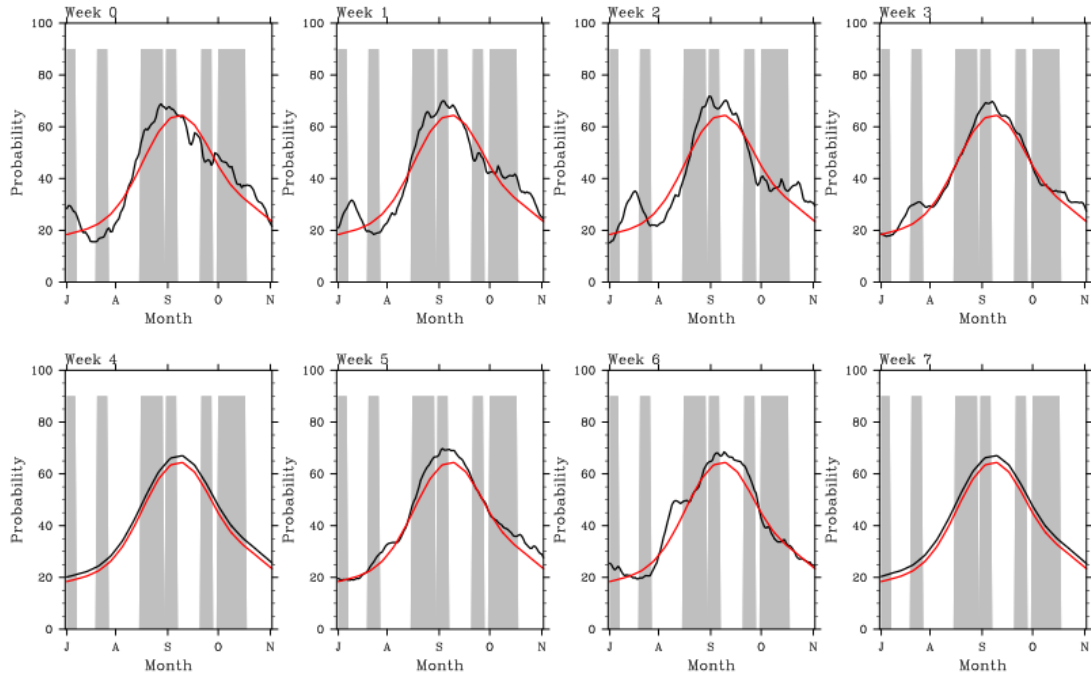


Fig. 84: Atlantic hindcast for 1996

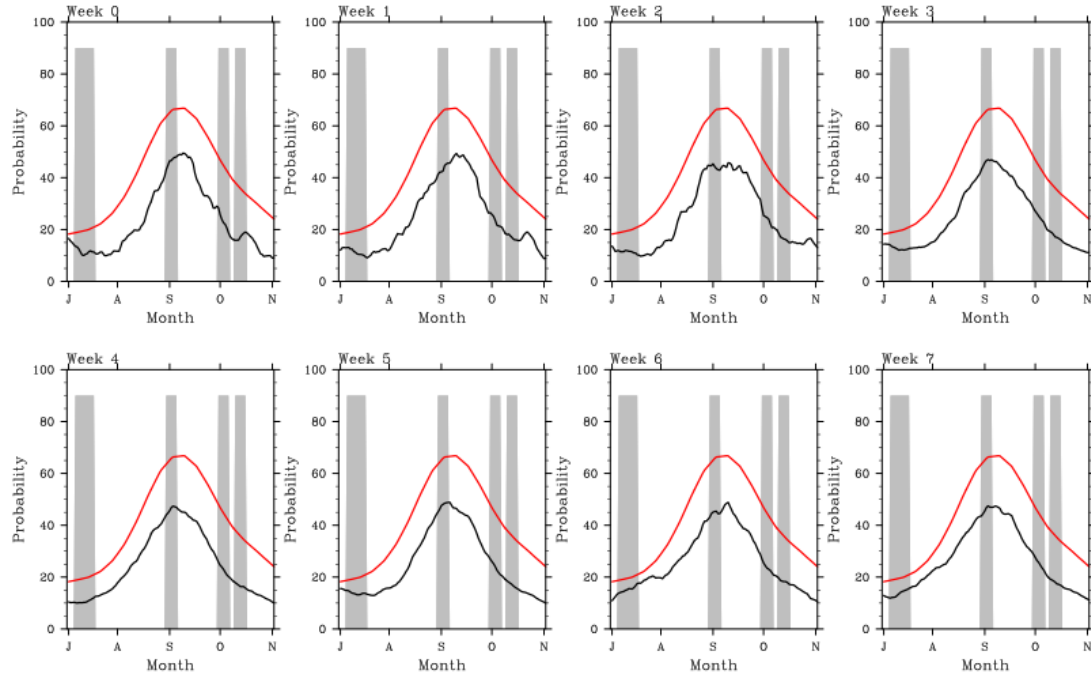


Fig. 85: Atlantic hindcast for 1997

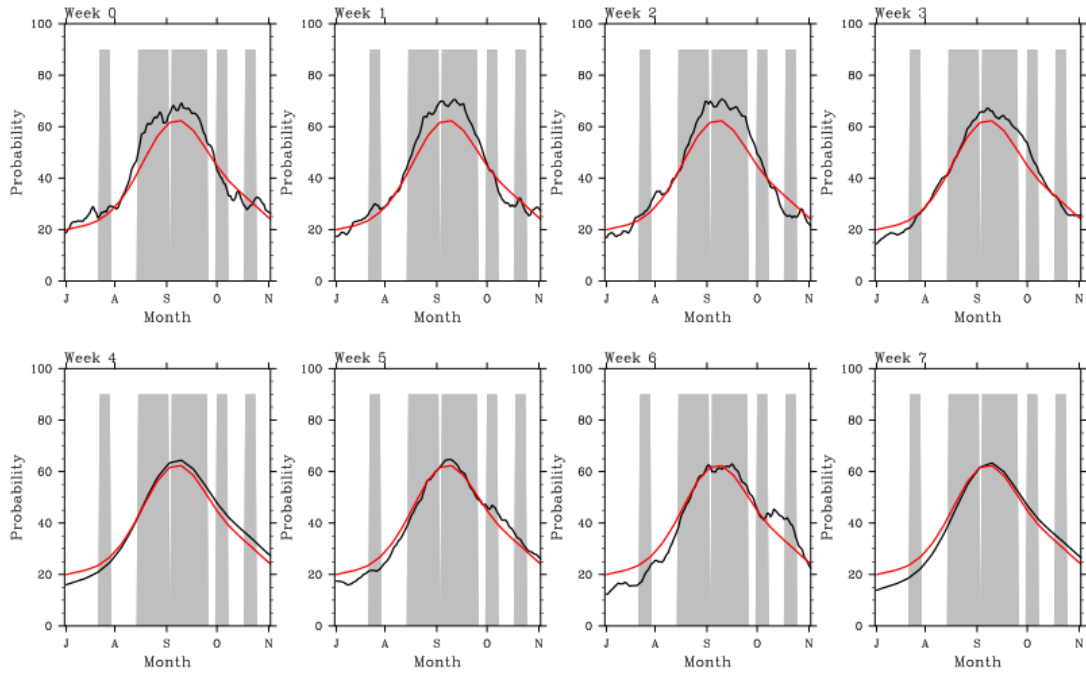


Fig. 86: Atlantic hindcast for 1998

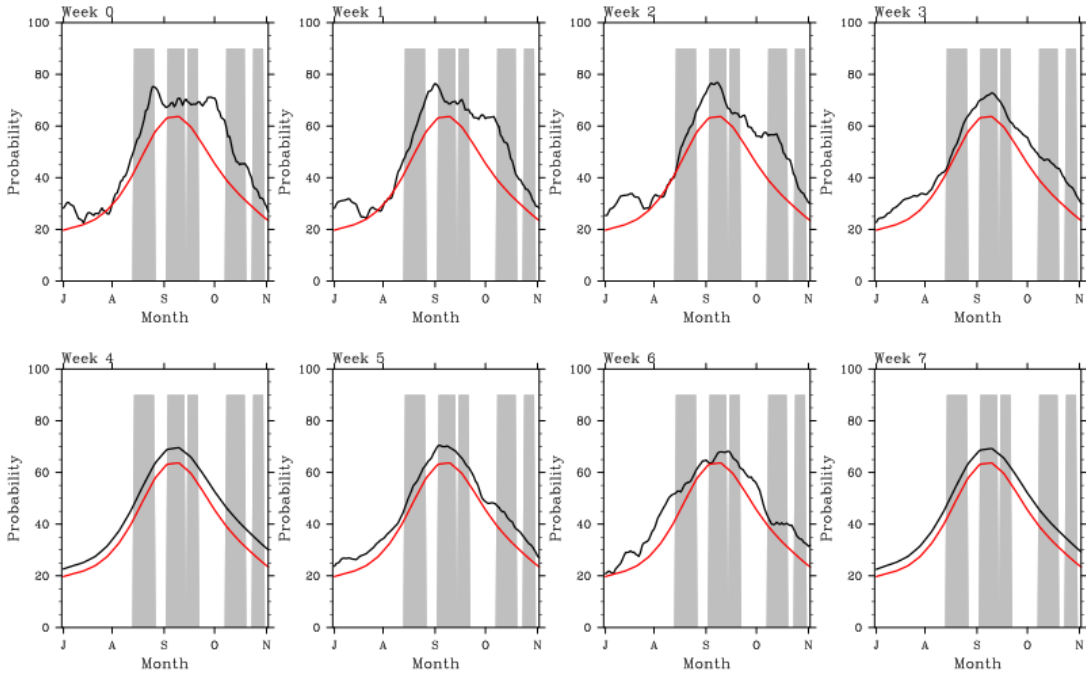


Fig. 87: Atlantic hindcast for 1999

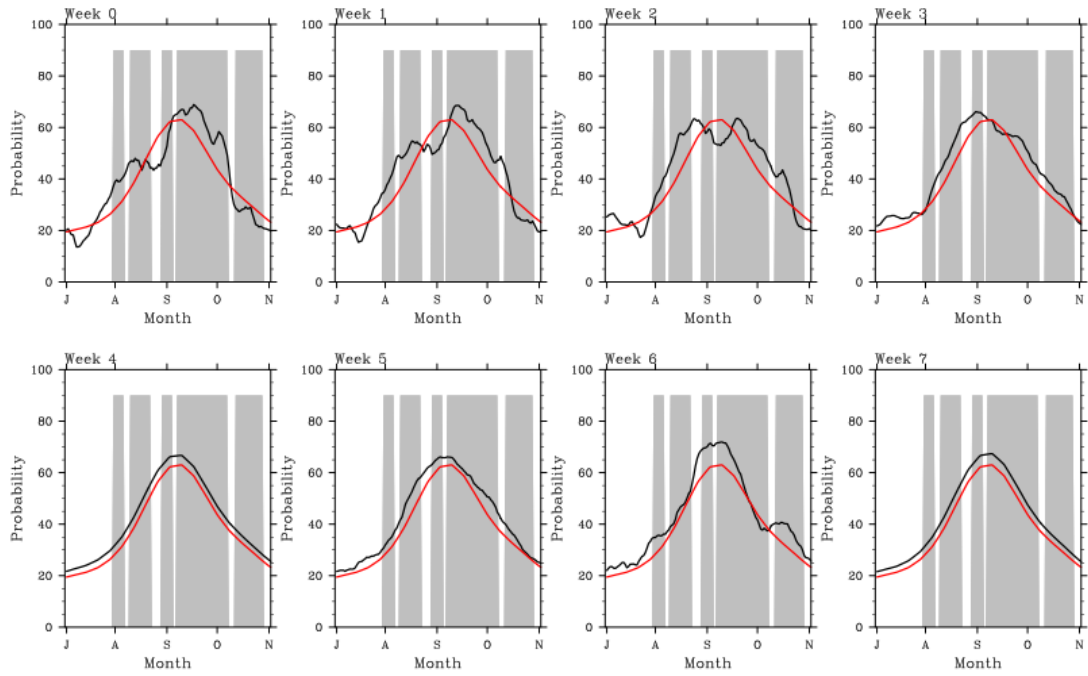


Fig. 88: Atlantic hindcast for 2000

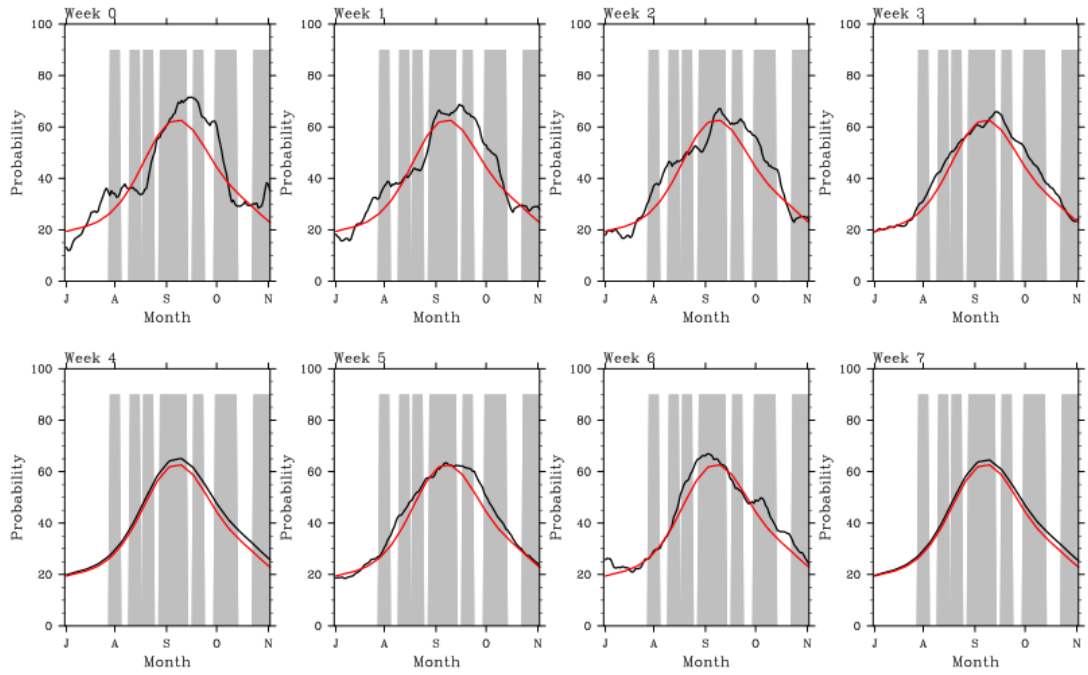


Fig. 89: Atlantic hindcast for 2001

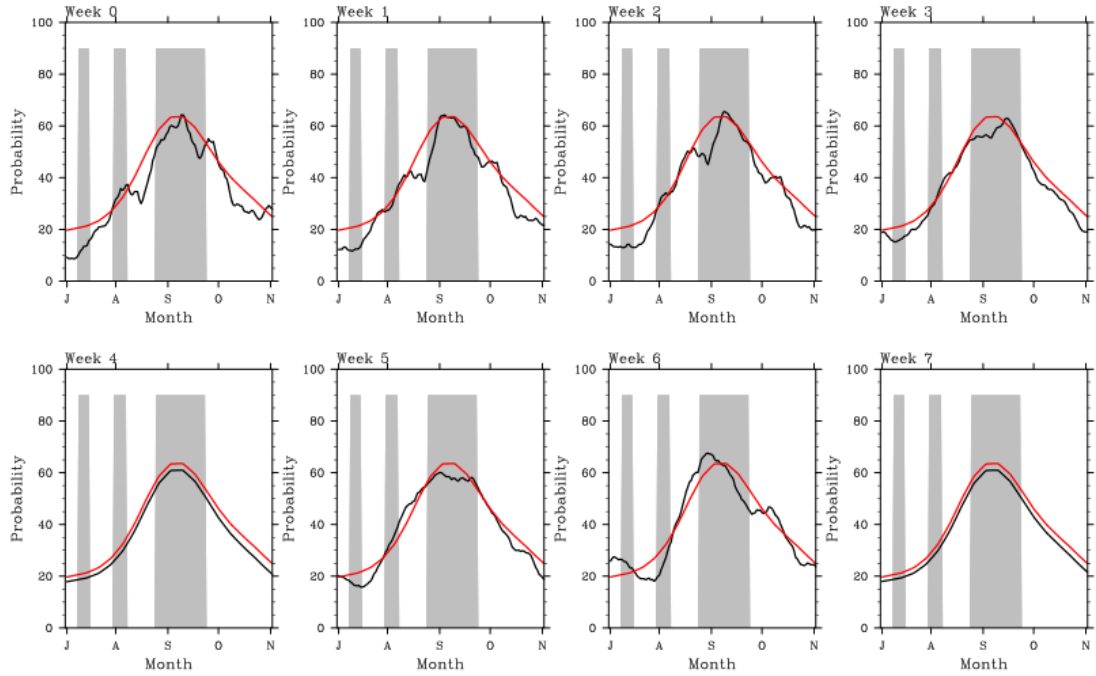


Fig. 90: Atlantic hindcast for 2002

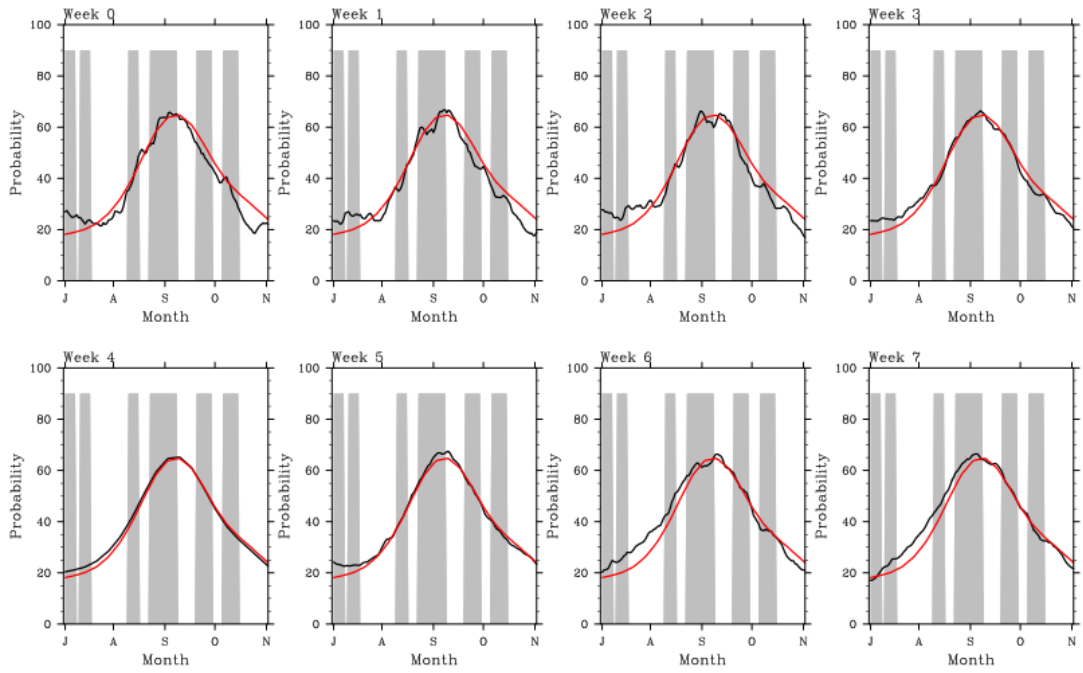


Fig. 91: Atlantic hindcast for 2003

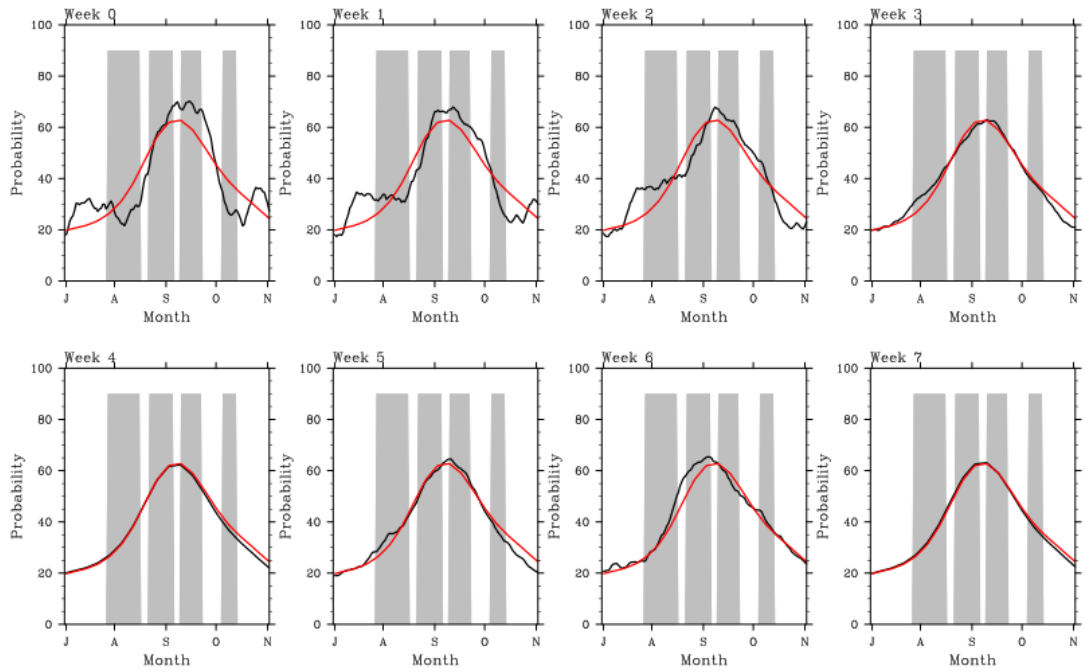


Fig. 92: Atlantic hindcast for 2004

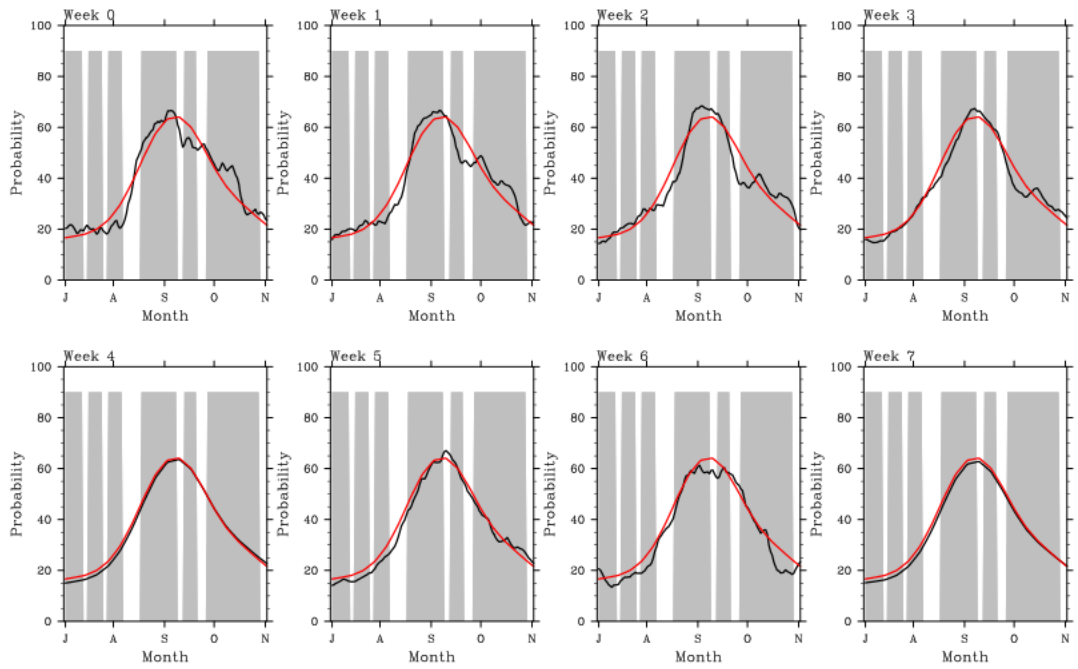


Fig. 93: Atlantic hindcast for 2005

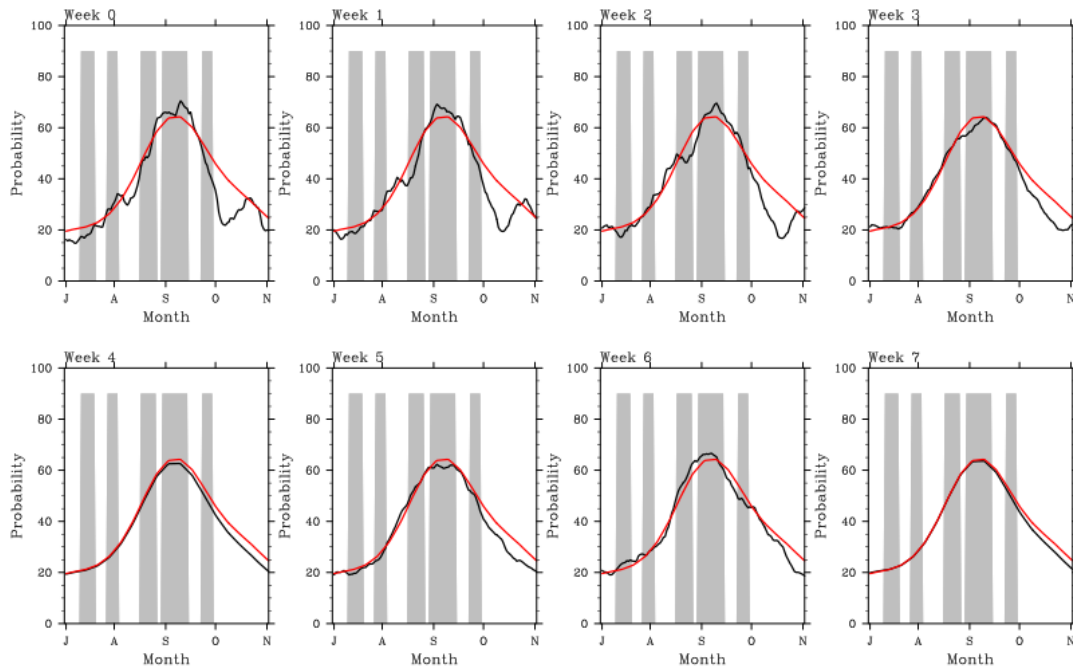


Fig. 94: Atlantic hindcast for 2006

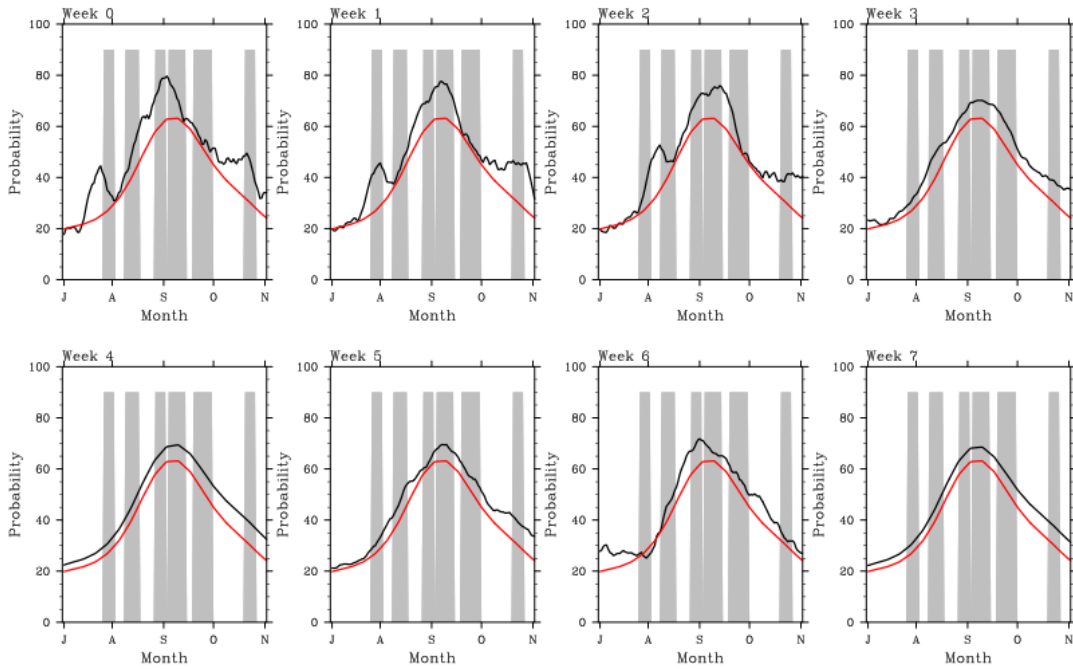


Fig. 95: Atlantic hindcast for 2007

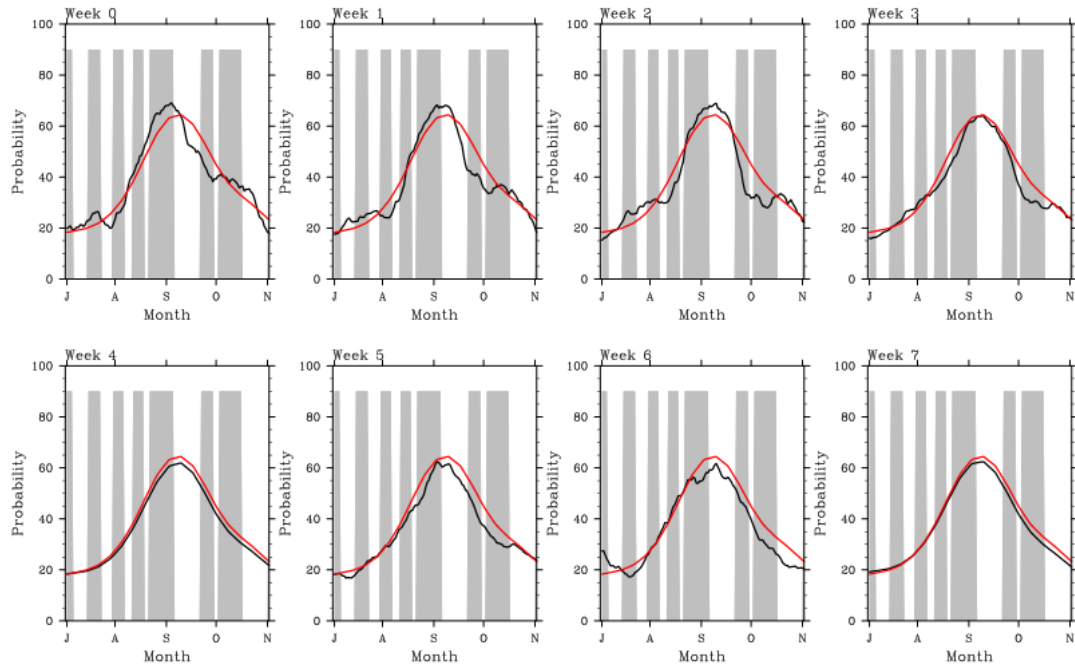


Fig. 96: Atlantic hindcast for 2008

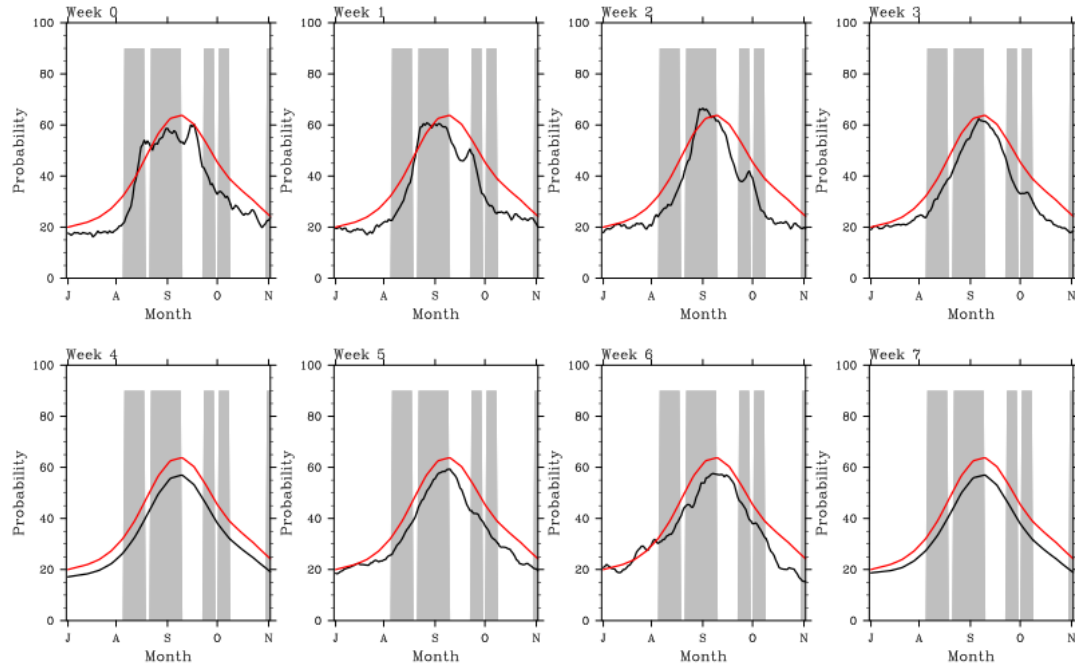


Fig. 97: Atlantic hindcast for 2009